Thermo-Mechanics of Pebble Beds in Fusion Blankets

Yixiang Gan

Institut für Materialforschung
Programm Kernfusion

Thermo-Mechanics of Pebble Beds

in Fusion Blankets

Yixiang Gan

Disclaimer

This work, supported by the European Communities under the contract of Association between EURATOM and Forschungszentrum Karlsruhe, was carried out within the framework of the European Fusion Development Agreement. The views and opinions expressed herein do not necessarily reflect those of the European Commission.

Abstract

Thermo-Mechanics of Pebble Beds in Fusion Blankets

Working as tritium breeder and neutron multiplier materials in Helium Cooled Pebble Bed (HCPB) blankets in fusion reactors, pebble beds are not only subject to severe conditions, but due to their discrete nature, also have complex behaviour. Pebble beds are composed of nearly spherically shaped pebbles. One of the most important issues in HCPB blankets is that the thermal conductivity of the pebble beds changes with the compressive stress state, the latter being introduced by thermal expansion of the pebble beds during operation. Therefore, a material model for describing their fully coupled thermo-mechanical response to the external excitation is essential to check the requirements in the design and analysis of HCPB blankets.

In this dissertation, a numerical simulation scheme for pebble beds under fusion-relevant conditions has been developed. Ceramic breeder and beryllium pebble beds are modelled by means of discrete element and phenomenological approaches. Moreover, the utilization of the available experimental results is also presented in this strategy. In the first approach, we consider each individual pebble as one element obeying equilibrium conditions under contact forces. We study not only the rearrangement of particles but also the overall behaviour of an assembly under the action of the macroscopic compressive stresses. Using random close packing as initial configurations, the discrete element simulation of the uniaxial compression test has been quantitatively compared to experiments. This method yields the distribution of the inter-particle contact forces. We also study the micro-macro relations to relate the microscopic information, such as the maximum contact force and the coordination number inside the assembly, to the macroscopic stress variables.

Assuming a pebble bed is a continuum medium, the phenomenological model, as the second approach, describes the typical overall behaviour of the material under fusion-relevant conditions. With the proper material model, finite element analyses of structures containing pebble beds can be performed. In the present phenomenological model, the thermo-mechanical response of a pebble bed is represented by a nonlinear elasticity law, a modified Drucker-Prager-Cap model and a strain-dependent thermal conductivity. The material parameters in the phenomenological model have been successfully identified from the available experimental results. This customized method has been used for different types of pebble beds, and this method has been verified along with the present phenomenological model at different bed temperature levels. Moreover, the phenomenological model has been implemented by a user-defined material routine, to provide the possibility to carry out fully coupled thermo-mechanical finite element analyses.

For the interfacial region between the pebble beds and container wall, a heat transfer model was

proposed to take into account the thermal contact conductance at different temperatures and stresses. Finally, a benchmark exercise has been carried out on the basis of the present phenomenological model. The results from the simulation have been compared to the experimental data, showing that the present modelling is suitable for thermo-mechanical analyses of fusion blankets.

It will also be shown that for the design and analysis of HCPB blankets, the numerical tools developed in this dissertation are efficient and important. Furthermore, this work also provides a framework to implement further experimental data, such as swelling and degradation of the pebble beds under irradiation, into the material model.

Zusammenfassung

Thermo-Mechanik von Schüttbetten in Fusionsreaktorblankets

Heliumgekühlte Schüttbetten (HCPB: Helium Cooled Pebble Beds) werden in der Ummantelung von Fusionsreaktoren, dem sogenannten Blanket, zur Tritiumerzeugung und als Neutronenmultiplikator verwendet und unterliegen somit harten Einsatzbedingungen. Die Schüttbetten bestehen aus nahezu kugelförmigem Granulat und weisen aufgrund dieser diskreten Beschaffenheit ein komplexes Materialverhalten auf. Eines der wichtigsten Forschungsthemen bei HCPB-Blankets ist die Abhängigkeit der Wärmeleitfähigkeit von der Druckspannung, die durch die thermische Ausdehnung der Schüttbetten im Betrieb hervorgerufen wird. Um den Anforderungen in Hinblick auf Design und Analyse eines HCPB-Blankets gerecht zu werden, wird ein Materialmodell benötigt, das die thermo-mechanische Antwort auf eine äußere Anregung vollständig gekoppelt beschreibt.

In der vorliegenden Dissertation wurden ein numerisches Simulationsverfahren für Schüttbetten unter fusionstypischen Einsatzbedingungen entwickelt. Die Schüttbetten aus Brutkeramik und Beryllium werden dabei mittels der Diskrete-Elemente-Methode und phänomenologischer Ansätze modelliert. Darüber hinaus wird gezeigt, wie vorhandene experimentelle Ergebnisse im Rahmen dieser Vorgehensweise ausgenutzt werden können. Bei der Diskrete-Elemente-Methode werden die einzelnen Granulatkörner unter Gleichgewichtsbedingungen betrachtet. Hierbei wird neben der Anordnung der einzelnen Partikel auch das globale Bauteilverhalten unter Einwirkung makroskopischer Druckbelastung untersucht. Ausgehend von einer zufälligen Packungsdichte als Anfangsbedingung liefert die Simulation die Verteilung der Kontaktbelastung zwischen den einzelnen Partikeln. Die Simulation eines einachsigen Drucktests mit Hilfe der Diskrete-Elemente-Methode ergab dabei eine quantitative Übereinstimmung mit experimentellen Ergebnissen. Darüber hinaus wurden die Beziehungen zwischen mikroskopischen Größen, wie z.B. der maximalen Kontaktbelastung oder der Koordinationszahl im Bauteil zu makroskopischen Belastungsgrößen untersucht.

In einem zweiten Ansatz wurde das globale Materialverhalten unter fusionsähnlichen Bedingungen durch ein phänomenologisches Modell beschrieben, welches die Schüttbetten als kontinuierliches Material betrachtet. Ziel ist die Entwicklung eines Materialgesetzes, das in eine Finite-Elemente-Simulation des Gesamtbauteils eingebunden werden kann. Das thermo-mechanische Materialverhalten wird dabei durch ein nichtlineares Elastizitätsgesetz abgebildet, welches ein modifiziertes Drucker-Prager-Cap Modell sowie eine dehnungsabhängige Wärmeleitfähigkeit beinhaltet. Die benötigten Materialparameter wurden aus vorhandenen experimentellen Ergebnissen abgeleitet. Dieses Vorgehen wurde anhand verschiedener Schüttbett-Varianten angewendet und

für unterschiedliche Temperaturniveaus verifiziert. Darüber hinaus wurde das phänomenologische Modell in eine benutzerdefiniterte Materialroutine implementiert, um vollständig gekoppelte thermo-mechanische FE-Analysen durchführen zu können.

Die Grenzfläche zwischen Granulat und Behälterwand wird durch ein Wärmeübergangsmodell dargestellt, welches die Wärmeleitung im Kontaktbereich bei unterschiedlichen Spannungen und Temperaturen berücksichtigt. In einer Vergleichsstudie wurden die Ergebnisse der Simulation auf Basis des phänomenologischen Modells mit experimentellen Ergebnissen verglichen. Dabei hat sich gezeigt, dass der vorliegende Modellierungsansatz für die thermo-mechanische Analyse eines Fusionsreaktorblankets geeignet ist.

Abschließend wird gezeigt, dass die in der vorliegenden Dissertation entwickelten numerischen Methoden eine effiziente Analyse von HCPB-Blankets ermöglichen und somit ein wichtiges Werkzeug in Hinblick auf das Design derartiger Bauteile darstellen. Darüber hinaus liefert die vorliegende Arbeit die Grundlage, um weitere experimentelle Daten, wie z.B. zum Schwellen oder zur Degradation durch Bestrahlung in das vorhandene Materialmodell für Schüttbetten zu implementieren.

Contents

Symbols

Symbols	Meaning
f_{ave}	average contact force
f_{max}	maximum contact force
h	heat transfer coefficient
k	(1) contraction rate
	(2) thermal conductivity
k_{eff}	effective thermal conductivity of pebble beds
m	mass
n_C	coordination number
p	(1) hydrostatic pressure
	(2) gas pressure
q	(1) von Mises stress
	(2) surface heat flux
t	time
w^c	complementary energy density function
$\mathbf{a}$	acceleration
$\mathbf{e}$ (e_i or e_{ij})	deviatoric strain tensor
$\mathbf{f}$	contact force
$\mathbf{n}$	normal unit vector
$\mathbf{p}$	momenta
$\mathbf{q}$	(1) coordinates for particles
	(2) internal variables
$\mathbf{s}$ (s_i or s_{ij})	deviatoric stress tensor
$\mathbf{t}$	tangential unit vector
$\mathbf{u}$ (u_i)	displacement vector
$\mathbf{v}$	velocity
$\mathbf{x}$	position
E	Young's modulus
G	shear modulus
I	moment of inertia
K	compression modulus
L	side length of a cubic RVE
R	radius of particle
S	surface
T	temperature
V	volume

$\mathbf{C}$ (C_{ij} or C_{ijkl})		stiffness matrix
$\mathbf{F}$		inter-particle force
$\tilde{\mathbf{F}}$		distribution force on surface
$\mathbf{I}$		identity matrix
$\mathbf{L}^{(n)}$		periodic vector
$\mathbf{S}$ (S_{ij} or S_{ijkl})		compliance matrix
$\mathcal{H}$		Hamiltonian
$\mathcal{K}$		kinetic energy
$\mathcal{V}$		potential energy

Greek Symbols

α	accommodation coefficient of gas
β	Drucker-Prager friction angle
ϵ	emissivity
δ	overlapping of two particles
δ_{ij}	Kronecker delta
ϵ_{ijk}	permutation tensor
ζ, ξ, ς	tolerances
η	packing factor
λ	mean free path of gas
$\Delta\lambda$	factor of proportionality
μ	friction coefficient
ν	Poisson's ratio
ρ	power density
τ	shear stress
$\boldsymbol{\epsilon}$ (ϵ_{ij})	micropolar strain tensor
$\boldsymbol{\varepsilon}$ (ε_i or ε_{ij})	strain tensor
$\boldsymbol{\sigma}$ (σ_i or σ_{ij})	stress tensor
$\boldsymbol{\phi}$ (ϕ_{ij})	microrotation tensor
$\boldsymbol{\omega}$	angular velocity vector
$\boldsymbol{\Gamma}$	inter-particle moment

Index

$\square^{cr}$	creep part
$\square^{e}$	elastic part
$\square^{in}$	inelastic part
$\square^{p}$	plastic part
$\square_i$	component of a first-order tensor
$\square_{ij}$	component of a second-order tensor
$\square_{ijk}$	component of a third-order tensor
$\square_{ijkl}$	component of a fourth-order tensor
$\square_N$	normal component
$\square_T$	tangential component
$\square^T$	transpose of matrix

x

Chapter 1

Introduction

Working as tritium breeder and neutron multiplier in fusion reactors, lithium-based ceramic and beryllium pebble beds, respectively, are under severe thermo-mechanical loads. Thus, the thermo-mechanics of these discrete materials is not only essential to understand the behaviour due to external excitations, but also important for the design, characterization and diagnostics of components in fusion reactors. In this chapter, the background of pebble beds is introduced first. The motivation of this work and state of the art in the thermo-mechanics of pebble beds are discussed, and finally a brief description of the chapters in this thesis is given.

1.1 Background

1.1.1 Nuclear fusion and tritium breeding

Research on the peaceful use of nuclear fusion or "thermonuclear reaction" energy started in the middle of the 20th century, mainly in the field of plasma physics. Soon, scientists realized that fusion provides a promising and sustainable solution for the future energy demand (in particular the electricity demand), without long-term radioactive waste and greenhouse gas emissions. Recently, a fusion reactor has become an interesting option, from scientific, technical, social and economic points of view (Stacey, 1984; Wesson, 2004). Since the signing of the agreement of ITER (International Thermonuclear Experimental Reactor, `http://www.iter.org`) on November 21$^{\text{st}}$, 2006, fusion research is carried out in the framework of a worldwide cooperation.

The fusion process releases a large amount of energy, by fusing two light atomic nuclei together to form heavier ones, as

$$D + T \rightarrow {}^4He + n + 17.6 \text{ MeV} , \qquad (1.1)$$
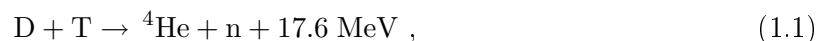
where D and T, namely deuterium and tritium, are isotopes of hydrogen. Other reactions, such as letting deuterium react with itself, or with ^{3}He can also be considered in fusion research. But the high reaction cross-section and high energy yield of the D-T reaction make it the most favorable candidate for fusion reactors. Deuterium is a stable isotope of hydrogen with a natural abundance in the oceans of approximately one atom in 6500 hydrogen. On the other hand, tritium is radioactive, with a relatively short half-life of 12.32 years, and its natural abundance

is negligible. The production of tritium will be economically unfeasible to fulfill the consumption in a fusion reactor. Thus tritium breeding should be considered to fuel the D-T reaction.

Using neutron activation of lithium (Li), tritium can be produced in a nuclear reactor, according to

$$n + {}^6\text{Li} \rightarrow {}^4\text{He} + \text{T} + 4.8 \text{ MeV}$$
$$n + {}^7\text{Li} \rightarrow {}^4\text{He} + \text{T} + n - 2.5 \text{ MeV} \ . \tag{1.2}$$

The reaction with ^{6}Li (with 7.5% natural abundance) is exothermic, and it is possible with neutrons of any energy. The latter one with ^{7}Li (with 92.5% natural abundance) is an endothermic reaction. To utilize the first type of reactions, ^{6}Li enrichment is one important aspect of the breeder material. The neutrons on the right hand side of (1.2) are the outcome of fusion reaction (1.1).

In Figure 1.1, a fusion reactor is drawn schematically. In the reactor core, D-T reactions take place at temperatures exceeding 10^8 °C. Neutrons pass through the first wall and interact with the lithium in the reactor blanket, thus breeding further tritium in situ. Tritium is collected from the blanket, and cycled back into the reactor core. A coolant flowing through the blanket removes the heat so as to generate electricity.
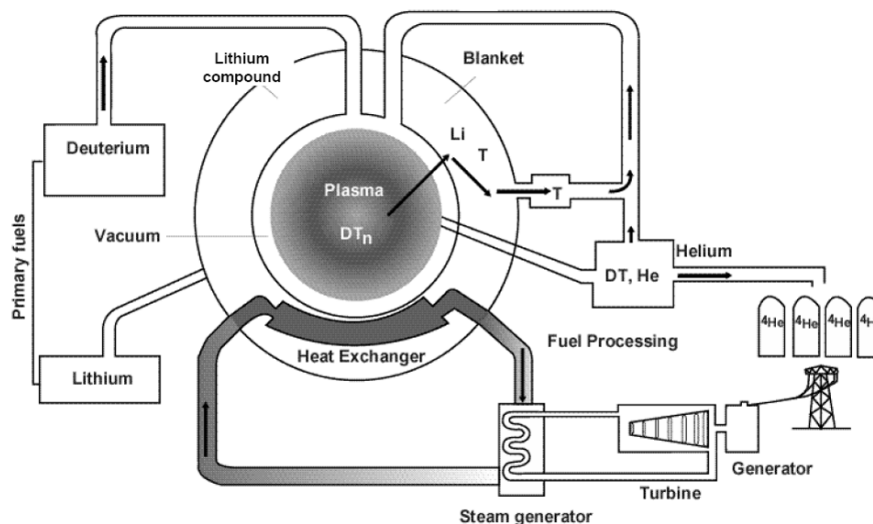
Figure 1.1: A schematic drawing of the fusion fuel cycle.

1.1.2 Breeding blankets for fusion reactors

In a fusion reactor, neutrons carrying 80% of the produced energy will be absorbed in a blanket surrounding the reactor core. This blanket contains lithium as breeding material in the form of a liquid or solid. Due to the number and the tritium breeding efficiency of neutrons, it is necessary to introduce extra elements (such as beryllium and lead) into the blankets working as neutron multipliers. Hence, the tritium breeding ratio (TBR) can be increased to more than 1.0, making the blanket self-sufficient for the tritium fuel cycle.

Based not only on different tritium breeding and structural materials, but also cooling strategies, there are several design concepts for breeding blankets. In ITER, there are possibilities to

investigate test blanket modules (TBM) to realize the fuel cycle. These modules allow the testing of design concepts for tritium breeding blankets at high temperatures relevant to a future fusion power reactor, and in particular to the next step (DEMO) beyond ITER (Giancarli et al., 2006). In the EU, helium-cooled pebble beds (HCPB) and helium-cooled lithium-lead (HCLL) blankets will be tested in ITER (Poitevin et al., 2005; Andreani et al., 2006). Furthermore, with parameters observed in ITER, schemes of design, predictive tools and diagnostics can be validated and developed to be used in DEMO. Among these design concepts, solid breeder blankets (such as HCPB) provides the most promising near-term options for fusion reactors.

There are three main functions of HCPB blankets: besides transformation of the neutron energy originating from the fusion reaction into usable heat and shielding of the superconducting magnets against neutron and gamma radiation, its main purpose is breeding of the fuel tritium by capturing neutrons in lithium (Boccaccini et al., 2002; Hermsmeyer et al., 2003). The HCPB blanket is split into several layers filled with breeder and neutron multiplier pebble beds. Figure 1.2 shows a typical design for a breeder unit in the European HCPB-TBM module.
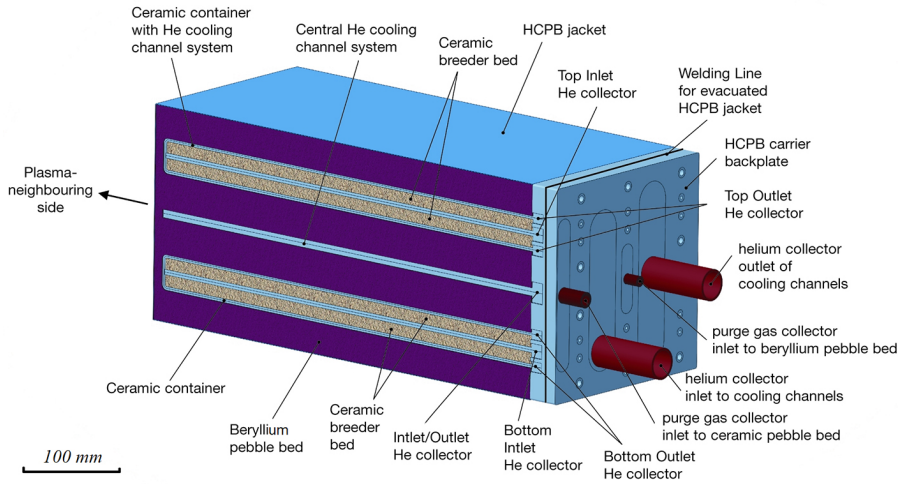
Figure 1.2: A breeder unit in the HCPB test blanket module.

1.1.3 Tritium breeder and neutron multiplier pebbles

The pebble beds in HCPB blankets are composed of nearly spherical shaped pebbles, whose diameters range from 0.25 to 2 mm (Reimann et al., 2002). The size of pebbles is selected in the breeder blankets, according to the following reasons: 1) small pebbles get small thermal gradients under large heat generation, which reduces the thermal stresses inside the pebble; 2) larger brittle ceramic particles are weaker than smaller ones; 3) generated tritium can be recovered by purge gas flowing between pebbles; 4) small spherical pebbles can be handled easily in plants. However, thermal conductivities of these materials composed of discrete particles depend strongly on the mechanical field. Under fusion-relevant conditions, special emphasis should be placed on such coupled thermo-mechanical properties.

Candidates for tritium breeder pebbles include lithium orthosilicate (Li_4SiO_4), lithium titanate (Li_2TiO_3), etc. Beryllium and its compounds, such as $Be_{12}Ti$, are good neutron multiplier pebbles. Their typical fabrication methods are listed in Table 1.1. Figure 1.3 shows optical micrographs of Li_4SiO_4 pebbles (Knitter, 2008). The diameters of different types of pebbles are

on the order of magnitude of 1 mm, which is much smaller compared to the dimension of a typical HCPB-TBM structure, as shown in Figure 1.2.

Table 1.1: Types of pebbles and their typical fabrication methods

Types	Fabrication Method	Diameter (mm)	Ref.
Li_4SiO_4	melting-spray method (*)	0.25-0.63	Knitter et al. (2007)
Li_2TiO_3	wet process	0.2-2.0	Tsuchiya et al. (2005)
$Be/Be_{12}Ti$	rotating electrode method (**)	1.0	Kawamura et al. (2002)

(*) Schott, Germany; (**) NGK, Japan.
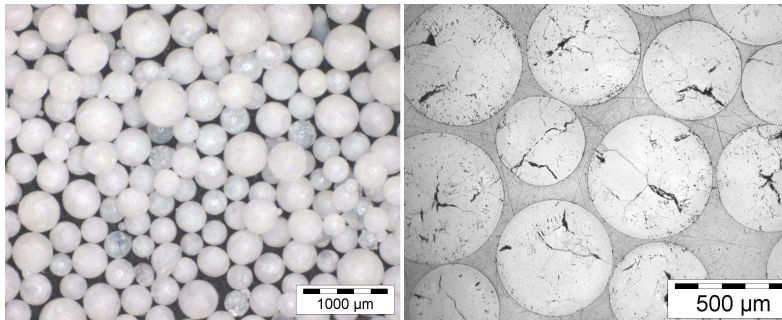
Figure 1.3: Optical micrographs of Li_4SiO_4 pebbles: left, overview; right, cross-section.

1.2 Motivation and state of the art

Under fusion-relevant conditions, pebble beds are not only subject to severe conditions, such as neutron irradiation and high heat flux, but they also show complex behaviour caused by their discrete nature. Due to the extreme working conditions in the fusion reactor, a deep understanding of the thermo-mechanical properties of these pebble beds is essential. Thus, a material model for describing their response to the external excitation is needed, to check the requirements in design and analysis of HCPB blankets.

The thermo-mechanical loads inside the pebble beds include the following: volumetric heating, heat sink and mechanical loads. One of the most important issues in the design and analysis of HCPB blankets is that the effective thermal conductivity of pebble beds is changed according to compressive stresses, which are introduced by the thermal expansion of pebbles during operation. When the thermal conductivity of packed beds varies, it affects in turn the stress distribution by changing the temperature distribution. The temperature field is important not only because of the induced thermal stresses and creep deformations inside pebble beds, but also because of the functionality of those materials, such as tritium invention and release rates. On the other hand, thermal stresses could increase the crush probability of single pebbles, as a result of inter-particle contact forces. Therefore, it is necessary to perform stress analysis and thermal analysis simultaneously, with a material model describing the coupled properties.

Another important type of loading on pebble beds is the neutron irradiation, although the experimental data on this effect are far from sufficiently up to date. The high level of neutron

irradiation can result in not only instantaneous volumetric heating of the pebble beds, but also in the swelling and degradation of each single pebble. The induced volumetric heating can be estimated by means of neutronics (Fischer et al., 2007). The irradiation effects on the mechanical behaviour can be taken into account based on the post-irradiation examination of pebble beds, such as uniaxial compression tests (UCT, or oedometric compression) on irradiated pebble beds. To adjust the material model according to both the type and conditions of pebble beds, an identification method of material parameters is needed.

For thermo-mechanical modelling of pebble beds, there are several recent approaches under development. The strategies of modelling pebble beds include: (i) modelling individual interactions between pebbles and (ii) phenomenological modelling. With the first type of modelling, by means of the so-called discrete element method, the contact interactions and rearrangements of particles are analyzed in view of the constitutive modelling of pebble beds. With this approach, the situation of individual particles can be explained through an understanding of the links between macroscopic and microscopic variables. For instance, the macroscopic plastic strain, as one of the phenomenological quantities, can be accounted for by both plastic deformation and rearrangement of particles. Moreover, contact forces are important to characterize the crush probability of single pebbles, which can be obtained explicitly by a discrete element simulation.

The second type of modelling, considering materials composed of particles as continuous media, is the thermo-mechanical modelling in the framework of continuum mechanics. For engineering applications, such as design and structural characterization, numerical studies with the help of the finite element method are desired. Therefore, a constitutive model using continuum mechanics and its implementation into finite element codes are essential. Due to the fact that the characteristics of pebble beds are sensitive to different factors, such as properties of bulk materials of pebbles, initial configurations and, in addition, levels of neutron irradiation, it is important to identify the material parameters from limited types of experiments. In addition to the bulk region of the pebble beds, the interface between pebbles and container wall is important due to the fact that the near-wall region reduces the thermal conductance by not only introducing interfacial thermal contact resistance but also by changing the packing of pebbles.

1.3   Overview of chapters

In the present work, after reviewing related work in Chapter 2, we start with micro-mechanics of pebbles. With the help of the discrete element method, the interactions between individual pebbles are studied. For discrete element calculations, a method to obtain reasonable initial packing is essential. An important first step towards the simulation of assemblies of pebbles, under periodic boundary conditions, is presented and discussed in Chapter 3. To represent the thermo-mechanical behaviour of pebble beds on the engineering scale, a phenomenological model is introduced in Chapter 4, including nonlinear elasticity, plasticity and creep. Moreover, the effective thermal conductivity, depending on both inelastic volumetric strain and temperature, is employed in the material model in order to be able to perform fully coupled thermo-mechanical analyses. In Chapter 5, to determine the material parameters in the present phenomenological model from available experimental data, an identification method is proposed. With this method the phenomenological model is validated for different types of pebble beds. In Chapter 6, a user-defined material routine is introduced to implement a general phenomenological model into finite

element codes, including elasto-plasticity and thermo-mechanical behaviour. In addition to the bulk region of pebble beds, the interfacial region between the structural container material and pebbles is modelled in Chapter 7, with emphasis on interfacial heat transfer. In Chapter 8, a fully coupled analysis of a benchmark exercise is performed as an application of the present material model. Finally, a summary of this work is made in Chapter 9.

Chapter 2

Related Work

In this chapter, related work on the thermo-mechanics of pebble beds is reviewed. A pebble bed is a collection of a large number of discrete particles, on which the phenomenological behaviour of the material depends strongly. Therefore, characterizations of both single pebbles and pebble beds are mentioned in the first section. Then the existing thermo-mechanical modelling efforts are discussed, including discrete element and continuum mechanics approaches. In the third section, mock-up experiments of pebble beds and benchmark activities of material models are introduced. Finally, the objectives of this work are presented briefly.

2.1 Characterizations

As a granular material, the overall properties of pebble beds depend not only on the bulk material, but also on the topology of pebbles in the packed state. Here we focus on the characterizations of mechanical and thermal behaviour.

2.1.1 Single pebbles

The characterizations of single pebbles include: properties of the bulk material, microstructure, pebble size distribution, density and porosity, compressive crush load test, and chemical and phase analyses (Reimann et al., 2006a).

Mechanical properties and thermal conductivity of bulk ceramic breeder and neutron multiplier materials have been studied, e.g., Dienst and Zimmermann (1988) and Zimmermann (1989). The crush load of single pebbles is one important issue for ceramic breeder pebbles (Piazza et al., 2001b; Tsuchiya et al., 2006). The average crush load of dried Li_4SiO_4 pebbles with diameter of 0.5 mm is about 7-8 N with 20% scattering. The scattering of data is mainly caused by randomly distributed voids and micro-cracks during rapid cooling in the course of the melting-spray method (Knitter et al., 2007). Experimental investigation shows that thermal shock is not an issue for blanket relevant temperature gradients in the range of $5^oC/s$ (Reimann et al., 2005a). For these properties, the database has been well established for un-irradiated materials. On the contrary, limited post-irradiation examinations of pebbles have been performed recently by Scaffidi-Argentina et al. (2000) and Piazza et al. (2004).

2.1.2 Pebble beds

To characterize the mechanical response of pebble beds to the external excitation, uniaxial compression tests (UCT, or oedometric compression) have been carried out using different types of pebbles at different bed temperatures (Reimann et al., 2000a). The empirical stress-strain curves are given based on experimental data. Nonlinear elasticity, overall plastic deformation and hardening are typical observations in experiments. Some biaxial experiments are available in literature (Hermsmeyer and Reimann, 2002), which provide additional information, such as inner friction angle of the beds. This type of experiments, and even more tri-axial experiments, are elaborate to be performed, especially on a large scale to minimize wall effects. To obtain the time-dependent behaviour of pebble beds, creep experiments have been conducted at different temperatures and compressive stresses. For beryllium pebble beds, Reimann and Harsch (2004) have investigated the creep properties of a bed with an average temperature ranging from 450 to 650 ^oC and compressive stresses up to 3.6 MPa. The correlations for creep properties of lithium orthosilicate and lithium metatitanate are obtained by Reimann and Worner (2001) and Piazza et al. (2002).

One of the most important phenomena of compressed pebble beds is that the effective thermal conductivity depends on not only the average bed temperature but also on mechanical quantities, such as inelastic strains. The effective thermal conductivity of beryllium pebble beds has been measured under different compressive stresses and temperatures (Reimann et al., 2000b; Abou-Sena et al., 2003; Piazza et al., 2003; Reimann et al., 2005b, 2006b), and the correlation has been given as a function of both average bed temperature and volumetric compressive strain. Abou-Sena et al. (2005) have reviewed the existing data of effective thermal conductivity for different types of ceramic breeder pebble beds. For ceramic breeder pebble beds, the strain dependence of the effective thermal conductivity is rather modest, compared to the one of beryllium pebble beds (Piazza et al., 2001a; Reimann and Hermsmeyer, 2002; Abou-Sena et al., 2003). This can be explained through an understanding of different mechanisms of heat transfer inside a packed bed (Chan and Tien, 1973; Batchelor and O'Brien, 1977; Hsu et al., 1994), such as the heat transfer through the contact zone between two particles. Ceramic breeder pebbles have much lower bulk thermal conductivity than beryllium pebbles, and hence ceramic breeder pebble beds are less sensitive to the changing of the mechanical loading. Concerning this property, the coupled thermo-mechanical analysis has to be taken into account to represent the thermal stresses and temperature distribution of a pebble bed.

2.1.3 Interfacial region

In the interfacial region between the bulk pebble bed and container wall, additional heat transfer resistance is introduced (Madhusudana, 1995). The interfacial heat transfer coefficient (HTC) is important for a coupled thermo-mechanical analysis of the typical HCPB-TBM structure, with the aim of investigating the influence of pebble beds and predicting the temperature distribution.

Experimental investigations have been carried out for ceramic breeder (Dalle Donne and Sordon, 1990; Tehranian et al., 1994; Tehranian and Abdou, 1995) and beryllium pebble beds (Dalle Donne et al., 2000; Abou-Sena et al., 2003). The additional temperature drop at the interface is calculated by extrapolating the bed temperature at the interface. The data scattering

of temperature measurements brings inaccuracy of the values of HTCs. Modelling the effects in this region can be traced back to the investigation of packed beds (Schlünder, 1982; Peterson and Fletcher, 1988; Kikuchi, 2001). With different assumptions, these models investigate the effects of the first layer of pebbles next to the container wall. Reimann et al. (2005a) developed a HTC model for pebble beds based on Schlünder's model, without taking into account the effect of mechanical pressure. Chan and Tien (1973) investigated the influence of different packing structures on the effective thermal conductivity. It is well known that a container wall varies the local packing structure of the pebble bed. Therefore, the near-wall topology will change the effective thermal conductivity, and consequently induce additional heat transfer resistance in the near-wall region. Recently, with the help of microtomography, the topology of packed pebbles has been investigated (Reimann et al., 2006c).

2.2   Modelling

Similar to sand and soil, pebble beds can be modelled by either a discrete element method or a continuum approach. The aim of both approaches is to represent the constitutive behaviour of the material in the framework of different models. The agreement between prediction of models and experimental results, such as the uniaxial compression test, is the key to show the applicability of material models.

Besides the similarities to the plastic behaviour of metals, namely, nearly rate independent plastic deformation and yield stress, granular materials have relatively strong dependence on pressure and volume changes. Increasing the hydrostatic pressure on a granular material can introduce further irreversible deformation which can be accompanied by a reduction in volume. The changes in volume can either harden or soften the material assemblies. Another common feature of granular materials is the dilatancy under shear stresses. When sheared, the interlocking particles in a compacted state move and produce a bulk expansion of the material. Appropriate non-associated plastic flow theories are hence needed to predict this behaviour. The overall plastic deformation of pebble beds results from a combination of the plastic deformation of individual pebbles and the irreversible rearrangement of pebbles.

Furthermore, other behaviour, like effective thermal conductivity and thermal expansion, depends sensitively on the packing and inter-particle force chains in the granular materials (Jaeger et al., 1996). To describe these properties, both a micro-mechanical description and a phenomenological model can be employed. The link between these micro- and macro-quantities can be studied by concurrent multiscale modelling. However, as sequential multiscale modelling, a micro-mechanics based phenomenological model for granular materials remains rare in literature.

2.2.1   Discrete element method

The discrete element method (DEM), or distinct element method, was first introduced by Cundall and Strack (1979) to study the mechanical response of assemblies consisting of discrete particles. DEM has been employed in either dynamic or static analyses of granular media (Herrmann and Luding, 1998). Using this method, the deformation, as well as the internal force distribution of the assembly can be obtained numerically (Thornton and Antony, 1998; Antony,

2000; Redanz and Fleck, 2001; Martin et al., 2003; Martin, 2004; Gilabert et al., 2007). These types of information are crucial to understand the mechanism of macroscopic behaviour of granular media, such as the yield surface (Redanz and Fleck, 2001) and the crush probability of single particles inside an assembly (Marketos and Bolton, 2007).

Some early approaches have made some assumptions to simplify the problem under consideration, such as using two-dimensional cases, or simulating limited number of particles contained by rigid walls. However, these assumptions would not be valid if DEM is applied to pebble beds in fusion blankets.

With the help of DEM, thermal creep of a ceramic breeder pebble bed has been investigated by a 3D discrete numerical thermo-mechanics code (Lu et al., 2000; Ying et al., 2002). Recently, the contact force distribution inside pebble beds has been investigated by An et al. (2007a,b). For these existing studies, six rigid walls are applied as boundaries for the assembly. Initial packing factors reached in these investigations are 60±0.5%. This range is below the reference value. To provide a representative result, and to eliminate the effect of a rigid wall at the same time, a large number of particles should be considered. Periodic boundary conditions are hence essential to perform the discrete element simulation (Gilabert et al., 2007). Other researchers (Aquaro and Zaccari, 2005, 2006) simplify the particles in regular lattices as beam elements, which represent the interaction forces between pebbles, and the overall response can be obtained. By using regular lattices, analytical solutions can be obtained, and the initial packing factor can be varied by using different types of lattices. However, this approach eliminates the influence of the rearrangement of particles, which is another important factor to understand the overall plastic strains of the assembly.

Considering the microstructure of pebble beds, the deformation mechanism can be clearly revealed by DEM approaches, including mechanical behaviour and thermal creep. The physical meanings of some phenomenological material parameters, such as strain-dependent thermal conductivity, can be explained through an investigation of assemblies consisting of particles. But on the other hand, the problem remains that, for example, the complexity of the microstructure and the plastic contact of pebbles are still idealized in this approach. Moreover, engineering applications of DEM into large scale structures, such as a HCPB-TBM blanket, will not be practical without the help of continuum mechanics.

2.2.2   Continuum mechanics

In the second type of modelling, pebble beds being composed of numerous discrete particles are assumed to be continuous media. To take into account the typical material behaviour in engineering analyses, a corresponding phenomenological constitutive model can be exploited in the framework of the finite element method. By investigating granular materials, many different models have been developed in soil mechanics, such as Mohr-Coulomb theory, the Drucker-Prager-Cap model (Drucker and Prager, 1953) and Cam-Clay model (Roscoe and Burland, 1968). They are typically pressure-dependent plasticity models, with non-associated plastic flow rules (Khan and Huang, 1995; Vardoulakis and Sulem, 1995; Collins and Houlsby, 1997). It should be noted that whether it is appropriate to use a continuum approach depends on the ratio of the size of the microstructure, i.e. an individual particle, compared to the dimension of the component under investigation.

In the activities of Forschungszentrum Karlsruhe (FZK), the modified Drucker-Prager-Cap model, which is one of the most frequently used models in soil mechanics, has been applied as the constitutive model for pebble beds (Bühler, 2002; Reimann et al., 2002; Hofer and Kamlah, 2005). The predictions of the model generally agree with the experiments, if the material parameters are chosen properly. However, in some specific cases, unrealistic plastic softening behaviour of the Drucker-Prager-Cap model during unloading is observed. Vella et al. (2001) and Di Maio et al. (2002) have used both the Drucker-Prager-Cap model and the Gurson model for porous materials (Gurson, 1977) as plasticity laws, combined with a so-called hyperporous elasticity law to analyze benchmark experiments. Motivated by experimental results and by the empirical loading and unloading curves by Reimann, Fokkens (2003) has applied two different elasticity laws for the loading and unloading branches. This model has been implemented in the finite element code, MSC.MARC, and is used to analyze the thermo-mechanical behaviour of the pebble bed assembly (PBA) during pre-compaction and start-up procedures (see Section 2.3).

To implement a general material model, interfaces for user-defined material routines are usually provided by finite element codes, e.g., ABAQUS (2004a). Return mapping algorithms are used as integration schemes for constitutive equations of elasto-plasticity with non-associated plastic flow rules (Ortiz and Popov, 1985; Ortiz and Simo, 1986; Ortiz and Martin, 1989; Keavey, 2002; Ahadi and Krenk, 2003). With this approach, newly developed material models can be used to analyze the thermo-mechanical behaviour of pebble beds. Moreover, achievements in DEM, such as a micro-mechanics based constitutive law, can be utilized by the finite element method.

2.3   Mock-up experiments and benchmark

To investigate the thermo-mechanical properties of pebble beds under fusion relevant conditions, in-pile (van der Laan et al., 2000a, 2002; Piazza et al., 2004) and out-of-pile mock-up experiments (Dell'Orco et al., 2004; Ying et al., 2007) are carried out in EU associations.

For in-pile experiments, the pebble bed assembly (PBA) and EXOTIC experimental series are two typical examples in NRG Petten. Due to limitations of the space in high flux fission reactors, comparably small capsules are used. In such cases, the ratio of the diameter of pebbles to the dimension of capsules is too large to represent the overall behaviour of pebble beds. As out-of-pile mock-up experiments, HELICA and HEXCALIBER have been launched in ENEA Brasimone (Dell'Orco et al., 2006; Tincani et al., 2006). For those experiments, the pebble layers are heated by electric heaters, and temperature and displacement have been measured.

Using different types of phenomenological models, the overall behaviour of the lithium orthosilicate cassette (HELICA) and the interactions of ceramic breeder and beryllium pebble beds (HEXCALIBER) can be studied numerically. The predictions can be compared with the measurements from the mentioned out-of-pile experiments, to check validity of material models proposed by different EU associations. Proper phenomenological models will be used as one type of the predictive tools for the design and diagnostics of HCPB-TBM blankets under ITER or DEMO relevant conditions.

2.4   Objectives of this work

The main objective of this work is to develop a reliable and effective thermo-mechanical model for simulating pebble beds under fusion relevant conditions. To achieve this goal in this thesis, we first study the mechanisms of the deformation and stress state inside a pebble bed. The rearrangement of particles and the interaction forces, obtained numerically in a discrete element simulation, are two key issues to understand the overall mechanical responses of pebble beds.

A finite element based simulation is best suited for engineering applications. A phenomenological model, based on the modified Drucker-Prager-Cap model, is proposed to satisfy the requirements for simulations. Unique identification of material parameters from available experimental results is another important issue, to avoid ambiguity and unnecessary efforts using trial-and-error methods. Moreover, to provide the possibility to implement new phenomenological models for pebble beds in the future, for example, a micro-mechanics based model using DEM, a user-defined material routine is introduced with emphasis on fusion relevant thermo-mechanical modelling. Furthermore, the material model is used to compare the predictions to the available benchmark experiments.

Chapter 3

Discrete Element Simulation

The discrete element method (DEM), or distinct element method, is a numerical method to simulate the mechanical response of a system composed of discrete particles (Cundall and Strack, 1979; Cundall, 1988), and it is suitable to study granular materials as the pebble beds considered in this work. In this chapter, first, the basic theory of the discrete element method will be briefly introduced. A stress average method is presented here to link the interactions between individual particles to the macroscopic stress state of the assembly. Some discussion concerning solution techniques will be made. In the application to the pebble bed system, an algorithm of random close packing is used to prepare initial configurations of pebbles in a reasonable range of packing factors. Finally, discrete element simulations are made to represent the uniaxial compression test of pebble beds.

3.1 Theory

The discrete element method is applied to simulate the assembly of particles, in which it allows finite displacement and rotation of discrete bodies, including complete detachment. DEM is developed based on the idea that discrete particles could be displaced independently from one another and interact with each other only at contact points. Contact laws are applied to describe inter-particle forces, i.e. normal and friction forces. New contacts can be automatically detected. The interaction in the assembly is monitored contact by contact, and the motion of particles is modelled particle by particle. Here, we first discuss the energy description of the assembly, interaction laws and equations of motion.

3.1.1 Energy in the assembly

The microscopic state of a system may be specified in terms of the positions and momenta of an assembly of particles. In the classical description, we may write the Hamiltonian $\mathcal{H}$ of a system of N particles as a sum of kinetic and potential energy functions of the set of coordinates $\mathbf{q}^{(i)}$ and momenta $\mathbf{p}^{(i)}$ of each particle i (Allen and Tildesley, 1987). Adopting a condensed notation

$$\mathbf{q} = (\mathbf{q}^{(1)}, \mathbf{q}^{(2)}, \dots, \mathbf{q}^{(N)})$$
$$\mathbf{p} = (\mathbf{p}^{(1)}, \mathbf{p}^{(2)}, \dots, \mathbf{p}^{(N)}) \, , \tag{3.1}$$

we have

$$\mathcal{H}(\mathbf{q}, \mathbf{p}) = \mathcal{K}(\mathbf{p}) + \mathcal{V}(\mathbf{q}) \ . \tag{3.2}$$

The kinetic energy $\mathcal{K}(\mathbf{p})$ and the potential energy $\mathcal{V}(\mathbf{q})$ are discussed in the following.

The kinetic energy $\mathcal{K}$

The kinetic energy depends on the momenta p_α and angular momenta p_β of the particles inside the assembly. In classical mechanics, momentum is the product of the mass m and velocity $\dot{\mathbf{x}}$ of an object. For an object with a fixed mass that is rotating about a fixed symmetry axis, the angular momentum is expressed as the product of the moment of inertia I of the object and its angular velocity vector $\boldsymbol{\omega}$.

Therefore, it is convenient to split the total kinetic energy of one body into the sum of its center-of-mass translational kinetic energy and the energy of rotation around the center-of-mass. The total kinetic energy $\mathcal{K}$ can be obtained by summing up the individual energy of all particles

$$\mathcal{K} = \sum_{i=1}^{N} \Big[\sum_{\alpha} \frac{(p_\alpha^{(i)})^2}{2m^{(i)}} + \sum_{\beta} \frac{(p_\beta^{(i)})^2}{2I^{(i)}} \Big] \ . \tag{3.3}$$

In a quasi-static system, the kinetic energy is ignorable, but this quantity can be used for a convergence check in the calculation, i.e. whether the quasi-static state has been reached. The value mainly reflects the proximity to equilibrium of the system. Granular materials dissipate energy quickly (Richard et al., 2005), thus damping mechanisms are needed in discrete element simulation to represent this process.

The potential energy $\mathcal{V}$

The potential energy contains the interesting information regarding inter-particle interactions, such as the normal contact and tangential friction forces. We have

$$\mathcal{V} = \sum_{I=1}^{N} \sum_{J} \phi^{(I,J)} \ . \tag{3.4}$$

The superscript J indicates the particle in contact with the I-th particle and $\phi^{(I,J)}$ is the potential of the interaction between the I-th and J-th particles. If only the normal contact forces are present in the particle assembly, then

$$\phi^{(I,J)} = \int_0^{\delta} f_N^{(I,J)} \, \mathrm{d}\delta \ . \tag{3.5}$$

Here, $\delta = |\mathbf{x}^{(I)} - \mathbf{x}^{(J)}| - (R^{(I)} + R^{(J)})$ denotes the overlapping of two contacting spherical particles, and $R^{(I)}$ is the radius of the I-th particle. $f_N^{(I,J)}$ is the normal contact force between the I-th and J-th particles. The exact expression depends on the contact law applied in the calculation.

3.1.2 Kinematics of contacting points

In order to obtain not only the relative normal velocities but also the direction of the friction force between two contacting particles, the kinematics of the contacting points is described here. Two contacting particles are schematically shown in Figure 3.1. The contact normal $\mathbf{n}$ between the contacting particles, namely, the I-th and J-th particles, is given by

$$\mathbf{n} = \frac{\mathbf{x}^{(J)} - \mathbf{x}^{(I)}}{\left|\mathbf{x}^{(J)} - \mathbf{x}^{(I)}\right|} \ . \tag{3.6}$$

The velocity of the contact point is contributed to by both the translation and rotation of the particle. For particle I, the velocity $\dot{\mathbf{x}}^R$ of contact point A, due to the rotation velocity $\boldsymbol{\omega}$, can be expressed as

$$\begin{aligned} \dot{\mathbf{x}}^R &= \boldsymbol{\omega} \times \mathbf{R} \\ \dot{x}_i^R &= \epsilon_{ijk}\, \omega_j\, n_k R \ , \end{aligned} \tag{3.7}$$

where ϵ_{ijk} is the permutation tensor as

$$\epsilon_{ijk} = \begin{cases} 1: & \text{if } ijk \text{ is an even permutation of } (1\ 2\ 3) \\ -1: & \text{if } ijk \text{ is an odd permutation of } (1\ 2\ 3) \\ 0: & \text{otherwise.} \end{cases} \tag{3.8}$$

Therefore, for two contacting particles, the relative velocity $\Delta\dot{\mathbf{x}}^{(I,J)}$, considering combined translation and rotation of both particles, is described as

$$\begin{aligned} \Delta\dot{\mathbf{x}}^{(I,J)} &= \left[\dot{\mathbf{x}}^{(I)} - \dot{\mathbf{x}}^{(J)}\right] + \left[\boldsymbol{\omega}^{(I)} \times \mathbf{R}^{(I)} - \boldsymbol{\omega}^{(J)} \times \mathbf{R}^{(J)}\right] \\ &= \left[\dot{\mathbf{x}}^{(I)} - \dot{\mathbf{x}}^{(J)}\right] + \left[\boldsymbol{\omega}^{(I)} R^{(I)} + \boldsymbol{\omega}^{(J)} R^{(J)}\right] \times \mathbf{n} \ . \end{aligned} \tag{3.9}$$

Using the above expression of the contact normal $\mathbf{n}$ and the relative velocity $\Delta\dot{\mathbf{x}}^{(I,J)}$, the friction force can be defined by the tangential component of $\Delta\dot{\mathbf{x}}^{(I,J)}$. The normal and tangential (or sliding velocity) components, respectively, can be expressed as

$$\begin{aligned} \Delta\dot{\mathbf{x}}_N &= \left(\Delta\dot{\mathbf{x}}^{(I,J)} \cdot \mathbf{n}\right) \mathbf{n} \\ \Delta\dot{\mathbf{x}}_T &= \Delta\dot{\mathbf{x}}^{(I,J)} - \Delta\dot{\mathbf{x}}_N \ . \end{aligned} \tag{3.10}$$

With these relations, the rate-dependent interaction and the friction force can be implemented in the DEM code.

3.1.3 Tangential interactions

Usually, the friction force has a direction opposite to the sliding velocity $\Delta\dot{\mathbf{x}}_T$. The magnitude can be defined by different assumptions. For instance, the friction force applied to the I-th particle can be written as (Bicanic, 2004)

$$\mathbf{f}_T^{(I,J)} = -\frac{\Delta\dot{\mathbf{x}}_T}{|\Delta\dot{\mathbf{x}}_T|} \min\left(\mu\, f_N^{(I,J)},\, k_s\, |\Delta\dot{\mathbf{x}}_T| \cdot \Delta t\right) \ . \tag{3.11}$$

Here, μ is the friction coefficient of the contacting surfaces, k_s represents the coefficient in the case of small tangential displacement (proportional to the sliding velocity). The second part gives a smooth transition at the region of low relative tangential velocity $|\Delta\dot{\mathbf{x}}_T|$.

15
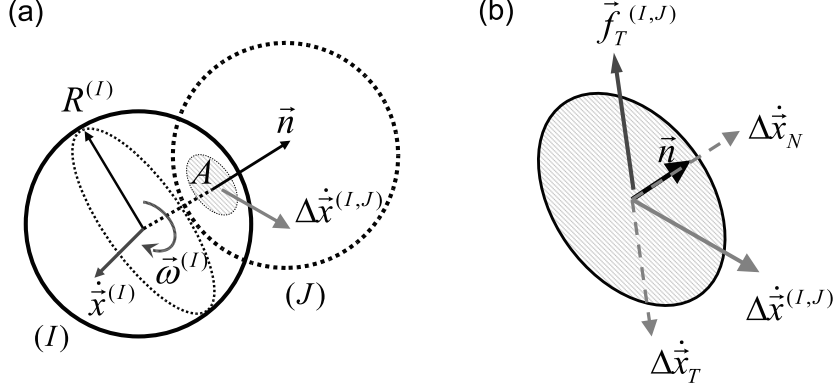
Figure 3.1: (a) Kinematics of two contacting particles; (b) decomposition of the relative velocity in the contact region A.

3.1.4 Normal interaction

In this investigation, we consider only the elasticity of the bulk material, and the particles are assumed to be spherical-shaped. Thus, the classical Hertzian solution (Johnson, 1985) can be employed depending on the elastic properties of the contacting particles, i.e. I-th and J-th in the assembly, by

$$\mathbf{f}_N^{(I,J)} = -\frac{4}{3}E^*\sqrt{R^*}\delta^{3/2} \cdot \mathbf{n} \ . \tag{3.12}$$

Here, E^* and R^* are the effective Young's modulus and the reduced radius, respectively, defined as

$$\frac{1}{E^*} = \frac{1-(\nu^{(I)})^2}{E^{(I)}} + \frac{1-(\nu^{(J)})^2}{E^{(J)}}, \quad R^* = \frac{R^{(I)}R^{(J)}}{R^{(I)}+R^{(J)}}.$$

For inelastic contact laws, there are different approaches in literature. Concerning the visco-plasticity properties of the bulk material, Storakers et al. (1999) have provided a solution using the total strain, which can be easily implemented in the present framework of the discrete element method. In order to take into account the elastic unloading path, Mesarovic and Johnson (2000) have investigated adhesive contact between elasto-plastic spheres, including the simplest case of the solution of the perfect elasto-plastic contact. Kruggel-Emden et al. (2007) have reviewed the existing inter-particle contact laws used in discrete element methods.

3.1.5 Equations of motion and their solution

For the I-th particle, the time evolution of the degrees of freedom is governed by the equations

$$m^{(I)}\ddot{\mathbf{x}}^{(I)} = \sum_J \mathbf{F}^{(I,J)} \ ,$$
$$I^{(I)}\dot{\boldsymbol{\omega}}^{(I)} = \sum_J \boldsymbol{\Gamma}^{(I,J)} \ . \tag{3.13}$$

Here, $\mathbf{F}^{(I,J)}$ and $\boldsymbol{\Gamma}^{(I,J)}$ denote the inter-particle force and moment from the J-th particle on the I-th one. The first term, $\mathbf{F}^{(I,J)}$, includes the contributions of normal force $\mathbf{f}_N^{(I,J)}$ and tangential force $\mathbf{f}_T^{(I,J)}$.

The most widely used method for integrating the equations of motion is the algorithm initially adopted by Verlet (1967). Swope et al. (1982) proposed a Verlet-equivalent algorithm, which stores positions, velocities and accelerations all at the same time t. This "velocity Verlet" algorithm takes the form

$$\mathbf{x}(t + \delta t) = \mathbf{x}(t) + \delta t \mathbf{v}(t) + \frac{1}{2} \delta t^2 \mathbf{a}(t)$$
$$\mathbf{v}(t + \delta t) = \mathbf{v}(t) + \frac{1}{2} \delta t \big[\mathbf{a}(t) + \mathbf{a}(t + \delta t) \big] \ . \tag{3.14}$$

In this form, the method resembles a three-value predictor-corrector algorithm. This method has the advantages of numerical stability, convenience and simplicity, which make it perhaps the most attractive one up to date (Allen and Tildesley, 1987). The rotational degrees of freedom can be treated in a similar way, by using general positions $\tilde{\mathbf{x}}$, velocities $\tilde{\mathbf{v}}$ and accelerations $\tilde{\mathbf{a}}$ like in Eqn. (3.14).

Another important issue is the time step of each iteration for the explicit scheme. In this work, the time step is determined using the method proposed by Cundall and Strack (1979) as

$$\delta t = 2 f_t \sqrt{\frac{m_0}{K_0}} \ , \tag{3.15}$$

where f_t is less than unity to ensure stability of the calculation, m_0 is the smallest particle mass and K_0 is the maximum contact stiffness, defined by the contact law. We use $f_t = 0.4$, and thus a typical value of δt is around 10^{-7} s. The simulation for quasi-static deformation can be carried out either using a global damping method (Cundall and Strack, 1979) or by scaling the density of the particles by a factor of β with a typical value of $\beta = 10^{12}$ (Thornton and Antony, 1998). The details will be discussed later in Section 3.3.

3.2 Micro-macro relations

The objective of this section is to determine the relation between the contact forces obtained in the discrete element calculation and the macroscopic stress tensor. This relation is necessary to link quantities from length scales of particle and bed, and, thus, helps to understand the physics behind the macroscopic behaviour.

3.2.1 Volume average stress

In micro-mechanics, the unweighted volume average stress, taken over the volume V of the representative volume element (RVE), denoted by $\overline{\boldsymbol{\sigma}}$ is defined as

$$\overline{\boldsymbol{\sigma}} \equiv \frac{1}{V} \int_V \boldsymbol{\sigma} \, \mathrm{d}V \ . \tag{3.16}$$

For integration over the surface S of volume V, we need to apply the Gauss divergence theorem. The Gauss divergence theorem states the relationship

$$\int_V (\sigma_{ij} x_k)_{,i} \, \mathrm{d}V = \oint_S \sigma_{ij} x_k n_i \, \mathrm{d}S \tag{3.17}$$

17

between surface and volume integrals. Here, x_k is the coordinate, and $x_{k,i}$ equals to the Kronecker delta δ_{ki}. The left hand side of the Eqn. (3.17) can be written as

$$
\begin{aligned}
\int_V (\sigma_{ij} x_k)_{,i} \, dV &= \int_V \sigma_{ij,i} x_k \, dV + \int_V \sigma_{ij} x_{k,i} \, dV \\
&= \int_V \sigma_{ij,i} x_k \, dV + \int_V \sigma_{kj} \, dV \ .
\end{aligned}
\tag{3.18}
$$

The first term on the right hand side of the above equation is zero, due to the equilibrium

$$
\sigma_{ij,i} = 0
\tag{3.19}
$$

of stresses, if the body force is zero. On the surface S of volume V, we have

$$
\sigma_{ij} n_i = \tilde{F}_j \quad \text{on } S \ .
\tag{3.20}
$$

Here, $\tilde{F}_j$ denotes the external load on surface S. Combining Eqs. (3.17), (3.18) and (3.20), we have

$$
\begin{aligned}
\overline{\sigma}_{ij} \equiv \frac{1}{V} \int_V \sigma_{ij} \, dV &= \frac{1}{V} \oint_S \sigma_{lj} x_i n_l \, dS \\
&= \frac{1}{V} \oint_S \tilde{F}_j x_i \, dS \ .
\end{aligned}
\tag{3.21}
$$

In this way, the macroscopic average stress $\overline{\sigma}_{ij}$ has been related to the external forces $\tilde{F}_j$ distributing on the surface S of the considered body.

3.2.2 Average stress in the discrete element method

A pair of contacting spherical particles, namely, the I-th and J-th particles, subject to discrete element analysis is illustrated in Figure 3.2. To describe the coordinate of the contact point, it can be either denoted as $\overline{\mathbf{x}}^{(I)}$ in the local coordinate with respect to the origin $\overline{O}^{(I)}$, or as $\mathbf{x}$ in the global coordinate system with the origin O. In the following, these two approaches are discussed. All contacts are assumed to be point-wise, and thus for particle I,

$$
\oint_S \tilde{F}_j x_i \, dS = \sum_J F_j^{(I,J)} x_i^{(J)} \ .
\tag{3.22}
$$

Here, $x_i^{(J)}$ denotes the position of the contact point with particle J.

Local coordinates

It is convenient to place the origin $\overline{O}^{(I)}$ of the I-th particle coordinate system in the center of the sphere, and the local coordinate system is named as $\overline{\mathbf{x}}^{(I)}$. In this pair of contacting particles, the relations

$$
\begin{aligned}
F_j^{(I,J)} &= f_N^{(I,J)} n_j + f_T^{(I,J)} t_j \\
F_j^{(I,J)} &= -F_j^{(J,I)} \\
\overline{x}_i^{(I,J)} - \overline{x}_i^{(J,I)} &= \delta^{(I,J)} n_i
\end{aligned}
\tag{3.23}
$$
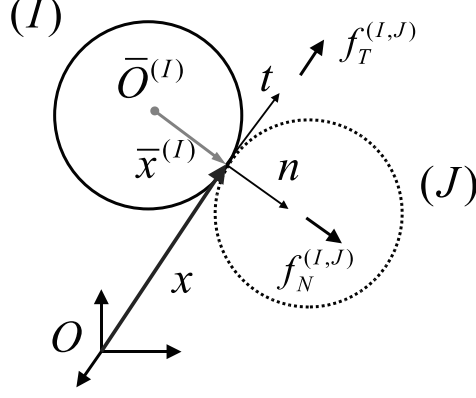
Figure 3.2: Two contacting particles.

are valid. Here, $f_N^{(I,J)}$ and $f_T^{(I,J)}$ are the magnitudes of the normal and tangential forces applied from particle J on I, $\delta^{(I,J)}$ denotes the distance between the centers of particles, and the unit vectors $\mathbf{n}$ and $\mathbf{t}$ are the normal and tangential unit vectors, respectively. The coordinate $\overline{x}_i^{(I,J)}$ describes the position of the J-th contact point in the local coordinate on particle I. The signs of the forces are defined by the vectors, i.e. a compressive force is negative. Since there is no stress present in the matrix (void), the integral of the assembly volume V can be obtained by summing each particle's volume $V^{(I)}$ $(1 \leq I \leq N)$ in the assembly. Eqn. (3.21) can be written for the N-particle assembly by summing up all the existing contact pairs

$$
\begin{aligned}
\int_V \sigma_{ij}\,\mathrm{d}V &= \sum_{I=1}^{N} \int_{V^{(I)}} \sigma_{ij}\,\mathrm{d}V \\
&= \sum_{I=1}^{N} \oint_{S^{(I)}} \tilde{F}_j \overline{x}_i^{(I)}\,\mathrm{d}S \\
&= \sum_{I=1}^{N} \sum_{J} F_j^{(I,J)} \overline{x}_i^{(I,J)} \ .
\end{aligned}
\tag{3.24}
$$

With Eqs. (3.23) and (3.24), the average stress can obtained as

$$
\begin{aligned}
\overline{\boldsymbol{\sigma}} &= \frac{1}{V}\Big(\sum_{I<J} \delta^{(I,J)} f_N^{(I,J)} \mathbf{n}\otimes\mathbf{n} + \sum_{I<J} \delta^{(I,J)} f_T^{(I,J)} \mathbf{n}\otimes\mathbf{t} \Big) \ , \\
\text{or} \quad \overline{\sigma}_{ij} &= \frac{1}{V}\Big(\sum_{I<J} \delta^{(I,J)} f_N^{(I,J)} n_i n_j + \sum_{I<J} \delta^{(I,J)} f_T^{(I,J)} n_i t_j \Big) \ .
\end{aligned}
\tag{3.25}
$$

This equation is consistent with the derivation by Christoffersen et al. (1981), and it has been implemented in DEM calculation in literature (e.g., Thornton and Antony, 1998; Martin et al., 2003; Martin, 2004; Gilabert et al., 2007, etc.).

Global coordinates

For the global coordinate system, a simulation box has been sketched in Figure 3.3. The contact forces in Eqn. (3.21), of two contacting particles inside the simulation box, are opposite while the position $\mathbf{x}$-s are identical. Therefore, the summation over all interactions between particles

inside the simulation box is zero. Only the terms stemming from contacts across the boundaries are non-zero. Considering two types of boundary conditions, we have:

- Generalized boundary conditions

$$\overline{\sigma}_{ij} = \frac{1}{V} \sum_{I} \sum_{BC} F_j^{(I,BC)} x_i \tag{3.26}$$

- Periodic boundary conditions

$$\overline{\sigma}_{ij} = \frac{1}{V} \sum_{I<J} F_j^{(I,J),BC} \tilde{L}_i^{(J)} \tag{3.27}$$

In the first case, the interaction $\mathbf{F}^{(I,BC)}$ denotes the interactions between the I-th particle and objects outside the box (e.g., the wall condition). In the second case of periodic boundary conditions, two contacts exist on the corresponding boundaries of the box, as shown in Figure 3.3. The J-th particle has been shifted by the vector $\tilde{\mathbf{L}}^{(J)}$, in order to satisfy the periodic boundary conditions, and as a result, it contacts with I-th particle inside the box. By summing up the corresponding interactions, the second expression can be obtained.
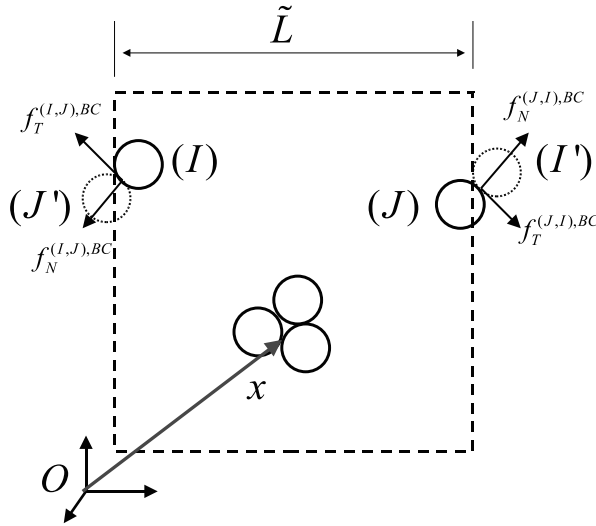
Figure 3.3: Average stress using the global coordinate.

Discussion on the averaging methods

Being independent of observers, the stress tensors obtained from both coordinates systems have to be identical. This can be proven from the DEM calculation, by implementing both methods and comparing to each other. There are some differences between these two methods:

- The first method, using the local coordinate, can be employed to calculate the local stresses inside the simulation box, for instance, the stress state of a small assembly of particles.

- The latter method, using global coordinates, can be also applied for systems of non-spherical particles. In this case, the first method is no longer valid, since Eqn. (3.23) is not fulfilled.

- The latter method is more cost-efficient for larger system, since only the summation over particles on the boundaries is taken into consideration. The difference is ignorable in the calculation of systems of a limited number of particles.

- Both methods are obtained for the assumption of zero body force, as well as the term of the acceleration $\rho \ddot{\mathbf{x}}$. Therefore, during the DEM calculation, an additional criterion has to be adopted to ensure a quasi-static state, and to obtain the exact macro-stresses from the current assembly. The real quasi-static state has not been reached until the difference

$$\left| \frac{\sigma_{ii}^{(\text{ext})} - \sigma_{ii}^{(\text{int})}}{\sigma_{ii}^{(\text{int})}} \right| < \varsigma$$

is smaller than a certain value. Here, the subscripts (ext) and (int) indicate the global and local methods, respectively, and ς is a tolerance.

- If only normal contact is considered, Eqn. (3.25) ensures the symmetry of the stress tensor. On the contrary, Eqn. (3.27) would provide a slightly asymmetric tensor during the calculation. In strain-controlled tri-axial compression, the shear stresses are not exactly zero, but a few magnitudes smaller than the normal stresses. This is caused by a slightly anisotropic packing state, which will be ignorable by using systems of a larger number of particles.

3.3 Solution techniques

In this section, we discuss some techniques used in the current discrete element study. Periodic boundary conditions (PBCs) for the simulation box, as well as the strain- and stress-controlled mechanical loading, has been implemented. The convergence condition and the damping methods to accelerate the convergence rate are also discussed.

3.3.1 Periodic boundary conditions

The initial periodic configuration is formed by shifting the particles in the objective zone, a representative volume element (RVE), by a vector $\mathbf{L}^{(n)}$ to the (n)-th periodic zone, where $n = 1...26$ in three dimensional cases. After an infinitesimal deformation, the RVE has an overall strain tensor $\boldsymbol{\varepsilon}$, and the change of $\mathbf{L}^{(n)}$ can be represented by the strain tensor. Here, the vector $\mathbf{L}^{(n)}$ changes to vector $\tilde{\mathbf{L}}^{(n)}$ with respect to the micropolar strain tensor $\boldsymbol{\epsilon}$ and microrotation tensor $\boldsymbol{\phi}$ as

$$\tilde{\mathbf{L}}^{(n)} = (\mathbf{I} + \boldsymbol{\epsilon} - \boldsymbol{\phi})^{\text{T}} \cdot \mathbf{L}^{(n)}$$
$$\text{or} \quad \tilde{L}_j^{(n)} = (\delta_{ij} + \epsilon_{ij} - \phi_{ij}) L_i^{(n)} \ .$$

(3.28)

Here, $\mathbf{I}$ is the second order identity matrix and δ_{ij} is the Kronecker delta. The definitions of the micropolar strain tensor $\boldsymbol{\epsilon}$ and microrotation tensor $\boldsymbol{\phi}$ are referred to Eringen (1968), and can be related to the overall strain tensor $\boldsymbol{\varepsilon}$ without much effort. The micropolar strain tensor $\boldsymbol{\epsilon}$ and Eulerian strain tensor $\boldsymbol{\varepsilon}$ are defined as

$$\epsilon_{ij} \equiv \phi_{ij} + u_{j,i} \ ,$$
$$\varepsilon_{ij} \equiv \frac{1}{2}(u_{i,j} + u_{j,i}) \ .$$

(3.29)

Here, u_i is the displacement vector. The micropolar strain tensor ϵ is a nonsymmetric tensor due to the presence of microrotation tensor ϕ. In this work, the microrotations (ϕ_{ij}) and rigid body rotations ($\frac{1}{2}\epsilon_{ijk}u_{k,j}$) are constrained and hence equal to zero with respect to time. Therefore, Eqn. (3.28) can be reduced to $\tilde{L}_j^{(n)} = (\delta_{ij} + \varepsilon_{ij})L_i^{(n)}$. Figure 3.4 shows the vector $\tilde{\mathbf{L}}^{(n)}$ varies with respect to the strain tensor ε, where (a) is the initial configuration and (b) indicates an infinitesimally deformed shape.
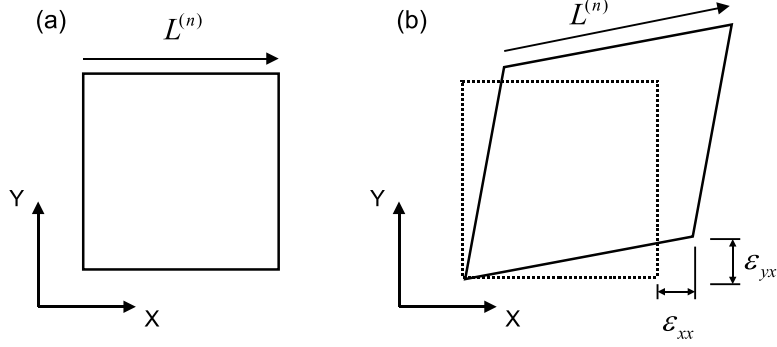
Figure 3.4: A schematic drawing of the vector $\tilde{\mathbf{L}}^{(n)}$.

3.3.2 Ways of mechanical loading

Changing the strain tensor, strain control of the RVE can be realized by Eqn. (3.28). In order to control the deformation of the periodic cell, an incremental strain tensor $\Delta\varepsilon_{ij}$ is specified, according to which the centers of all the particles in the assembly are initially moved by

$$\Delta x_j = \Delta\varepsilon_{ij}x_i \ , \tag{3.30}$$

at the beginning of each loading step, as if they are points in a continuum. Then the calculations to reach the equilibrium state are carried out iteratively. The applied deformations of particles in the RVE result in stresses, which can be calculated by interaction forces, see Eqn. (3.25) or Eqn. (3.27).

Moreover, to implement stress proportional loading, the stress can be controlled by a proportional-integral-derivative (PID) controller (Ziegler and Nichols, 1993). The PID controller algorithm involves three separate parameters: the proportional, integral and derivative values. The proportional value determines the reaction to the current error $e(t)$, the integral value determines the reaction based on the sum of the recent errors and the derivative one determines the reaction to the rate at which the error has been changing. The weighted sum of these three actions is used to adjust the process via a control element. The manipulated variable (MV) can be expressed as the standard form of the PID controller in devices as

$$\mathrm{MV}(t) = K_p \Big[e(t) + \frac{1}{T_i} \int_0^t e(\tau) \, \mathrm{d}\tau + T_d \frac{\mathrm{d}e(t)}{\mathrm{d}t} \Big], \tag{3.31}$$

where K_p is the proportional gain, and T_i and T_d are the integral time and derivative time, respectively.

Assuming the materials being initially isotropic, the incremental form of Hook's law can be expressed in the Cartesian coordinate system (x_1, x_2, x_3) as

$$d\varepsilon_{ij} = \frac{1}{E^*}\Big[(1+\nu)\,d\sigma_{ij} - \nu\delta_{ij}\,d\sigma_{kk}\Big]. \tag{3.32}$$

If $\bar{\sigma}_{ij}^{(n)}$ is the desired value of stress and $\sigma_{ij}^{(n)}$ is the calculated value, the strain tensor can be updated by the current error $d\sigma_{ij}^{(n)} = \bar{\sigma}_{ij}^{(n)} - \sigma_{ij}^{(n)}$ of the stress tensor and the counterpart $d\sigma_{ij}^{(n-1)}$ at the previous step , in the framework of the PID controller as

$$\begin{aligned}
d\varepsilon_{ij}^{(n)} &= d\varepsilon_{ij}^{P,(n)} + d\varepsilon_{ij}^{I,(n)} + d\varepsilon_{ij}^{D,(n)} \;, \\
\varepsilon_{ij}^{(n)} &= \varepsilon_{ij}^{(n-1)} + d\varepsilon_{ij}^{(n)} \;.
\end{aligned} \tag{3.33}$$

Here, the respective contributions of the PID parts are

$$\begin{aligned}
\mathbf{P}: \quad & d\varepsilon_{ij}^{P,(n)} = \frac{1}{E^*}\Big[(1+\nu)d\sigma_{ij}^{(n)} - \nu d\sigma_{kk}^{(n)}\delta_{ij}\Big] \\
\mathbf{I}: \quad & d\varepsilon_{ij}^{I,(n)} = d\varepsilon_{ij}^{I,(n-1)} + \frac{1}{E^*}\frac{dt}{T_i}\Big[(1+\nu)d\sigma_{ij}^{(n)} - \nu d\sigma_{kk}^{(n)}\delta_{ij}\Big] \\
\mathbf{D}: \quad & d\varepsilon_{ij}^{D,(n)} = \frac{1}{E^*}\frac{T_d}{dt}\Big[(1+\nu)(d\sigma_{ij}^{(n)} - d\sigma_{ij}^{(n-1)}) - \nu(d\sigma_{kk}^{(n)} - d\sigma_{kk}^{(n-1)})\delta_{ij}\Big].
\end{aligned} \tag{3.34}$$

Therefore, by summing up these parts, we have

$$\begin{aligned}
d\varepsilon_{ij}^{(n)} = d\varepsilon_{ij}^{I,(n-1)} &+ \frac{1+\nu}{E^*}\Big[(1+\frac{dt}{T_i})d\sigma_{ij}^{(n)} + \frac{T_d}{dt}(d\sigma_{ij}^{(n)} - d\sigma_{ij}^{(n-1)})\Big] \\
&- \frac{\nu}{E^*}\delta_{ij}\Big[(1+\frac{dt}{T_i})d\sigma_{kk}^{(n)} + \frac{T_d}{dt}(d\sigma_{kk}^{(n)} - d\sigma_{kk}^{(n-1)})\Big].
\end{aligned} \tag{3.35}$$

The value of E^* and ν can be set rather arbitrarily, and they are not necessarily equal to the ones of the assembly. If we only consider the integral part of the PID controller, as $d\varepsilon_{ij}^{(n)} = d\varepsilon_{ij}^{I,(n)}$, and set $\nu = 0$, we have the form of

$$\dot{\varepsilon}_{ij}^{(n)} = \dot{\varepsilon}_{ij}^{(n-1)} + \frac{1}{E^*T_i}d\sigma_{ij}^{(n)} \;. \tag{3.36}$$

The general form in Eqn. (3.35) has been reduced to the servo-control of strain rate used in literature (Thornton and Antony, 1998; Antony, 2000).

Since the particle assembly has a random structure (slight anisotropy), a small shear strain/stress is present, if the principle stresses/strains are applied on the assembly. Two strategies can be used to eliminate either shear stresses or shear strains: (1) let $\varepsilon_{ij} = 0$ for $i \neq j$, and accept shear stresses to be present; or (2) let $\sigma_{ij} = 0$ for $i \neq j$, and accept shear strains to be present.

3.3.3 Convergence control

The most simple example for the determination whether a system reaches the equilibrium state is a single spring-mass system. In terms of energy, all systems have two types of energy, potential energy and kinetic energy. When a spring is stretched or compressed, it stores elastic potential energy, which may then transfer into kinetic energy. If the system is a dissipative one (e.g., a

spring-dashpot-mass system), the total energy will finally be transformed into heat. The steady-state can be reached eventually (as $t \to \infty$) by not only minimizing potential energy (min $\mathcal{V}$) but also removing all kinetic energy ($\mathcal{K} = 0$).

In an assembly, the network of contacts can also be simplified into spring-dashpot-mass systems. Thus, to achieve convergence in such a simple system, the criterion of unbalanced force is not sufficient for equilibrium. Additionally, the criterion of the kinetic energy should be taken into account. The principle stays unchanged for the whole assembly. The velocity (kinetic energy) and acceleration, representing the unbalanced force, of particles should be checked at the same time. The criteria can be expressed as

$$\delta f \le \delta f_0, \quad \bar{\mathcal{K}} \le \mathcal{K}_0. \tag{3.37}$$

Here, δf_0 and K_0 are two inputs for the convergence criteria, namely, maximum allowable unbalanced force and maximum allowable average kinetic energy, respectively.

For force convergence (unit: N), we have

$$\delta f_0 \le \max(\delta f_{\min}, \alpha_0 \cdot f_{\text{ave}}) , \tag{3.38}$$

where f_{ave} is the average contact force in the assembly, and the tolerance for the unbalanced force $\delta f_{\min}$ and the ratio to the average contact force α_0 are constants. The average kinematic energy (unit: J) of the assembly is given by

$$\bar{\mathcal{K}} = \frac{1}{N} \sum_{I=1}^{N} \left[\frac{1}{2} m^{(I)} (\mathbf{v}^{(I)})^2 + \frac{1}{2} I^{(I)} (\boldsymbol{\omega}^{(I)})^2 \right] . \tag{3.39}$$

In this investigation, we assume that the equilibrium state of the assembly is not reached, until Eqn. (3.37) is satisfied.

3.3.4 Damping method

In order to remove the kinetic energy and to achieve convergence inside the assembly, a dissipation mechanism should be introduced. This is divided into two parts: local damping and global damping.

For the I-th and J-th particles in contact, if only the dependence on the relative normal velocity $\dot{\mathbf{x}}_N^{(I,J)}$ is taken into account, the local damping force is given by

$$\mathbf{f}_d^{(I)} = -m_{\text{eff}} \eta_d \dot{\mathbf{x}}_N^{(I,J)}. \tag{3.40}$$

Here, $m_{\text{eff}} = m^{(I)} m^{(J)} / (m^{(I)} + m^{(J)})$ is the reduced mass. The local damping factor η_d can be found for different materials in Kruggel-Emden et al. (2007). The local damping forces will vanish when relative velocities $\dot{\mathbf{x}}_N^{(I,J)}$ are approaching zero.

In addition to local damping, a global damping mechanism is introduced to speed up convergence. For the I-th particle, the global damping force is

$$\begin{aligned}
\mathbf{f}_D^{(I)} &= -m^{(I)} \eta_D \dot{\mathbf{x}}^{(I)}, \\
\mathbf{\Gamma}_D^{(I)} &= -I^{(I)} \eta_D \boldsymbol{\omega}^{(I)}.
\end{aligned} \tag{3.41}$$

Here, η_D is the global damping factor. Similar to the local damping mechanism, global damping forces will vanish when velocities $\dot{\mathbf{x}}^{(I)}$ and $\boldsymbol{\omega}^{(I)}$ are approaching zero. For a quasi-static analysis, global damping can be used to absorb the kinetic energy, and hasten to reach the equilibrium for the assembly.

3.4 Initial packing

From a microscopic point of view, the configuration of particles inside an assembly plays a major role in their overall constitutive behaviour, and different packing factors introduce a different mechanical response to the external excitation. This parameter is important in fusion blankets, due to the fact that the pebble beds expand during the increase of temperature, and hence the induced stresses affect the coupled thermo-mechanical properties. It is obvious that the thermal stresses will vary according to initial packing factor at the same temperature level. On the contrary, a low packing factor will provide a low effective thermal conductivity for the assembly, which might be insufficient to conduct the heat generated in the pebble bed.

For pebble beds in fusion blankets, the packing factor is in the range of 63%-64% (Reimann et al., 2005a). In this section, we focus on the algorithm for initial packing, since it is crucial to prepare an initial state of the assembly with both reasonable packing factor and topology before the discrete element simulation itself.

The ordered close packing of hard mono-sized spheres has a maximum packing factor of $\eta = \pi/(18)^{1/2} \cong 0.7405$, when the spheres are packed in either the face-centered cubic (FCC) or the hexagonal close-packed (HCP) structure. On the other hand, the packing factor η for experimental packing of mono-sized spheres varies with the method of packing. Berryman (1983) noted that the experimentally obtainable values of random close packing are in the range of 0.64 ± 0.02. The computer simulation of random close packing has been studied by various researches (Berryman, 1983; Jodrey and Tory, 1985; Zinchenko, 1994; Torquato et al., 2000; Wouterse and Philipse, 2006). Several algorithms have been proposed to get more realistic initial configurations, among which the one suggested by Jodrey and Tory (1985) has the advantage to control the final packing factor by a parameter, called the contraction rate κ. In this section, this algorithm will be introduced and then extended to polydisperse spherical packing.

3.4.1 Random close packing algorithm

Jodrey and Tory (1985) have proposed an algorithm to obtain random close packing of equal-sized spheres by both removing the overlaps and reducing the radius of particles iteratively. First, N spherical particles are generated randomly into a $L \times L \times L$ cube. Initially, the so-called outer radius (r_{out}) of an assembly of N equal-sized particles is set to make the packing factor equal to 1.0. Meanwhile, a so-called inner radius (r_{in}) is set to be half of the distance between the two closest particles' centers. That means if all particles had a radius of r_{in}, there would be no overlap between particles inside the whole assembly. The definitions of the outer and inner radii are schematically shown in Figure 3.5 for the simplest case of two overlapping particles. Each iteration has two functions: first, the worst overlap is removed by moving the two particles away from each other by an equal distance of $r_{out} - r_{in}$, along the line connecting

the two centers; second, the outer radius is contracted according to

$$\chi^{(i+1)} = \chi^{(i)} - (\frac{1}{2})^j \kappa/N \; , \tag{3.42}$$

where

$$\chi^{(i)} = \frac{r_{out}^{(i)}}{r_{out}^{(0)}} \; ,$$

and

$$j = \lceil -\log_{10} \Delta \eta^{(i)} \rceil \; .$$

Here, i denotes the number of iterations, N is the number of particles (e.g., $N = 5000$ in this investigation), $\Delta \eta$ is the difference between the packing factors calculated by the outer and inner radii (r_{out} and r_{in}), namely, the nominal packing factor η^{nomi} and the true packing factor η^{true}, respectively. The operator $\lceil \bullet \rceil$ is the greatest integer function. The parameter κ, which is independent of the size and number of the spheres, characterizes the contraction rate of the assembly.
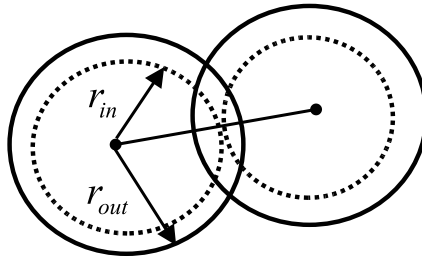

Figure 3.5: The definition of r_{out} and r_{in} in a two-particle system.

The final configuration is reached, if the condition $r_{out} \leq r_{in}$ is satisfied. In a N-particle assembly, the parameter κ is the only one to control the contraction rate, and hence different packing factors can be reached by changing κ. In the work of Jodrey and Tory (1985), they established a relation between the obtaining packing factor and the contraction rate κ, for assemblies composed of 1000 equal-sized spherical particles with PBCs, despite their different initial configurations generated randomly. Figure 3.6 shown a typical evolution of η^{nomi} and η^{true} over the iterations. The assembly contains 5000 equal sized spherical particles and $\kappa = 2 \times 10^{-5}$. The nominal density decreases from its initial value of 1.0 to its final value of 0.6436, while the true density, calculated by the inner radius, increases.

This algorithm was originally based on the idea of concurrently removing the worst overlap and reducing the outer radius, and it can be extended easily to solve the initial packing problem of polydisperse (multi-sized) particles. To make use of this algorithm in an assembly of polydisperse particles, the outer radius r_{out} and inner radius r_{in} should be redefined. These radii depend on the size distribution of particles in the assembly. Based on these radii, the method can be specified. Contrary to the mono-sized packing as discussed above, the outer radius and inner radius of each particle may not be identical to the ones of other particles for polydisperse packing.

It is assumed that the distribution of the radii obeys some function $f(I)$ where $1 \leq I \leq N$ (e.g., $f(I) \equiv 1$ for mono-sized particles). In an assembly of different sized particles, the radius of each individual particle (e.g., the I-th particle) in the current step, called the outer radius $r_{out}^{(I)}$, can
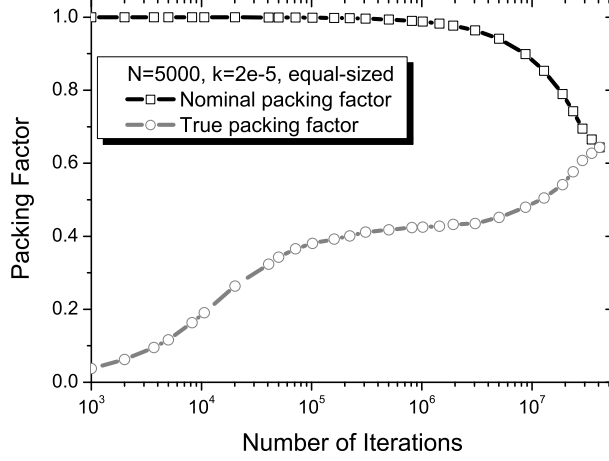
Figure 3.6: The evolution of the nominal and true packing factors over the number of iterations.

be written as

$$r_{out}^{(I)} = f(I) \cdot \tilde{r}_{out} \; . \tag{3.43}$$

Here, $\tilde{r}_{out}$ is an outer scaling radius of the assembly. According to $\tilde{r}_{out}$, a nominal packing factor can be calculated as if the particles have radii of $r_{out}^{(I)}$ $(I = 1, 2, ..., N)$

$$\eta^{nomi} = \frac{4}{3}\pi\tilde{r}_{out}^3 \cdot \sum_{I=1}^{N} [f(I)]^3 / L^3 \; . \tag{3.44}$$

The value of $\tilde{r}_{out}$ is initially set to yield the nominal packing factor $\eta^{nomi} = 100\%$, irrespective of the existence of overlaps in the assembly.

For each particle, the corresponding inner radius is

$$r_{in}^{(I)} = f(I) \cdot \tilde{r}_{in} \; . \tag{3.45}$$

The inner scaling radius $\tilde{r}_{in}$ is chosen in such way that there is no overlap in the assembly. If the distance between two particles I and J is $\delta^{(I,J)}$, then the inner radius of the assembly is defined as

$$\tilde{r}_{in} \equiv \min_{I<J} \left[\frac{\delta^{(I,J)}}{f(I) + f(J)} \right] \; . \tag{3.46}$$

The value of $\tilde{r}_{in}$ is determined by searching all overlaps in the target domain, as Eqn. (3.46). This pair of these particles (for instance, the I-th and J-th particles) is defined as the worst overlap for polydisperse packing. This can be reduced to the equal-sized packing, if $f(I) \equiv 1$. But with the size distribution $f(I) \neq 1$, the worst overlap might not equal to the absolute minimum distance, due to the presence of different-sized particles. Using the inner radius $\tilde{r}_{in}$, another packing factor, called true packing factor, can be obtained:

$$\eta^{true} = \frac{4}{3}\pi\tilde{r}_{in}^3 \cdot \sum_{I=1}^{N} [f(I)]^3 / L^3 \; . \tag{3.47}$$

27

Substitute $\tilde{r}_{out}$ and $\tilde{r}_{in}$ into Eqs. (3.43) and (3.45), we have the maximum overlap as $\Delta = r_{out}^{(I)} + r_{out}^{(J)} - \delta^{(I,J)}$. To remove this overlap, several different laws can be applied. The general expression of the movement of the I-th particle can be written as

$$d^{(I)} = \Delta \frac{[f(J)]^n}{[f(I)]^n + [f(J)]^n} \ . \tag{3.48}$$

Here n can be set to 0, 1, 2 and 3, for equal/linear/square/cubic interpolation, respectively. The equal interpolation means that there is no weight function applied to the movements of the different-sized particles; the cubic interpolation means that the weight function is verse proportional to the mass of the spherical particles, if they have the same density of the bulk material; n equaling to 1 or 2 is something in between. In this investigation, $n = 1$ is used for the sake of simplicity.

According to $\tilde{r}_{in}$ and $\tilde{r}_{out}$, the worst overlap is removed and the outer radii of particles, i.e. $r_{out}^{(I)}$ ($I = 1, 2, ..., N$), are contracted iteratively for polydisperse packing. For each iteration, the nominal and true packing factors are calculated by Eqs. (3.44) and (3.47), and the inner radius $\tilde{r}_{in}$ is calculated from the worst overlap by Eqn. (3.46). The worst overlap Δ is removed, the consequence of which is to increase the inner radius $\tilde{r}_{in}$. And then the outer radius $\tilde{r}_{out}$ of the particle assembly is reduced by Eqn. (3.42), while the distribution function $f(I)$ keeps unchanged. The iteration will stop and the assembly reaches the finial packing factor, if the difference between $\tilde{r}_{in}$ and $\tilde{r}_{out}$ is smaller than the tolerance. The evolution of the nominal packing factor η^{nomi} and the true packing factor η^{true} is similar to mono-sized packing, as Figure 3.6.

For polydisperse packing, the radii distribution function $f(I)$ can be varied by several parameters. For instance, a uniform distribution, a normal distribution, etc. can be applied to describe different types of polydisperse packing. The simplest case in polydisperse packing will be the packing of binary mixtures, next to the equal sized packing (Cumberland and Crawford, 1987). The sizes of pebbles vary also in HCPB blankets. For the reference Li_4SiO_4 pebbles, the diameter lies in the range of 0.25-0.63 mm (Loebbecke and Knitter, 2007).

3.4.2 Packing factors of mono-sized particles

Assemblies with 5000 equal-sized spherical particles have been generated by the random packing algorithm with periodic boundary conditions. The contraction rate κ varies from 1×10^{-5} to 1×10^{-3}. For each given contraction rate, a few samples have been generated independently. Figure 3.7 shows that we can produce randomly packed assemblies for which $0.625 \leq \eta \leq 0.645$. The packing factor can be controlled roughly by the value of the given contraction rate κ. For the same contraction rate, differences between samples are relatively small. The fitting curve for $N = 1000$ assemblies from Jodrey and Tory (1985), although they focused on the region of the dense close packing, is plotted as dashed line for comparison.

3.4.3 Packing factors of binary mixtures

One way to increase the packing factor is to fill the space with smaller spheres, i.e. to use a binary mixture. There are two parameters to describe the size distribution of particles: the size
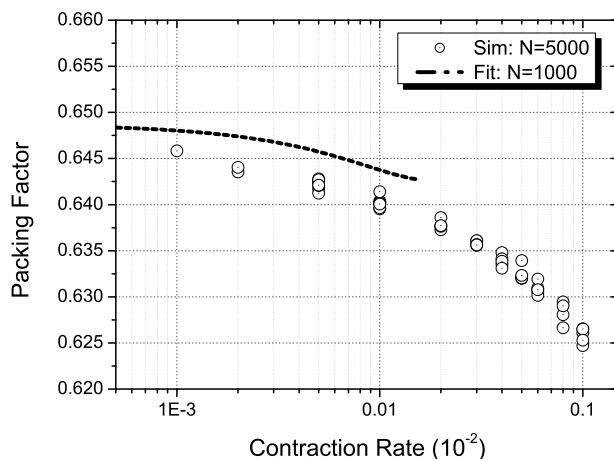
Figure 3.7: Variation of packing factor η with the contraction rate κ, $N = 5000$. The dashed line shows the fit for assemblies with 1000 equal-sized particles (Jodrey and Tory, 1985).

ratio of large and small particles, r_L/r_S, and the volume fraction of each group of particles, ϕ_L and ϕ_S, where $\phi_L + \phi_S = 1.0$. The relative size and the population of large particle can fully describe the size distribution of the assembly. By varying these two parameters, the packing factor will be changed, and it is interesting to find out the maximum packing factor among different types of binary mixtures. However, large r_L/r_S may introduce size segregation under vibration inside the assembly, and a critical value of $r_L/r_S = 2.78$ has been suggested (Duran et al., 1993, 1994).

First the contraction rate is fixed as $\kappa = 1 \times 10^{-4}$ in this investigation. The changing of the packing factor depending on r_L/r_S and ϕ_L can be found in Figure 3.8. Sets of calculations with different size ratios (5/3, 3 and 7) are carried out, and for each data point, 5 samples are made for statistical purposes. For larger size ratios, a higher packing factor η can be obtained for the same volume fraction ϕ_L, while for the same size ratio, the maximum value is reached in the range of volume fraction between 0.7 and 0.8. In literature, the theoretical value of $\phi_L = 0.735$ for the highest packing factor has been suggested (Cumberland and Crawford, 1987). Two obtained assemblies are visualized in Figure 3.9: (a) $r_L/r_S = 5/3$ and $\phi_L = 0.7$, with a packing factor of $\eta = 0.6606$; (b) $r_L/r_S = 3.0$ and $\phi_L = 0.7$, with $\eta = 0.7123$.

3.5   Simulation of uniaxial compression tests

In this section, simulations of uniaxial compression tests on assemblies of Li_4SiO_4 pebbles are carried out using the discrete element method. In this work, we consider "soft" compaction, meaning, compaction without sintering and crushing.

The loading conditions of the assembly are defined by the macro-strain tensor: ε_{33} increases from 0 to 1.25% and the other components are zero. Periodic boundary conditions for the assembly are implemented by Eqn. (3.28) with respect to the current configuration, and the overall stress tensor is calculated by Eqn. (3.25).
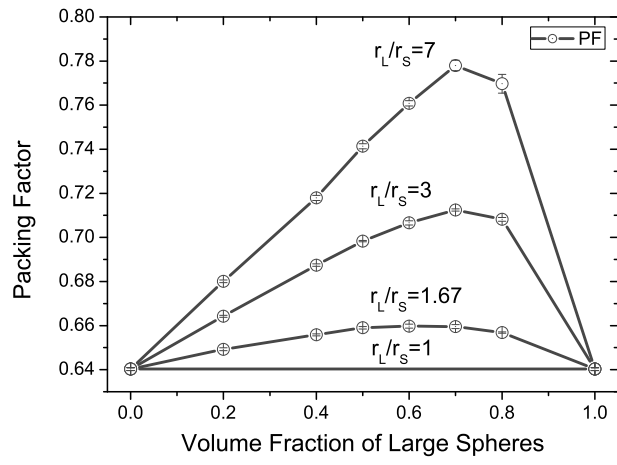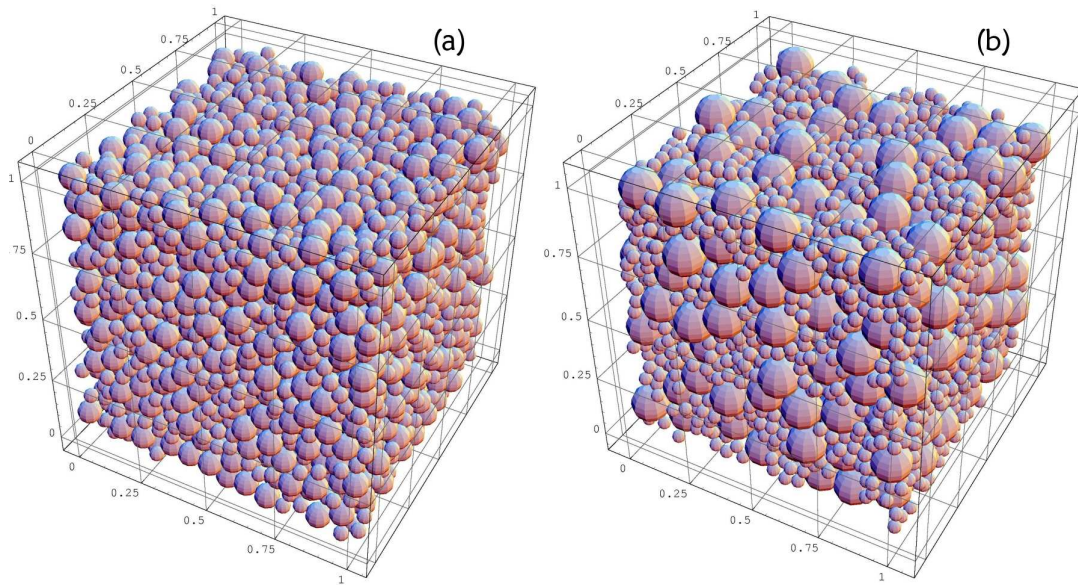
Figure 3.8: Packing factors of binary mixtures.

Figure 3.9: Visualization of binary mixtures: (a) $r_L/r_S = 5/3$ and $\phi_L = 0.7$; (b) $r_L/r_S = 3.0$ and $\phi_L = 0.7$.

3.5.1 Material parameters

Young's modulus for bulk Li$_4$SiO$_4$ has been measured by Dienst and Zimmermann (1988) and Zimmermann (1989), and it depends on both porosity of the material and temperature. The relation is expressed as follow

$$E = 110(1 - \tilde{p})^3 \times [1 - 2.5 \times 10^{-4}(T - 293)] \quad (GPa) . \qquad (3.49)$$

Here, $\tilde{p}$ is the porosity of the bulk material and T is the temperature in Kelvin. For Li$_4$SiO$_4$ pebbles, $\tilde{p} = 5 \sim 6\%$ (Knitter and Alm, 2005; Knitter et al., 2007), and the temperature is around 20 ^oC. Therefore, we set the material parameters as $E = 90$ GPa and $\nu = 0.24$. Only elastic contact is taken into account in this simulation, which seems to be justified, since the bulk material is Li$_4$SiO$_4$ ceramic in this study, whose plastic deformation is negligible. The normal interaction is described as Eqn. (3.12), and the elastic potential energy for each contact is $\phi^{(I,J)} = \frac{8}{15}E^*\sqrt{R^*}\delta^{5/2}$. The density of the bulk material is 2260 kg/m^3 (Loebbecke and Knitter, 2007). For tangential interactions, the friction coefficient is set to 0.1 due to lack of experimental data. A low friction coefficient increases potential particle movement and reduces overall loads, and vice versa (Procopio and Zavaliangos, 2005).

The parameters for the convergence control introduced in Section 3.3 can be found in Table 3.1, namely, the tolerance for unbalanced force $\delta f_{\min}$ and the ratio to the average contact force α_0, the maximum allowable average kinetic energy $\mathcal{K}_0$, the local damping factor η_d, and the global damping factor η_D. The tolerance $\delta f_{\min} = 5 \times 10^{-4}N$ will introduce an error of a few kPa to the stress tensor, while the damping factors result in dissipation forces with a magnitude of less than $1 \times 10^{-4}N$ after convergence is reached. These settings are comparably strict, and thus errors should be negligible.

Mono-sized pebbles are generated in the range of packing factors from 63.3% to 64.4%, and the diameter of pebbles is set to 0.5 mm. The samples are divided into three groups of packing factors: Low) 63.3-63.5 %, Medium) 63.7-63.9% and High) 64.0-64.4%, as listed in Table 3.2. The number of particles in this simulation is 5000. Since periodic boundary conditions are applied, the number of particles seems to be sufficient to give a representative result (Gusev, 1997, 2007).

Table 3.1: Parameters for the convergence control

$\delta f_{\min}$ (N)	α_0 (1)	$\mathcal{K}_0$ (J)	η_d (1/s)	η_D (1/s)
5×10^{-4}	5×10^{-4}	1×10^{-12}	5×10^4	5×10^4

Table 3.2: Packing factors of the samples

Number	L: 63.3-63.5 %	M: 63.7-63.9%	H: 64.0-64.4%
1	0.63393841	0.63728178	0.64007780
2	0.63411831	0.63772953	0.64166147
3	0.63479272	0.63859036	0.64355432

3.5.2 Stress-strain curves

The macro-strain $\varepsilon_{33} = -1.25\%$ is applied incrementally to the assemblies, and the stress σ_{33} is calculated by the interaction forces. After loading, the assemblies are unloaded by gradually removing ε_{33} until the stress σ_{33} reaches zero. Figure 3.10 shows the stress-strain curves from discrete element simulations of assemblies with (a) low, (b) medium and (c) high initial packing factors, and a typical experimental curve (Reimann et al., 2005a) is plotted as the dashed line for comparison.

The loose-packed assemblies deform significantly up to $\varepsilon_{33} = -0.4\%$ for small compressive stresses. Then stresses are gradually built up, see Figure 3.10-(a). This suggests that for a loose-packed assembly applying small compressive stresses (i.e. a few kPa) can increase the packing factor without introducing notable residual stresses inside the assembly. The response of those assemblies is more compliant than the experimental curve. The consistency of the unloading path of the experimental curve can be also found in the simulation, although shifts about $\Delta\varepsilon_{33} = 0.5\%$ are found in those assemblies. This indicates that the elastic constants, e.g., Young's modulus, of the assembly depend on the stress state rather than on compressive strains. Friction forces (Makse et al., 2000) and rolling resistance (Oda and Iwashita, 2000; Gilabert et al., 2007) can form a jammed system and hence lead to a build-up of stresses inside the assembly (Goldenberg and Goldhirsch, 2005; Richard et al., 2005). However, in this study the friction coefficient is set to a comparably low value of 0.1 and no rolling resistance has been taken into account with the goal of making a first step towards the simulation of pebble beds. Assemblies with medium packing factors agree satisfactorily with the experimental curve, see Figure 3.10-(b). The maximum compressive stresses reached at end of loading are comparable to the experiment. The unloading path shows the similar trend parallel to the experiment, and, furthermore, gives a macroscopic irreversible strain at the end of unloading, which can be compared quantitatively to the experimental curve. The close-packed assemblies, in Figure 3.10-(c), show a much stiffer response than the experiment. Relatively small irreversible strains can be found. Such assemblies can represent the behaviour of densified pebble beds after a few cyclic compressive loadings. For the extreme case of $\eta = 64.36\%$, the compressive stress reaches almost 8 MPa at the end of loading.

In summary, the stress-strain curves of three groups differ significantly, suggesting that the sensitivity to the packing factor is an important issue in pebble beds related problems. Overall plastic strains are observed for the assemblies, despite the fact that only elastic interactions are taken into account in this investigation. The macroscopic irreversibility found in the present discrete element simulations has to be affiliated to rearrangement of elastic particles.

3.5.3 Visualization of the assembly

With the help of OpenGL® (Angel, 1996), a visualization software has been developed to visualize outputs from the discrete element simulation.

Figure 3.11 shows the force chains and the elastic potential energy of an assembly at different loading levels. Three loading steps of the assembly M1 are chosen as shown in Figure 3.10-(b). The magnitudes of the strain ε_{33} are 0.25%, 0.75% and 1.25%. The unit of normal contact forces is N, and the unit of elastic potential energy is $10^{-6}J$. The potential energy depends on both
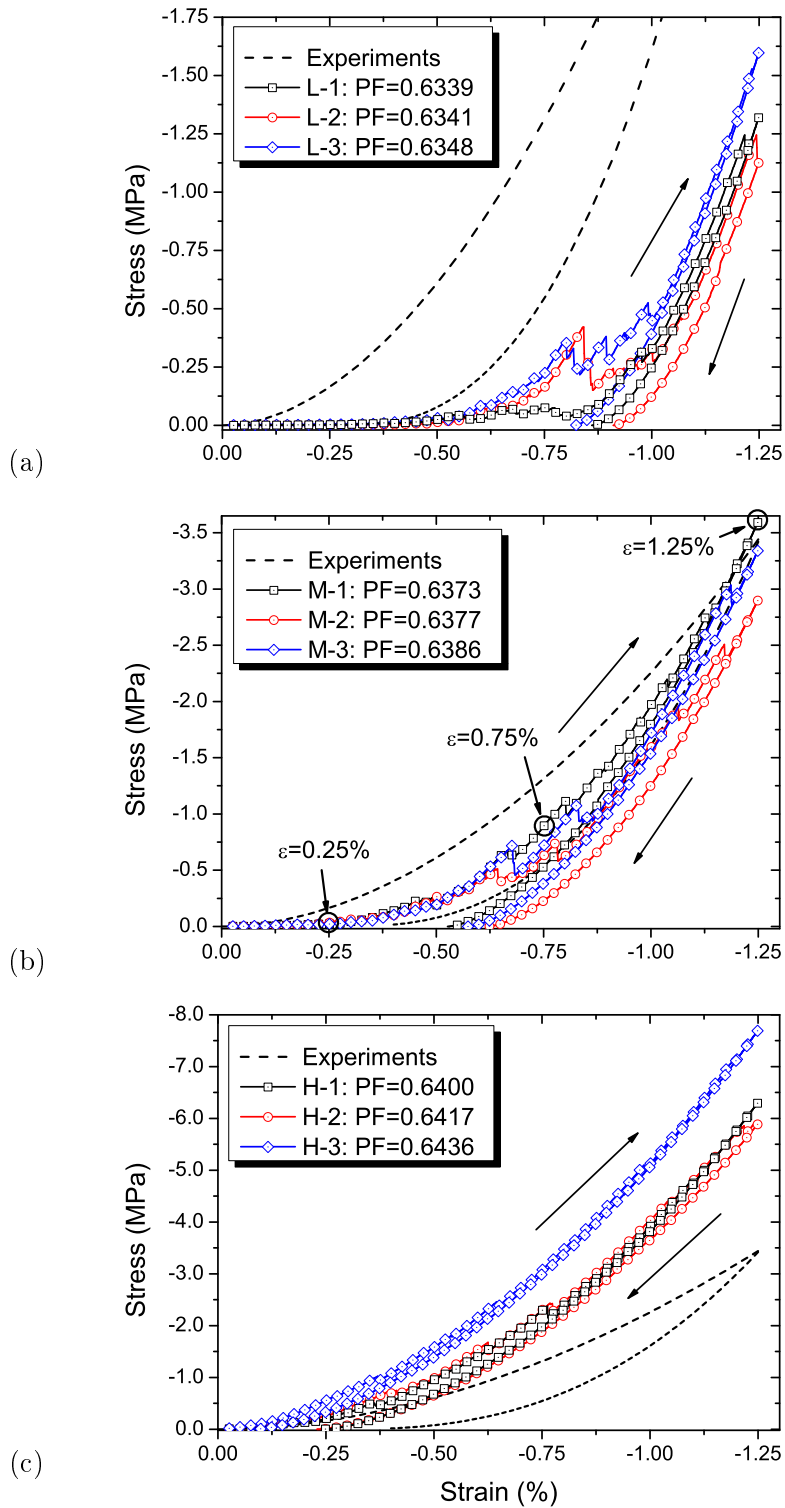
(a)

(b)

(c)

Figure 3.10: Stress-strain curves of discrete element simulations of uniaxial compression tests, assemblies with: (a) low; (b) medium ;(c) high packing factors.

magnitude and number of contact forces. According to the positions of particles at different loading levels, rearrangements can be found.

Force chains are formed at the low strain level, and evolve during loading. Main force chains are developing during loading and support the whole assembly. Non-uniform distributions of both potential energy and inter-particle forces are observed. The force chains are important for the understanding of the mechanism of heat transfer inside the assembly, especially for those materials with high ratio of solid-to-gas thermal conductivities, such as beryllium pebbles. The main force chains, carrying most of the external load, have less thermal resistance to the heat flux transferring through the assembly. Based on discrete element methods, it will be possible to formulate an anisotropic thermal conductivity taking into account the loading histories.

3.5.4 Statistical analyses

In addition to the macroscopic quantities, such as stresses and strains, the interactions can be obtained explicitly by the discrete element simulation. We focus on the probability distribution of normal contact forces, as well as mean values of coordination number and contact forces in dependence on the macroscopic stress state. Here, the coordination number is the total number of contacting neighbours of a central particle.

Figure 3.12 shows probability distributions of the normalized normal forces $f^{(I,J)}/f_{\mathrm{ave}}$ and normalized maximum normal forces $f^{(I)}_{\max}/f_{\mathrm{ave}}$ in two assemblies, namely M1 and H3. The average normal force f_{ave} is the mean value of all normal interactions inside the assembly, and the maximum normal force $f^{(I)}_{\max}$ of each particle is defined as the maximum absolute value among all the normal forces applied on this particle.

For both types of probability distributions, similarities are found not only in different loading levels, namely, 0.25%, 0.75%, 1.00% and 1.25%, but also between the two chosen assemblies. Despite the fact that at different loading levels the average normal contact force and the co-ordination number (C.N.) vary in a wide range, nearly congruent probability distributions can be found. Figure 3.12-(a) and (c) show non-uniform distributions of the normalized normal forces. A small fraction of the normal forces is in the high $f^{(I,J)}/f_{\mathrm{ave}}$ ratio region. The peak of the distribution is located in the region $f^{(I,J)}/f_{\mathrm{ave}} < 1.0$. In Figure 3.12-(b) and (d), however, the peak of the probability distribution of the normalized maximum contact force is located at $f^{(I,J)}/f_{\mathrm{ave}} \approx 1.5$, suggesting that most of particles inside the assembly have a maximum contact force larger than f_{ave}.

The change of the average coordination number, named as n_C, of an assembly over the macroscopic hydrostatic pressure, $p = -\sigma_{ii}/3$, is plotted in Figure 3.13. Assemblies with medium and high packing factors are represented, and the ones with low packing factors are excluded from the figure since their macroscopic stresses only vary in relatively small ranges. The average coordination number varies between 5.8 and 6.7, for hydrostatic pressures from 0 to 8 MPa. It rapidly increases with the increase of compressive stresses in the low stress region. New contacts are formed as a result of the compressive stress state, which in turn increases the stiffness of the assembly. Eventually the average coordination number becomes less sensitive to the increase of hydrostatic pressure, suggesting a saturation value of n_C. The distribution of the data points

0.25%

0.75%

1.25%

max 3.15

NORM FORCE

min 0.00

max 5.07

Pot ENERGY

min 0.00
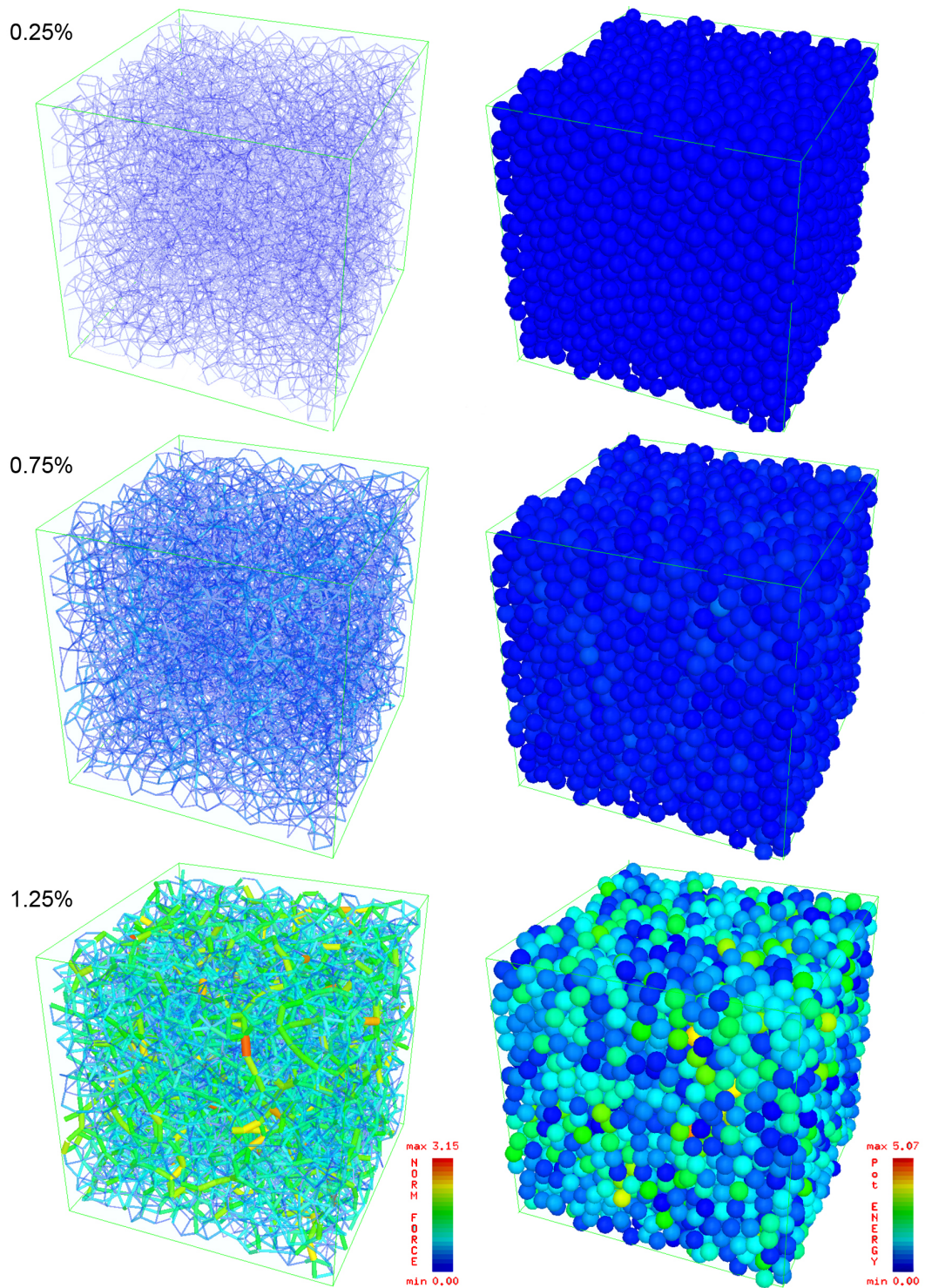
Figure 3.11: Visualization of simulation results: left, inter-particle force chains; right, elastic potential energy.

(a) M1: $P(f^{(I,J)}/f_{\mathrm{ave}})$

(b) M1: $P(f_{\max}^{(I)}/f_{\mathrm{ave}})$

(c) H3: $P(f^{(I,J)}/f_{\mathrm{ave}})$

(d) H3: $P(f_{\max}^{(I)}/f_{\mathrm{ave}})$
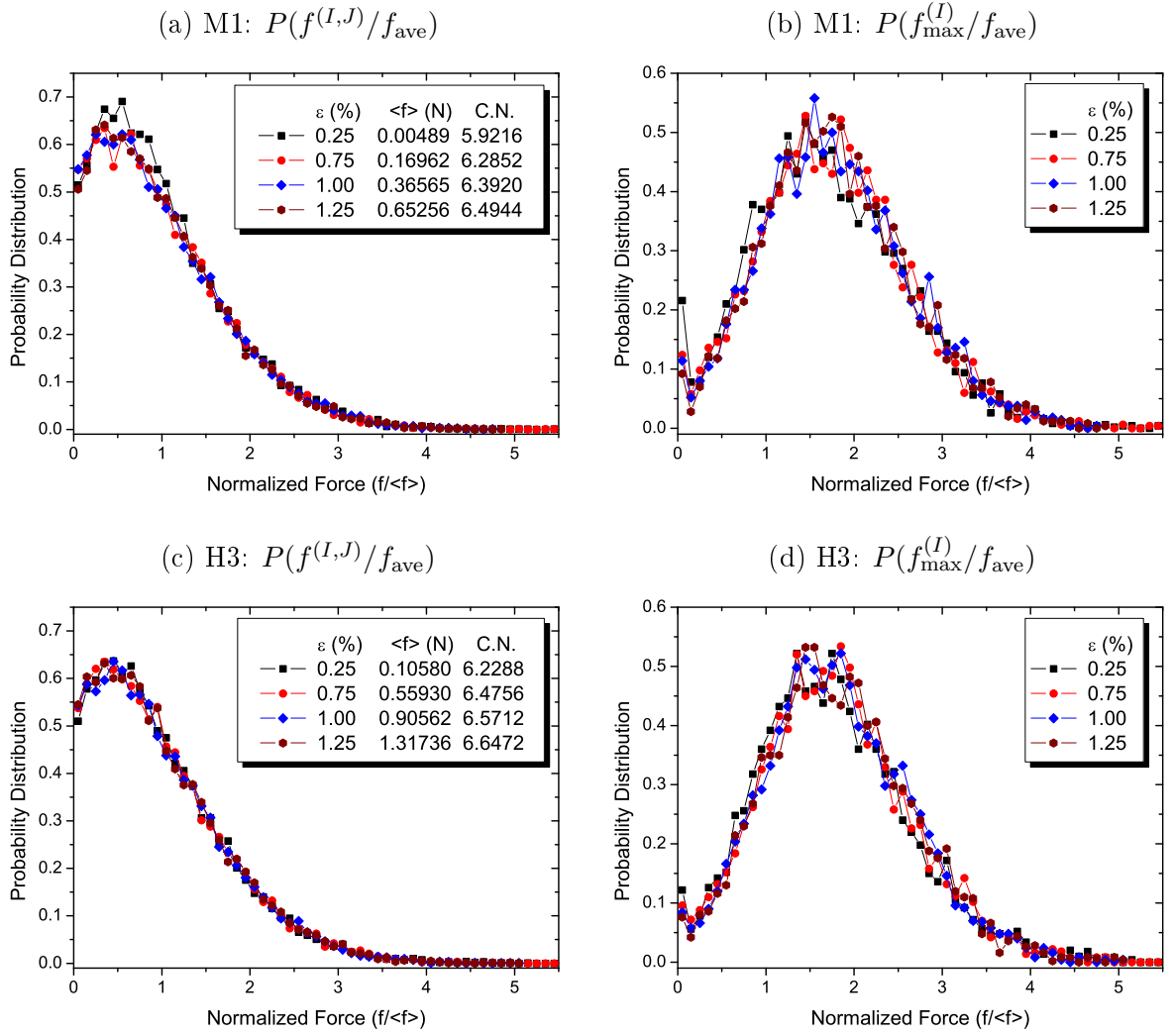
Figure 3.12: Probability distributions of: (a), (c) the normalized normal contact forces and (b), (d) normalized maximum normal contact forces of M1 and H3, respectively.

give the possibility to fit those data with a simple function. Equation

$$n_C = 5.80 + 0.490p^{0.288} \tag{3.50}$$

gives the best fit for data of different cases between 0 and 8 MPa. This fit curve is also plotted in Figure 3.13 as a dashed line for comparison.

Figure 3.14 shows the changes of contact forces, namely, the average normal contact forces f_{ave} and the maximum contact forces $f_{\max}$ in assemblies with medium and high packing factors, over the hydrostatic pressure. Here, the average normal contact force is

$$f_{\mathrm{ave}} = -2 \sum_{I<J} f_N^{(I,J)} / \left(n_C \cdot N \right) \; . \tag{3.51}$$

For the calculation of the hydrostatic pressure from Eqn. (3.25), $n_i n_i = 1$ and $n_i t_i = 0$. Neglecting the changes of the distance between two contacting particles, we have

$$p = -\frac{2r}{3V} \sum_{I<J} f_N^{(I,J)} \; . \tag{3.52}$$

36

For mono-sized assemblies, $\eta = N \cdot \frac{4}{3}\pi r^3 / V$. Thus, the hydrostatic compression can be expressed as follow

$$p = \frac{n_C \eta}{4\pi r^2} f_{\text{ave}} \ . \tag{3.53}$$

Here, the initial packing factor is chosen as $\eta = 0.64$ for all samples and the average coordination number n_C is calculated by Eqn. (3.50). Nemat-Nasser (2000) provided a similar relation for 2D cases, but here we show the dependency on not only the average normal contact force but also the coordination number. In Figure 3.14-(a), the approximation curve is plotted and gives a good representation of the data. Due to the occurrence of the radius, this relation can also applied to different systems with other values of particle radius.
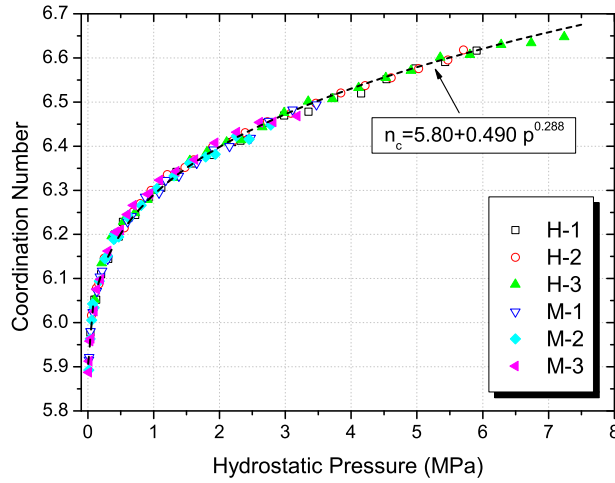
Figure 3.13: Average coordination number over macroscopic hydrostatic pressure.
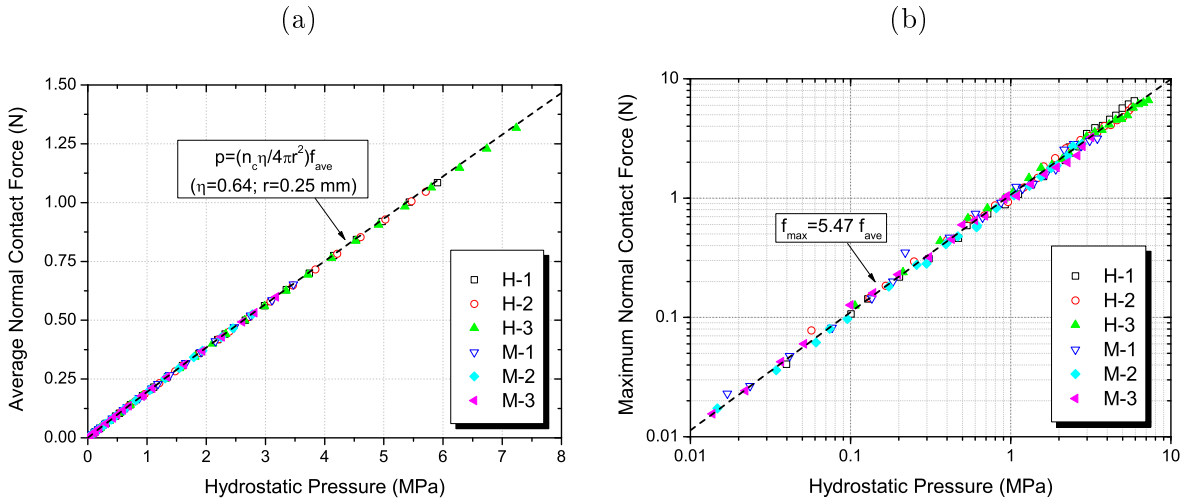
Figure 3.14: Contact forces over hydrostatic pressure: (a) average normal forces; and (b) maximum normal forces.

Figure 3.14-(b) shows the maximum forces f_{max} inside the assemblies, with respect to hydrostatic pressure. Usually, the maximum force is 5-6 times of the average normal force in an assembly. Neglecting scatter in the data of the maximum force, the relation

$$f_{\text{max}} = (5.47 \pm 0.474) f_{\text{ave}} \tag{3.54}$$

37

gives the best linear fit for the maximum force as a function of the average force. This curve is plotted in Figure 3.14-(b), agreeing well with the data from simulations. The maximum force f_{max} is important for the crush probability of individual pebbles. Eqs. (3.53) and (3.54) make it possible to estimate the maximum contact force based on the value of hydrostatic pressure.

For the crushing of single pebbles in a pebble bed, the following factors are essential: the contact force distributions $P(f)$ and $P(f_{max})$, the coordination number n_C, the maximum contact force f_{max} in the assembly, as well as the behaviour of single pebbles (Marketos and Bolton, 2007). Except for the last factor, which needs systematical experimental study on the crush load of single pebbles, the discrete element simulations presented here are capable to describe all those issues mentioned above.

3.6 Summary

In this chapter, the discrete element method is used to analyze the mechanical response of assemblies of pebbles. In addition to the basic theoretical background of DEM, the preparation of initial configurations is studied numerically.

The simulation of uniaxial compression tests shows that the initial packing factor plays an important role in the mechanical response to the external excitation. A macroscopic irreversible deformation of pebble beds has been observed for assemblies with only elastic particles, suggesting that the rearrangement of particles is an important mechanism for macroscopic irreversibility. For different external loading levels and samples, the normalized force distributions are the same in view of statistics. Furthermore, the average coordination number, as well as the average and maximum normal contact forces are obtained as a function of the macroscopic hydrostatic pressure. This discrete element investigation gives not only a basic understanding of the response of pebble beds, but also the possibility to characterize the pebbles in a microscopic way.

Chapter 4

Phenomenological Modelling

In the previous chapter, we have simulated pebble beds under uniaxial compression using the discrete element method. In order to analyze typical HCPB-TBM structures, the finite element method is most often required. To this end, a phenomenological model describing constitutive behaviour of the material is essential. It is also possible to use a micro-mechanics based constitutive model to characterize the overall phenomena of pebble beds. However, elaborate discrete element simulations of proportional loading have to be carried out first. This procedure needs much computational effort to take into account different factors which influence the overall behaviour of pebble beds, such as more practical size distributions of pebbles, and realistic interaction laws, etc. Therefore, constitutive models based on a micro-mechanical approach, as sequential multi-scale modelling, remain scarce in literature. It is convenient to directly use some common material models for granular materials, e.g., the Drucker-Prager-Cap model (Drucker and Prager, 1953), to perform thermo-mechanical analyses of pebble beds under fusion-relevant conditions (Bühler, 2002; Reimann et al., 2002; Hofer and Kamlah, 2005). The characteristics of these phenomenological models include a pressure-dependent elasto-plasticity. Plastic flow after yielding is described by non-associated flow rules (Collins and Houlsby, 1997).

In the HCPB concept, a pebble bed has typical dimension on the order of 10^{-1} m, but is composed of nearly spherical particles with typical diameter of 10^{-3} m. Thus, a continuum mechanics approach is appropriate for investigating thermo-mechanical responses of the materials to the external excitation. The main experimental phenomena of pebble beds are non-linear elasticity, pressure-dependent plasticity, volumetric creep and strain-dependent thermal conductivity. To describe the overall thermo-mechanical behaviour of pebble beds, the present material model is mainly based on the following:

- a non-linear elasticity law describes the observed stress-dependent elasticity;

- the modified Drucker-Prager-Cap model predicts the yielding and hardening behaviour;

- the time-dependent behaviour or the thermal creep is modelled by a so-called consolidation (cap) creep mechanism;

- finally, the strain dependent-thermal conductivity and thermal expansion obtained in experiments are also implemented.

In this chapter, the present phenomenological model will be discussed in detail. The identification method for the material parameters will be introduced in Chapter 5, and the implementation of the material model into a finite element code can be found in Chapter 6.

4.1 Nonlinear elasticity law

For stress states inside the yield surface, it is assumed that the material behaves elastically. During unloading and reloading in experiments (oedometric or uniaxial compression tests), nonlinear and non-hysteretic behaviour has been observed. This nonlinear elasticity can be explained through the understanding of inter-particle contacts inside the assembly. According to the Hertzian solution, the elastic contact force is nonlinear with respect to displacement, suggesting that if the compressive stress increases, the overall stiffness of the assembly will increase instead of staying constant. Another issue is the increase of the coordination number due to attachment and detachment of particles. In Chapter 3, the change of the average coordination number with respect to macroscopic stresses has been shown in the discrete element simulation. This indicates that new contact pairs are formed when compressive stresses are increasing, which makes the assembly more stiff than in the original configuration. Since in experiments, the unloading paths are parallel at different deformation levels, we consider the nonlinear elastic properties to be a function of stresses rather than strains.

In order to take into account the stress dependence of elastic moduli, the complementary energy density function can be written as

$$w^c(\boldsymbol{\sigma}) = \int_0^{\boldsymbol{\sigma}} \boldsymbol{\varepsilon}^e : \mathrm{d}\boldsymbol{\sigma} \ . \tag{4.1}$$

Thus, w^c is a stress potential function for elastic strains

$$\varepsilon_{ij}^e = \frac{\partial w^c}{\partial \sigma_{ij}} \ . \tag{4.2}$$

The stress and strain tensors can be decomposed into spherical and deviatoric parts as

$$\begin{aligned} \sigma_{ij} &= \frac{1}{3}\sigma_{kk}\delta_{ij} + s_{ij} \\ \varepsilon_{ij} &= \frac{1}{3}\varepsilon_{kk}\delta_{ij} + e_{ij} \ . \end{aligned} \tag{4.3}$$

Here, s_{ij} and e_{ij} denote the deviatoric stress and strain tensors, respectively. For an isotropic elastic body, the complementary energy density is a function of stress invariants, i.e. the hydrostatic pressure p and the von Mises stress q. In terms of the principle stresses, q and p may be expressed as:

$$\begin{aligned} q &= \sqrt{\frac{3s_{ij}s_{ij}}{2}} = \sqrt{\frac{(\sigma_1 - \sigma_2)^2 + (\sigma_2 - \sigma_3)^2 + (\sigma_3 - \sigma_1)^2}{2}} \ , \\ p &= -\frac{1}{3}\sigma_{kk} = -\frac{\sigma_1 + \sigma_2 + \sigma_3}{3} \ . \end{aligned} \tag{4.4}$$

According to the theory of isotropic elasticity, we have

$$\begin{aligned} \varepsilon_{kk} &= -\frac{1}{K_s}p \\ e_{ij} &= \frac{1}{2G_s}s_{ij} \ . \end{aligned} \tag{4.5}$$

Here, K_s and G_s are the secant elastic compression and shear moduli, respectively, depending on the stress invariants. Usually, it is convenient to assume a constant Poisson's ratio, e.g., $\nu =$ const., and Young's modulus can be expressed as

$$E_s = 2(1 + \nu)G_s = 3(1 - 2\nu)K_s \ . \tag{4.6}$$

We substitute Eqs. (4.3) and (4.5) into Eqn. (4.1), and the complementary energy can be written as

$$w^c(\sigma_{ij}) = \int_0^{\sigma_{ij}} \big(- \frac{1}{3K_s}p\delta_{ij} + \frac{1}{2G_s}s_{ij}\big) \, \mathrm{d}(-p\delta_{ij} + s_{ij}) \ . \tag{4.7}$$

Due to relations

$$\delta_{ij}\delta_{ij} = 3 \text{ and } s_{ij}\delta_{ij} = 0 \ , \tag{4.8}$$

we have

$$\begin{aligned} w^c(\sigma_{ij}) &= \int_0^{\sigma_{ij}} \big(\frac{p}{K_s} \, \mathrm{d}p + \frac{s_{ij}}{2G_s} \, \mathrm{d}s_{ij}\big) \\ &= \int_0^p \frac{\mathrm{d}(p^2)}{2K_s} + \int_0^q \frac{\mathrm{d}(q^2)}{6G_s} \ . \end{aligned} \tag{4.9}$$

Eqn. (4.9) suggests an equivalent stress, which combines the effect of p and q, as

$$\sigma_e = \Big[\frac{3}{2}(1 - 2\nu)p^2 + \frac{1}{3}(1 + \nu)q^2\Big]^{1/2} \ . \tag{4.10}$$

By using this equivalent stress, the complementary energy can be expressed in the form

$$w^c = \int_0^{\sigma_e} \frac{\mathrm{d}(\sigma_e^2)}{E_s} \ . \tag{4.11}$$

The general non-trivial model corresponding to the assumption that E_s is a function of σ_e reads

$$E_s = E_0 + A_e\sigma_e^n \ . \tag{4.12}$$

Here, s and A_e are constants, and E_0 indicates an initial value of Young's modulus. When $n = 1$, the Young's modulus is a linear function of σ_e.

The work of Coube (1998) on powder die compaction has dealt with a material with a microstructure having similar characteristics as the pebble beds under consideration in this work. Therefore, the nonlinear elasticity law proposed by Coube is adopted for the present material model. This law possesses the structure of the classical Hooke's law, however, Young's modulus depends on the current stress state via the von Mises stress q and the hydrostatic pressure p in the form

$$E = E_0 + A_e\Big[\frac{3}{2}(1 - 2\nu)p^2 + \frac{1 + \nu}{3}q^2\Big]^{n/2} \ . \tag{4.13}$$

Note that this expression is equivalent to Eqn. (4.12). Figure 4.1 shows a contour plot of Young's modulus, Eqn. (4.13), in stress space, where the parameters are set as $\nu = 0.25$, $n = 0.6$.

4.2 Modified Drucker-Prager-Cap model

In the present model, the plasticity of pebble beds is described by the modified Drucker-Prager-Cap model, which is a commonly used constitutive model in geomechanics (Drucker and Prager,
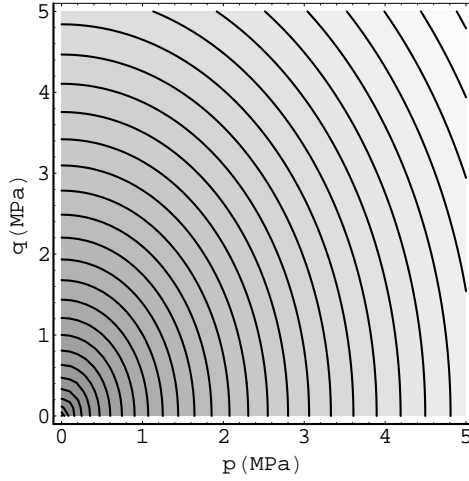
Figure 4.1: Contour plot of Young's modulus in the q-p plane.

1953; Vardoulakis and Sulem, 1995). This model has been implemented in the commercial finite element program, ABAQUS (ABAQUS, 2004a), representing yielding, hardening and time-dependent mechanical behaviour. The yield surface consists of the shear failure surface F_s and the cap surface F_c. Figure 4.2 gives a representation of the Drucker-Prager-Cap model in the q-p plane. The shear failure surface F_s characterizes the pressure-dependent shear failure loading. This describes a basic feature of granular materials: as the pressure increases, a higher shear loading is needed to initiate shear failure. The shear failure mechanism is usually combined with a non-associate plastic flow rule. The cap surface F_c describes the plastic behaviour under mainly hydrostatic compression. This is not present in classical metal plasticity, since for fully densified materials, the assumption is pressure-independent plasticity. Three unit cells are schematically drawn in Figure 4.2, to show an initial configuration inside the yield surface, a deformed configuration under shear stresses, and a consolidated one by yielding at the cap surface.

Figure 4.2: Modified Drucker-Prager-Cap model.

4.2.1 Formulas and related material parameters

In detail, the yield criterion F_s and the non-associated plastic flow potential G_s for shear failure surface are defined as

$$F_s = q - p \tan \beta - d = 0 \; , \tag{4.14}$$

$$G_s = \sqrt{[(p - p_a) \tan \beta]^2 + q^2} \; , \tag{4.15}$$

where

$$p_a = \frac{p_b - R \cdot d}{1 + R \tan \beta} \; . \tag{4.16}$$

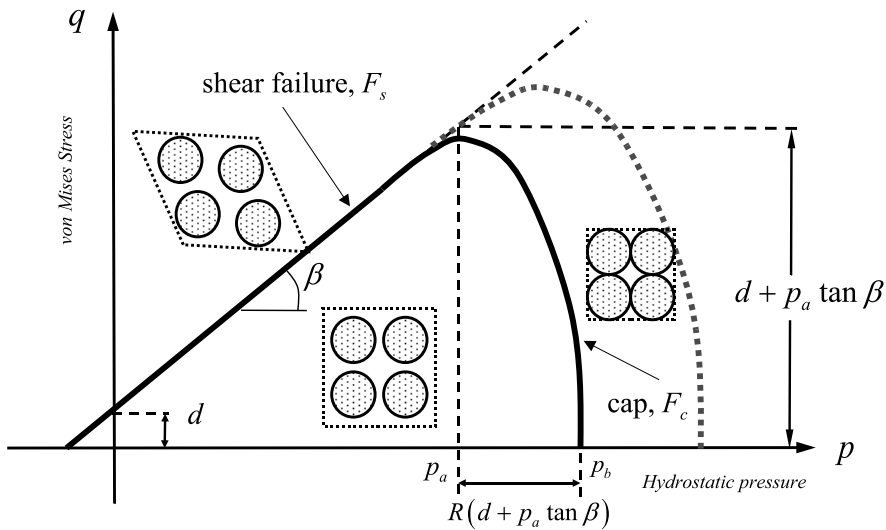For the cap surface, the yield criterion F_c and the associated flow potential G_c read as

$$F_c = \sqrt{[(p - p_a)]^2 + (R \cdot q)^2} - R(d + p_a \tan \beta) = 0 \; , \tag{4.17}$$

$$G_c = \sqrt{[(p - p_a)]^2 + (R \cdot q)^2} \; , \tag{4.18}$$

The plastic flow potentials G_s and G_c are parts of ellipses forming together a continuous and smooth potential surface. There are several material parameters that need to be identified, such as the constants β, R, d and the material function p_b.

Constant β is the Drucker-Prager friction angle defining the slope of the shear failure surface F_s. It is not identical to the friction angle of granular materials, and the relation between these two friction angles will be discussed in the next chapter. Constant d represents the value of von Mises stress related to the cohesion of the material. For the pebble beds under consideration here, the value of d is set almost to 0. Constant R controls the shape of the elliptic cap surface F_c. Finally, p_b defines the position of the ellipse F_c. The dependence of p_b on the hardening history is assumed to represent hardening properties of the material. For instance, in ABAQUS p_b is taken to be a function of the volumetric inelastic strain, i.e. $p_b(\varepsilon_{vol}^{in})$ (default with "*CAP HARDENING"). Furthermore, it is also possible to implement a hardening law based on the volumetric plastic strain, as $p_b(\varepsilon_{vol}^{p})$, or a work hardening law by a USDFLD (user-defined fields) routine.

4.2.2 Plastic flow theory

Since the plastic flow rule of the Drucker-Prager-Cap model is not given in detail in the ABAQUS manual, it will be deduced in the following. We discuss plastic flow in multi-surface and non-associated plasticity with $f^I(\boldsymbol{\sigma}, \boldsymbol{q}) = 0$ and $g^I(\boldsymbol{\sigma}, \boldsymbol{q})$ as the I-th yield (failure) criterion and the corresponding plastic flow-potential, where $\boldsymbol{q}$ is the set of internal variables, e.g., the hardening parameters. For instance, in the Drucker-Prager-Cap model, Eqs. (4.14), (4.15), (4.17) and (4.18) give the descriptions of the yield (failure) surfaces and plastic flow potentials on the shear failure surface and cap surface, respectively. First we define two second-order tensors as

$$
\begin{aligned}
\boldsymbol{\alpha}^I &= \frac{\partial f^I}{\partial \boldsymbol{\sigma}} \\
\boldsymbol{\beta}^I &= \frac{\partial g^I}{\partial \boldsymbol{\sigma}} \; .
\end{aligned}
\tag{4.19}
$$

According to the continuum theory of plasticity (Khan and Huang, 1995), the plastic strain increments can be written as

$$\mathbf{d}\boldsymbol{\varepsilon}^p = \sum_{I=1}^{I_0} \mathrm{d}\lambda\,\boldsymbol{\beta}^I \; , \tag{4.20}$$

where $\mathrm{d}\lambda$ is a factor of proportionality and I_0 is the number of the active yield surfaces. If the I-th yield (failure) surface is active, the corresponding consistency condition is given by the differential of the yield function as

$$\mathrm{d}f^I = \frac{\partial f^I}{\partial \sigma_{ij}}\mathrm{d}\sigma_{ij} + \frac{\partial f^I}{\partial q_i}\mathrm{d}q_i = 0 \; , \tag{4.21}$$

or in another form

$$\boldsymbol{\alpha} : \mathbf{d}\boldsymbol{\sigma} - A\,\mathrm{d}\lambda = 0 \; , \tag{4.22}$$

where

$$A = -\frac{1}{\mathrm{d}\lambda}\frac{\partial f^I}{\partial \boldsymbol{q}} \cdot \mathbf{d}\boldsymbol{q} \; . \tag{4.23}$$

The scalar function A depends on the hardening law. If the hardening parameters $\boldsymbol{q}$ can be written as a function of the plastic strains, $\boldsymbol{q} = \boldsymbol{q}(\boldsymbol{\varepsilon}^p)$, the differentiated form is

$$\mathbf{d}\boldsymbol{q} = \frac{\partial \boldsymbol{q}}{\partial \boldsymbol{\varepsilon}^p} : \mathbf{d}\boldsymbol{\varepsilon}^p \; . \tag{4.24}$$

Substituting Eqn. (4.24) into Eqn. (4.23) and replacing $\mathbf{d}\boldsymbol{\varepsilon}^p$, the scalar function A can be obtained as

$$A = -\frac{\partial f^I}{\partial \boldsymbol{q}} \cdot \frac{\partial \boldsymbol{q}}{\partial \boldsymbol{\varepsilon}^p} : \boldsymbol{\beta} \; . \tag{4.25}$$

If time-dependent effects are taken into consideration and only the yielding (hardening) mechanism I is active, the total strain increment can be decomposed into elastic, plastic and creep strain increments in the form

$$\begin{aligned} \mathbf{d}\boldsymbol{\varepsilon} &= \mathbf{d}\boldsymbol{\varepsilon}^e + \mathbf{d}\boldsymbol{\varepsilon}^p + \mathbf{d}\boldsymbol{\varepsilon}^{cr} \\ &= \left(\mathbf{C}^e\right)^{-1} : \mathbf{d}\boldsymbol{\sigma} + \mathrm{d}\lambda\,\boldsymbol{\beta} + \mathbf{d}\boldsymbol{\varepsilon}^{cr} \; , \end{aligned} \tag{4.26}$$

where $\mathbf{C}^e$ is the elastic stiffness matrix. Multiplying both sides of the above equation with $\boldsymbol{\alpha} : \mathbf{C}^e$ gives

$$\boldsymbol{\alpha} : \mathbf{C}^e : (\mathbf{d}\boldsymbol{\varepsilon} - \mathbf{d}\boldsymbol{\varepsilon}^{cr}) = \boldsymbol{\alpha} : \mathbf{d}\boldsymbol{\sigma} + \boldsymbol{\alpha} : \mathbf{C}^e : (\mathrm{d}\lambda\,\boldsymbol{\beta}) \; . \tag{4.27}$$

According to Eqn. (4.22), $\boldsymbol{\alpha} : \mathbf{d}\boldsymbol{\sigma}$ on the right hand side can be replaced by $A\,\mathrm{d}\lambda$, resulting in

$$\boldsymbol{\alpha} : \mathbf{C}^e : (\mathbf{d}\boldsymbol{\varepsilon} - \mathbf{d}\boldsymbol{\varepsilon}^{cr}) = A\,\mathrm{d}\lambda + \boldsymbol{\alpha} : \mathbf{C}^e : (\mathrm{d}\lambda\,\boldsymbol{\beta}) \; . \tag{4.28}$$

Thus, the factor of proportionality is obtained as

$$\mathrm{d}\lambda = \frac{\boldsymbol{\alpha} : \mathbf{C}^e : (\mathbf{d}\boldsymbol{\varepsilon} - \mathbf{d}\boldsymbol{\varepsilon}^{cr})}{\boldsymbol{\alpha} : \mathbf{C}^e : \boldsymbol{\beta} + A} \; . \tag{4.29}$$

We will discuss more details on the implementation of a general theory of thermo-elasto-plasticity in Chapter 6.

4.3 Representation of creep processes

For the Drucker-Prager-Cap model, two types of creep laws are defined in ABAQUS: consolidation creep and cohesion creep (ABAQUS, 2004b). In this investigation, only the consolidation creep mechanism is taken into account. This seems justified since pebble beds in fusion reactors are mainly in a tri-axial compression stress state. For consolidation creep, the creep potential is equal to the plastic potential, Eqn. (4.18), of the cap yield surface, i.e.

$$G_c^{cr} = \sqrt{(p - p_a)^2 + (R \cdot q)^2} \ . \tag{4.30}$$

The corresponding creep flow rule is given by

$$\boldsymbol{\Delta \varepsilon}^{cr} = \frac{\Delta \bar{\varepsilon}^{cr}}{f^{cr}} \frac{\partial G_c^{cr}}{\partial \boldsymbol{\sigma}} \ . \tag{4.31}$$

Here, $\boldsymbol{\Delta \varepsilon}^{cr}$ is the work conjugate to the stress tensor $\boldsymbol{\sigma}$ in terms of the creep dissipation energy. The work conjugate of the equivalent consolidation creep strain $\Delta \bar{\varepsilon}^{cr}$ is denoted by $\bar{\sigma}^{cr}$. Thus, f^{cr} is a proportionality factor defined as

$$f^{cr} = \frac{1}{\bar{\sigma}^{cr}} \boldsymbol{\sigma} : \frac{\partial G_c^{cr}}{\partial \boldsymbol{\sigma}} \ . \tag{4.32}$$

Bühler (2002) has used a strain hardening formulation for the creep law reading in the integrated form of equivalent consolidation creep strain $\Delta \bar{\varepsilon}^{cr}$ as:

$$\Delta \bar{\varepsilon}^{cr} = \left[\left(\frac{1}{m} A^* \exp\left(-\frac{B}{T}\right) p^n \right)^{1/m} \cdot \Delta t + (\bar{\varepsilon}^{cr,0})^{1/m} \right]^m - \bar{\varepsilon}^{cr,0} \ . \tag{4.33}$$

Here p is the hydrostatic pressure, $\bar{\varepsilon}^{cr,0}$ is the creep strain at the beginning of the time step Δt, and A^*, B, m and n are material parameters to be obtained from the experimental results.

In the ABAQUS implementation, consolidation creep occurs for stress states inside the area between the cap yield surface F_c and the critical line $p = p_a$ (see Figure 4.3). This means the condition for starting consolidation creep is $p > p_a$. Furthermore, in the "*CAP CREEP" option, the driving force for creep, i.e. the effective creep pressure, is defined as $\bar{\sigma}^{cr} = \bar{p}^{cr} = p - p_a$, providing a smooth transition to the region in which consolidation creep is not active ($p \leq p_a$).

For the purpose of this work, the ABAQUS consolidation creep option is not sufficient for the following reason: while the creep strain increases, by the harding law $p_b(\varepsilon_{vol}^{in})$, the value of p_a will increase simultaneously. For creep under constant hydrostatic pressure p, this means that the driving force $\bar{p}^{cr} = p - p_a$ will vanish gradually and, eventually, creep will be stopped. For instance, the starting point of the creep calculation locates inside the cap yield surface, once the creep strains are increasing, the cap surface will be moved by hardening until the critical line $p = p_a$ surpasses the starting point, which terminates the increasing of creep strains, in Figure 4.3.

One possible modification is to define a hardening law depending only on the volumetric plastic strain, as $p_b(\varepsilon_{vol}^p)$. This totally avoids any hardening effects introduced by creep strains. However, in two-step creep experiments (Bühler and Reimann, 2002), the compressive stresses have been applied in two different steps at the same bed temperature, showing that hardening behaviour may also be introduced by creep strains. This phenomenon can also be explained
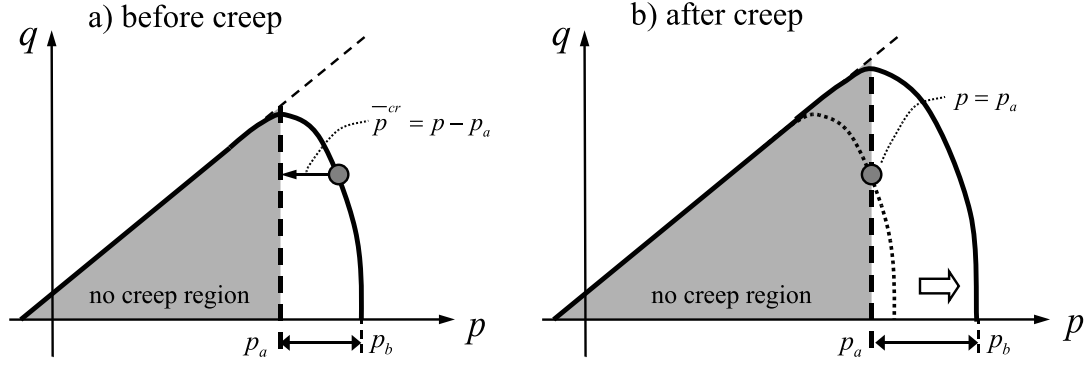
Figure 4.3: A schematic drawing of the evolution of the creep region and the effective creep pressure $\bar{p}^{cr}$.

from a micro-mechanics point of view. The creep deformation of pebble beds is caused by both creep of the bulk material and rearrangement of particles, which in turn increase the stiffness of the material. The selection of the types of hardening laws depends on the amount of volumetric creep strain present in the material under consideration. For materials with a small range of creep strains, the original ABAQUS definition is sufficient. If there are large creep strain amplitudes, the modification based on $p_b(\varepsilon_{vol}^p)$ is necessary to obtain correspondingly larger value of the creep strains. The other solution for this problem is to rewrite the material model, in a way to totally avoid these drawbacks of the implementation in ABAQUS by changing the definition of the critical line for creep calculation (see details in Chapter 6).

Moreover, according to its definition, the driving force $\bar{p}^{cr} = p - p_a$ can not be measured directly from experiments. Therefore, the parameters of the creep model need to be identified. One straightforward modification is to set $\bar{p}^{cr} = p$, which is identical to hydrostatic pressure (Bühler and Reimann, 2002).

4.4   Other thermo-mechanical properties

4.4.1   Effective thermal conductivity

It is well established in literature that the effective thermal conductivity of pebble beds is related to not only the properties of solid and gas phases, but also the contact areas between particles (Batchelor and O'Brien, 1977; Schlünder, 1982; Madhusudana, 1995). As one of the major heat transfer mechanisms in pebble beds, the particle-to-particle heat transfer depends on both the area of the contact zone, which is a result of contact forces, and the coordination number (Chan and Tien, 1973).

As discussed in the previous chapter, the discrete element method shows a non-uniform distribution of contact forces inside the assembly. Moreover, the discrete element simulation reveals the changes of the coordination number (n_C) and the average normal force (f_{ave}) with respect to the stress state, which are two important factors to the effective thermal conductivity (k_{eff}) of pebble beds. With the increase of f_{ave}, the average contact area increases, and meanwhile the change of n_C indicates the formation of new contact pairs during loading. As a result, the

value of k_{eff} increases. Figure 4.4 schematically shows the influence of the stress state on the effective thermal conductivity of an assembly. Although the contact areas of particles in a small assembly can be experimentally observed with the help of micro-tomography (Reimann et al., 2006c), the exact contact areas of pebble beds are difficult to be obtained due to the large number of pebbles. Hence, researchers have used macroscopic strains to characterize the average size of contact areas and the number of contact points. For elastic unloading, the effective thermal conductivity does not change notably, so the volumetric inelastic strain, ε_{vol}^{in}, is used here to represent the change of k_{eff}.
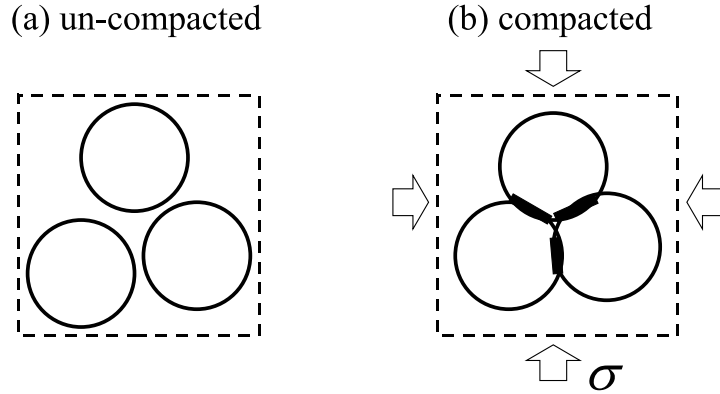
(a) un-compacted   (b) compacted

Figure 4.4: Influence of the mechanical loading on the effective thermal conductivity of pebble beds.

Experiments have been carried out to measure the effective thermal conductivity of beryllium pebble beds (Reimann et al., 2005b, 2006b) and ceramic breeder pebble beds (Reimann and Hermsmeyer, 2002), by the hot wire method. It is found that the effective thermal conductivity of beryllium pebble beds changes significantly between un-compacted and compacted pebble beds. This change has a notable impact on the thermo-mechanical analysis. It gives rise to a full (and nonlinear) thermo-mechanical two-way-coupling, excluding the classical staggered approach of first solving the thermal boundary value problem and then in a second step computing mechanical equilibrium for the obtained thermal strains. As a consequence, it is essential to model the material behaviour with respect to the change of thermal conductivity. By systematical experimental investigation of the effective thermal conductivity of beryllium pebble beds for different compressive strains (ε_{vol}^{in}) and temperatures (T), an empirical equation describing the strain-dependent thermal conductivity has been obtained (Reimann et al., 2005b):

$$
\begin{aligned}
k_{\text{eff}} =& 1.81 + 0.0012 \cdot T - 5 \times 10^{-7} \cdot T^2 \\
& + (9.03 - 1.386 \times 10^{-3} \cdot T - 7.6 \times 10^{-6} \cdot T^2 + 2.1 \times 10^{-9} \cdot T^3) \cdot \varepsilon_{vol}^{in} .
\end{aligned}
\tag{4.34}
$$

Here, the units for k_{eff}, T and ε_{vol}^{in} are $W/(mK)$, ^oC and %, respectively. The functional form of Eqn. (4.34) is adopted from the semi-empirical Schlünder-Zehner-Bauer (SZB) model and the coefficients are identified from experiments. It has been determined for bed temperatures between 200 and 650^oC and for a maximum strain of 3.5%.

The effective thermal conductivity has been measured for Li_4SiO_4 pebble beds, with the reference diameter distribution from 0.25 mm to 0.63 mm. The experiments have been carried out under bed temperatures ranging from room temperature to 800 ^oC and a maximum pressure of 6.5

MPa. The correlation has been found as (Reimann and Hermsmeyer, 2002)

$$k_{\text{eff}} = 0.768 + 4.96 \times 10^{-4} \cdot T + 0.045 \cdot \varepsilon_{vol}^{in} \ . \tag{4.35}$$

The same unit system is used as Eqn. (4.34). The volumetric inelastic strain-dependent thermal conductivity $k(\varepsilon_{vol}^{in}, T)$ found in experiments, which is represented by Eqs. (4.34) and (4.35), has been implemented in ABAQUS by a user-defined fields routine. This makes a fully coupled thermo-mechanical analysis possible under fusion-relevant conditions, as the change of deformation has a strong influence on the thermal conductivity and, thus, on the temperature field.

4.4.2 Other thermo-mechanical properties

Furthermore, the coefficients of thermal expansion and the specific heat for different pebble beds have been obtained directly from experiments. Databases were provided in the framework of European Fusion Development Agreement (EFDA) (Fokkens, 2003, 2005, etc.), see Appendix A. These properties have been implemented in ABAQUS as functions of temperature in this investigation.

4.5 Summary

In this chapter, the thermo-mechanical properties of ceramic and beryllium pebble beds are modelled using continuum mechanics. Motivated by the results of the experimental investigation, the present phenomenological model is mainly composed of a nonlinear elasticity law, the Drucker-Prager-Cap model, a consolidation creep law and a volumetric inelastic strain-dependent thermal conductivity.

Some discussions are made on the material parameters in the phenomenological model and on the limitation of the consolidation creep mechanism. The present constitutive model can be applied in the finite element code for fully coupled thermo-mechanical analyses of pebble beds under fusion-relevant conditions.

Chapter 5

Identification of Material Parameters

For the investigation of thermo-mechanical behaviour of pebble beds, different phenomenological models have been proposed (Bühler, 2002; Fokkens, 2003; Dell'Orco et al., 2007). However, these models often introduce new parameters, the physical meanings of which may be relatively obscure. Due to the difficulty to perform stress-controlled multi-axial experiments on granular materials, it is common to tune the parameters of the proposed material model based on experimental results of uniaxial compression (oedometric) tests by the trial-and-error method. Using this strategy, it is possible to provide different sets of parameters, which can well represent the uniaxial compression test but may fail under other loading paths. Concerning not only the varieties of types of pebble beds, but also strong temperature-dependent behaviour, a customized identification method of parameters is important to avoid unnecessary effort to find the proper sets of parameters for arbitrary conditions. In this chapter, we present an identification method of material parameters of the phenomenological model by analyzing the stress-strain state in the experiment. Moreover, validations of elasto-plasticity and creep are carried out for the present phenomenological model.

5.1   Determination of material parameters

The present phenomenological model describes the thermo-mechanical properties of pebble beds in terms of non-linear elasticity, plasticity, time-dependent effects and thermo-mechanical interactions by a multi-parameter system. The only available experimental basis for the determination of the material parameters is the uniaxial compression test (UCT), which is not strictly a stress-controlled proportional loading. It is impossible to directly use the experimental data in the material model. Therefore, it is necessary to find relations between the experiments and the material parameters in the present material model.

In this section, the determination of the material parameters from experiments is discussed. With this identification method, the relation between the hardening law and experimental results can be determined uniquely, and no trial-and-error method is necessary. This method is mainly based on the analysis of the stress-strain state in uniaxial compression tests, therefore, the experiments will be introduced first.

5.1.1 Uniaxial compression tests

The uniaxial compression test or oedometric experiment, see Figure 5.1, is one of the basic experimental setups to characterize the properties of granular materials, such as soil and sand. In Figure 5.1, the loading force F_y and the displacement of the pressure plate represent the overall stress and strain states in the experiments. The dimensions of the container are sufficiently larger than the one of individual pebbles to provide the representative overall behaviour of pebble beds. The transverse dimensions are much larger than the height to minimize wall effects, such as pebble-wall friction. On the other hand, in UCTs, the wall around the specimen is fixed. In contrast to stress-controlled uniaxial compression or hydrostatic compression, this means a combination of stress and strain boundary conditions.

Experimental investigations of the ceramic breeder and beryllium pebble beds have been performed by FZK (Reimann and Mueller, 1998; Reimann and Behnke, 1999; Reimann et al., 2000a). A typical stress-strain curve can be found in Figure 5.2, including loading, unloading, reloading and creep processes.

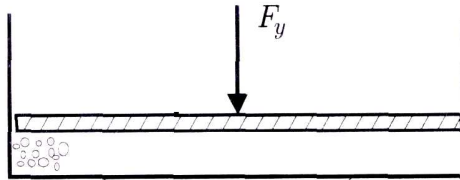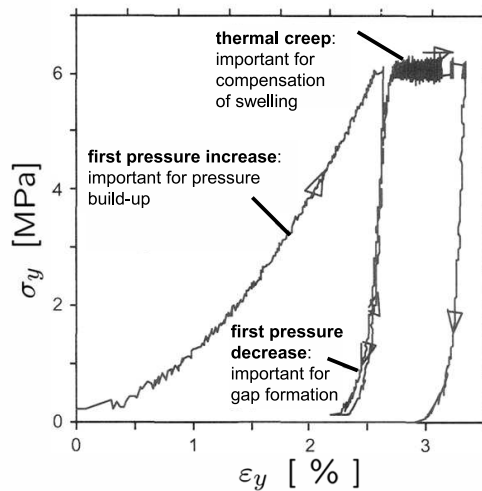Figure 5.1: A sketch of the uniaxial compression test.

Figure 5.2: A typical stress-strain curve of the uniaxial compression test.

UCTs have been carried out for various temperature levels, starting from room temperature to 900 ^{o}C for Li_4SiO_4 and 480 ^{o}C for beryllium pebble beds. The loading and unloading branches of the stress-strain curves are represented by separate temperature-dependent empirical

fit functions as

$$\sigma^L = \left[C_1^L \left(C_2^L + C_3^L T^{C_4^L} \right) \varepsilon \right]^{\frac{1}{1-C_5^L}}$$

$$\sigma^U = \left[C_1^U \left(C_2^U + C_3^U T^{C_4^U} \right) \varepsilon \right]^{\frac{1}{1-C_5^U}} \; . \tag{5.1}$$

Superscripts L and U indicate the loading and unloading branches. For each material, coefficients C_i^L and C_i^U are chosen such to yield optimum representation of the experimental loading and unloading curves.

The results of a few biaxial compression experiments can also be found in literature (Hermsmeyer and Reimann, 2002). While usually pebble beds are under triaxial compression in working conditions, triaxial results are difficult to be obtained in experiments. Therefore, the material parameters will have to be identified based on these available experimental data.

5.1.2 Deformation mechanism of UCT

The stress state of the uniaxial compression test, Figure 5.1, can be sketched as Figure 5.3. Since $\sigma_x = \sigma_z$, the problem is reduced to an axisymmetric one. In this case, the von Mises stress q and the hydrostatic pressure p, as in Eqn. (4.4), are given by

$$q = |\sigma_y - \sigma_x| \; ,$$

$$p = -\frac{\sigma_y + 2\sigma_x}{3} \; . \tag{5.2}$$
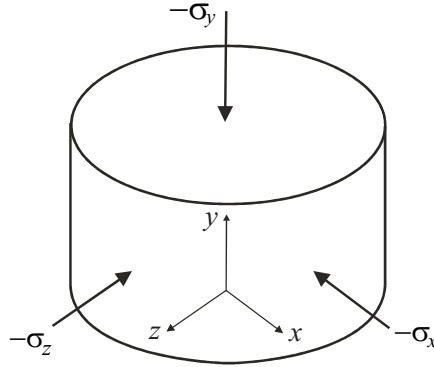
Figure 5.3: Stress state of the uniaxial compression test.

As the material deforms elastically, the relations

$$\sigma_x = \sigma_z = \frac{\nu}{1-\nu}\sigma_y \; ,$$

$$\sigma_y = \frac{1-\nu}{(1+\nu)(1-2\nu)} E\varepsilon_y \; , \tag{5.3}$$

can be obtained by the theory of isotropic elasticity. One remark has to be made here of isotropically elasticity. The assumption seems to be justified within comparably low compressive stress in the case of "soft" compaction. With the first equation in Eqn. (5.3), the non-linear Young's modulus in Eqn. (4.13) reads as

$$E = E_0 + A_e \left[\frac{2(1-\nu)}{(1+\nu)(1-2\nu)} \right]^{-s/2} (\sigma_y)^s \; . \tag{5.4}$$

Here, only the superscript n in Eqn. (4.13) is changed to s. The above relation is valid during pure elastic deformation only, since use has been made of elasticity in Eqn. (5.3). During elasto-plastic loading, however, the ratio between the principle stresses of elastic loading in Eqn. (5.3) needs to be updated. Thus, Eqn. (5.4) is the prediction of Young's modulus based on elasticity in the uniaxial compression test.

For elasto-plastic loading, a sketch of the loading and unloading paths in the σ_y-σ_x plane is plotted in Figure 5.4. This is an alternative representation of the Drucker-Prager-Cap surface, and it is valid for the special type of the axisymmetric stress state acting in the uniaxial compression test (see Figure 5.3). The dotted line is the yield (failure) surface, transferred to the σ_y-σ_x plane. If the cap yield surface is active during loading in the uniaxial compression test, the following equations are satisfied by the yield criterion F_c and plastic flow potential G_c

$$F_c = 0 \ ,$$
$$\left.\frac{\partial G_c}{\partial \sigma_x}\right|_{\sigma_x = \sigma_z} = 0 \ . \tag{5.5}$$

The first equation is the cap yield criterion, satisfied while the cap yield is active, and the second one is derived from the plastic flow potential by taking into account the condition of rigid side walls in UCT (see Section 4.2.2). During the compression, $\varepsilon_x = \varepsilon_z = 0$ is valid due to the rigid wall condition, but for the increments of plastic strains in the transverse plane, the second equation in Eqn. (5.5) is an approximation to the condition on the total strains.
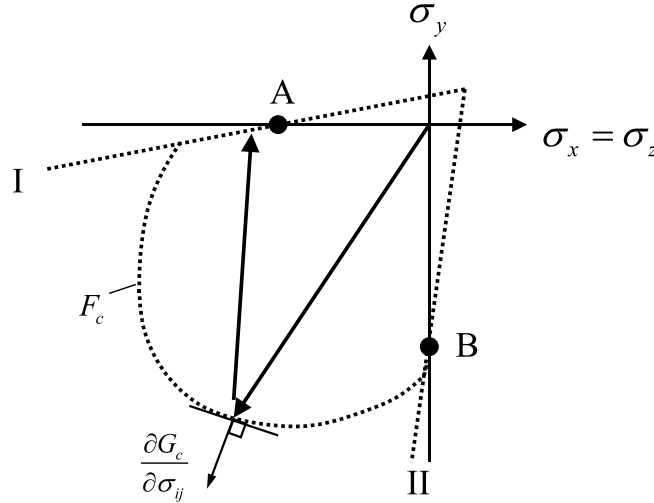
Figure 5.4: A sketch of the loading and unloading paths of UCT in the σ_y-σ_x plane.

Expressing Eqn. (5.5) in terms of the principle stresses for the case of axisymmetric loading, this system of equations can be solved for the harding parameter p_b as a function of stress component σ_y, giving

$$p_b = -\frac{3\sec^2\beta(\cos\beta + R\sin\beta)\times(-3\cos\beta + \sqrt{4+9R^2}\sin\beta)}{-9+(4+9R^2)\tan^2\beta}\sigma_y \ . \tag{5.6}$$

Eqn. (5.6) can not provide the definition of the hardening law yet, but there is possibility to reveal the relation between the compressive stress and plastic strain through the empirical coefficients for uniaxial compression tests, as will be shown below.

5.1.3 Experimental coefficients for the loading and unloading paths

First, we recall the empirical curves by Reimann for the UCT. While in the unloading branch σ^U of Eqn. (5.1), strain ε represents purely elastic strain changes during unloading, the strain in the loading branch σ^L is the sum of the elastic and plastic strain changes during loading. Thus, Eqn. (5.1) can be written as

$$
\begin{aligned}
\sigma^L &= \left[C_1^L \left(C_2^L + C_3^L T^{C_4^L} \right) (\varepsilon^e + \varepsilon^p) \right]^{\frac{1}{1-C_5^L}} , \\
\sigma^U &= \left[C_1^U \left(C_2^U + C_3^U T^{C_4^U} \right) \varepsilon^e \right]^{\frac{1}{1-C_5^U}} .
\end{aligned}
\tag{5.7}
$$

Comparing the non-linear Young's modulus in Eqn. (5.4) to the elastic (unloading) part of experimental coefficients in Eqn. (5.7), we identify

$$
\begin{aligned}
\frac{E_0}{E} &\to 0 , \\
s &= C_5^U , \\
A_e &= 2 C_1^U \left(C_2^U + C_3^U T^{C_4^U} \right) f(\nu)^{1-s/2} g(\varepsilon_{vol}^{in}) ,
\end{aligned}
\tag{5.8}
$$

where

$$
\begin{aligned}
f(\nu) &= \frac{(1+\nu)(1-2\nu)}{2(1-\nu)} , \\
g(\varepsilon_{vol}^{in}) &= 1 + \frac{\varepsilon_{vol}^{in}}{\varepsilon_{vol,0}^{in}} .
\end{aligned}
\tag{5.9}
$$

In Eqn. (5.8), $g(\varepsilon_{vol}^{in})$ is a function to adjust the difference between the elastic prediction according to Eqn. (5.4) and the exact elasto-plastic loading path. Eqn. (5.4) is valid only in pure elastic deformation. Once the material had behaved irreversibly, the ratio of stresses will be different from Eqn. (5.3), even for the case of elastic unloading. The present non-linear elasticity law depends on the stress state, however the elastic prediction is different from the elasto-plastic loading path because of the changes of inelastic strains. The difference in these two stress states is accounted for approximately by the function $g(\varepsilon_{vol}^{in})$. Here, only the first order, or the linear functional form, of $g(\varepsilon_{vol}^{in})$ is taken into account, and the values of $\varepsilon_{vol,0}^{in}$ are chosen to fit the empirical curves.

Next, we eliminate the elastic strain change in the elasto-plastic (loading) part of Eqn. (5.7) by means of the corresponding unloading part and solve the plastic strain change to obtain

$$
\varepsilon^p = \frac{(\sigma_y)^{1-C_5^L}}{C_1^L \left(C_2^L + C_3^L T^{C_4^L} \right)} - \frac{(\sigma_y)^{1-C_5^U}}{C_1^U \left(C_2^U + C_3^U T^{C_4^U} \right)} .
\tag{5.10}
$$

Note the dependence on both experimental parameter sets for loading and unloading paths, namely, C_i^L and C_i^U.

Combining Eqs. (5.6) and (5.10), the hardening law $p_b \sim \varepsilon^p$ is obtained. Note that variable ε^p here can be obtained in uniaxial compression tests as in Eqn. (5.10) with respect to the compressive stress σ_y, representing the overall volumetric plastic/inelastic strain of the beds. To each value of ε^p, there is related a unique value of p_b in the analytical form depending on the values of C_i^L and C_i^U as they are provided by the experimental data. So, with the procedure

discussed above, the parameters for elasto-plasticity in the present phenomenological model can be determined unambiguously from the experimental results without any trial-and-error method. Discussions concerning other material parameters, such as β and R, can be found in Section 5.3.1 and 5.3.2.

5.2 Validation

For the purpose of validation, the material data from the uniaxial compression test are needed. The experimental coefficients can be varied by different properties of bulk materials, different size distributions of particles, etc. In this section, the validation has been made based on the material database (Reimann et al., 2006a) for the pebble beds used in two out-of-pile mock-up experiments, namely HELICA and HEXCALIBER, carried out in ENEA Brasimone. The uni-axial compression tests and creep experiments are simulated, and compared with experimental results.

5.2.1 Validation for hardening law

The coefficients for Eqn. (5.1) are listed in Table 5.1 (Reimann et al., 2006a), for both ceramic breeder and beryllium pebble beds. The material parameters are determined with the present identification method by using these experimental coefficients as inputs. As validation, we simulate the uniaxial compression tests with the present method. The comparisons are made between the experimental curves and simulation by a single finite element (8-node axisymmetric thermally coupled element, CAX8RT in ABAQUS), see Figure 5.5.

Table 5.1: Coefficients for uniaxial compression tests of Li_4SiO_4 and beryllium pebble beds

i	Li_4SiO_4 C_i^L	C_i^U	Beryllium C_i^L	C_i^U
1	125.0	176.0	313.0	1074.0
2	1.0	1.0	1.0	1.0
3	-9.6×10^{-10}	0.0	0.0	0.0
4	3.0	3.0	0.0	0.0
5	0.50	0.66	0.33	0.60

For the pebble beds considered in this work, the Poisson's ratio $\nu = 0.25$ (Bühler, 1998). The procedure of determining the material parameters has been implemented in a USDFLD routine. As for beryllium pebble beds, we take $\varepsilon_{vol,0}^{in} = 0.02$, and for Li_4SiO_4 breeder pebble beds, $\varepsilon_{vol,0}^{in} = 0.05$ is used. Figure 5.5 shows a good agreement of the prediction by the method with the empirical curves for both loading and unloading branches. For Li_4SiO_4, calculations are made at different bed temperatures, from 50 to 850 ^oC, according to the temperature dependence suggested in the experiments. As good agreement is found at different temperature levels, this validation proves the accuracy of the method discussed above to determine the material parameters of both elasticity and plasticity in the present phenomenological model.
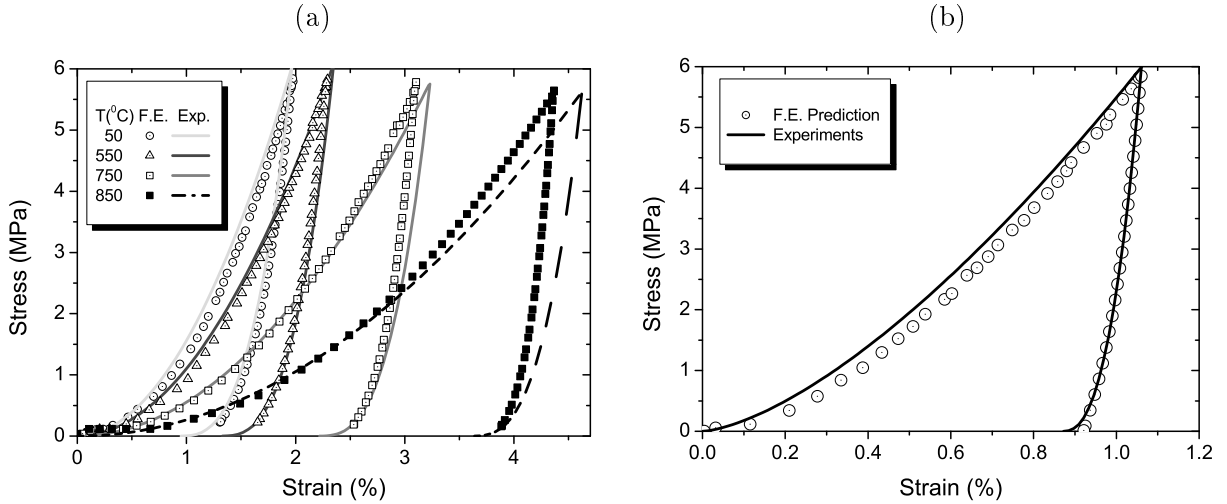
Figure 5.5: Uniaxial compression tests of: (a) Li_4SiO_4 under 50-850 ^oC; (b) beryllium pebble beds, comparison between FEA (dots) and empirical curves (lines).

5.2.2 Creep properties

Based on the creep experiments, empirical creep equations have been obtained (Reimann and Worner, 2001) of the type

$$\varepsilon^{cr} = A \exp\Big(- \frac{B}{T}\Big)\sigma^n t^m \ . \tag{5.11}$$

Parameters A, B, n and m have been determined by experiments for different materials, such as ceramic breeder and beryllium pebble beds. The parameters of Li_4SiO_4 and beryllium pebble beds (Reimann et al., 2006a) are listed in Table 5.2.

Table 5.2: Coefficients for creep experiments of Li_4SiO_4 and beryllium pebble beds

$\varepsilon^{cr}(\%) = A \exp(-\frac{B}{T(K)})\sigma(MPa)^n t(min)^m$			
	A	B	n	m
Li_4SiO_4	5143	11005	0.65	0.23
Beryllium	1614	9124	0.62	0.35

In view of the discussion in Section 4.3, the parameters (A^*, B, m, n) in Eqn. (4.33) can be identified from experiments for different materials. It has been reported that due to a bug the "strain hardening" form of the consolidation creep is not available in ABAQUS in analyses of two-step creep (Hofer and Kamlah, 2005). Therefore, consolidation creep has been re-implemented in ABAQUS by a CREEP routine. In contrast to the ABAQUS formulation reported in Section 4.3, in this investigation, the effective creep pressure $\bar{p}^{cr}$ is taken to be equal to the total hydrostatic pressure p at the current stress state. By this approach, the empirical equations for the experimental data can be used directly in the formulation of consolidation creep. Eqn. (5.11) is formulated in terms of uniaxial stress σ_y, whereas Eqn. (4.33) for the consolidation creep relies on hydrostatic pressure p. This difference is taken into account by the ratio A^*/A, while the other parameters (B, m, n) are identical to the experimental coefficients in both cases. In order to minimize the difference between the predictions of the model and experiments, we choose for

A^*/A the value of 1.45 for both Li$_4$SiO$_4$ and beryllium pebble beds, which have been used in HELICA and HEXCALIBER benchmark exercises (Reimann et al., 2006a).

The validation of the creep modelling has been made for different compressive stresses and bed temperatures for Li$_4$SiO$_4$ and beryllium pebble beds, respectively. Figure 5.6 shows a comparison between the model for simulation by a single finite element and the experimental results. For Li$_4$SiO$_4$ pebble beds, four typical examples are given with the maximum creep strain up to 5%, namely, (1) at 2.1 MPa and 700 ^oC, (2) at 2.1 MPa and 765 ^oC, (3) at 2.1 MPa and 850 ^oC, (4) at 4.1 MPa and 840 ^oC. For beryllium pebble beds, two typical examples are given with the maximum creep strain up to 2.3%, namely, (1) at 3.5 MPa and 550 ^oC, (2) at 1.5 MPa and 650 ^oC. Good agreements are found in Figure 5.6. It can be seen that the identification of the material constants for creep properties has been successful.

Furthermore, the two-step creep experiments (Reimann et al., 2005b) of beryllium pebble beds in Figure 5.7 may serve as an independent validation, since such a loading history was not the basis of the identification of these creep parameters. The prediction is made at a bed temperature of 605^oC, while the compressive stress changes from 1 MPa to 3.6 MPa at the second step. The comparison shows the present model is well capable of representing the creep processes in the pebble beds considered here.

(a)   (b)
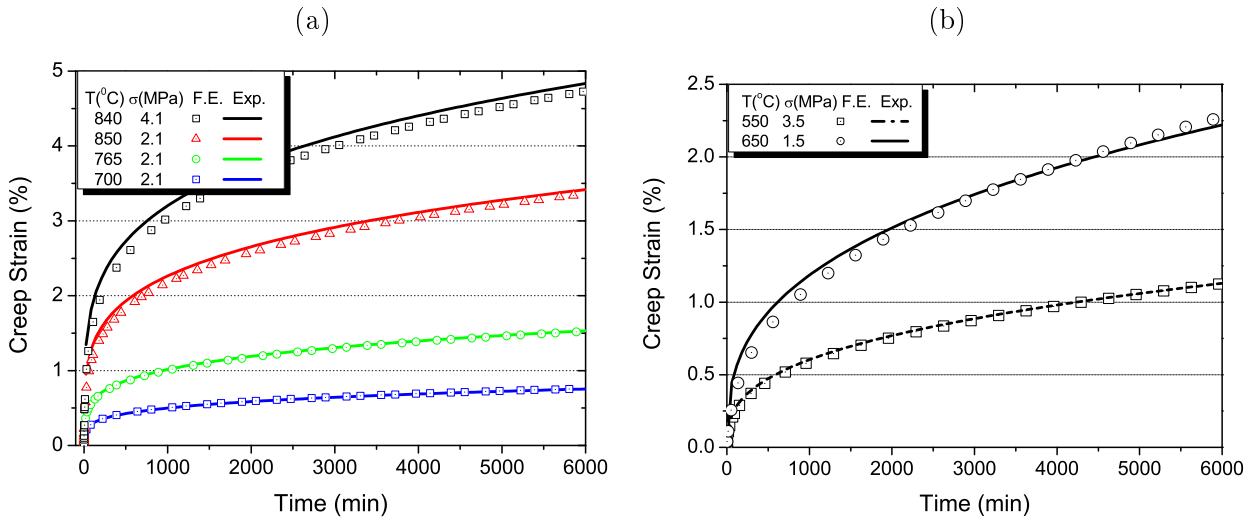
Figure 5.6: Creep tests of: (a) Li$_4$SiO$_4$ (b) beryllium pebble beds at different compressive stresses and temperatures, comparison between FEA (dots) and experimental results (lines).

5.3   Discussion

5.3.1   Softening behaviour during unloading

In previous material modelling (Hofer and Kamlah, 2005), the Drucker-Prager friction angle β has been chosen as 45°. Unrealistic plastic softening behaviour has been observed in the model when simulating unloading in the uniaxial compression tests to zero stresses resulting in an almost complete vanishing of the plastic strains. Figure 5.8 shows the stress-strain curves for different values of the Drucker-Prager friction angle β (40°, 45°, 60°). The smaller the β value,

Figure 5.7: Two-step creep experiment, comparison between the prediction and experiment.

the more pronounced softening behaviour is found. In Figure 5.4, the slopes of the shear failure surfaces are defined by β. Here we discuss the mechanism of this softening behaviour. For axisymmetric conditions, the shear failure surface F_s can be transformed form the q-p plane to the σ_y-σ_x plane as

$$
\begin{aligned}
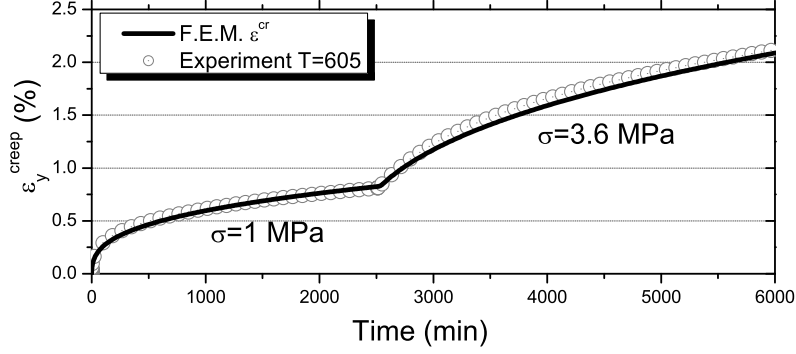\mathrm{I} \ &: \sigma_y - \sigma_x + \frac{1}{3}(\sigma_y + 2\sigma_x)\tan\beta - d = 0 \\
\mathrm{II} \ &: \sigma_x - \sigma_y + \frac{1}{3}(\sigma_y + 2\sigma_x)\tan\beta - d = 0 \ ,
\end{aligned}
\tag{5.12}
$$

where "I" and "II" refer to the shear failure surfaces in the σ_y-σ_x plane, respectively, see Figure 5.4. Thus, we may obtain the coordinates of the intersections (A and B) between the shear failure surfaces and the σ_x- and σ_y-axes. We get

$$
\begin{aligned}
\mathrm{A} \ &: \left(-\frac{d}{1 - \frac{2}{3}\tan\beta}, 0 \right) \ , \\
\mathrm{B} \ &: \left(0, -\frac{d}{1 - \frac{1}{3}\tan\beta} \right) \ .
\end{aligned}
\tag{5.13}
$$

For a relatively small d, as in the case of pebble beds, intersection A is close to the origin of the σ_y-σ_x plane. Consequently, the main reason for the softening behaviour while unloading is that the failure surface is hit before complete unloading to zero compressive stresses has occurred. If the unrealistic softening during unloading is to be totally avoided, the shear failure surface "I" should be nearly parallel to the σ_x-axis or have an intersection for $\sigma_x > 0$. This means a condition for the slope, i.e. β, and by Eqn. (5.13) we find

$$
\tan\beta \geq 1.5 \ .
\tag{5.14}
$$

As mentioned above, for a small value of β, the unloading path will hit the shear failure surface before the axial stress is reduced to zero, initiating the unrealistic softening behaviour during final unloading, while Eqn. (5.14) provides the condition to avoid such behaviour.

Note that the Drucker-Prager friction angle β is not identical to the commonly used friction angle μ_s of granular materials, but it is a function of the real friction angle. The Drucker-Prager
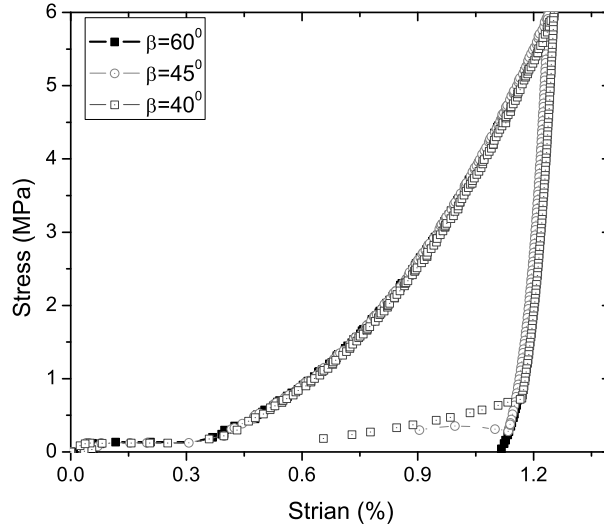
Figure 5.8: Effects of β on the softening behaviour while unloading.

friction angle β can be estimated by the Leonardo da Vinci's static friction experiment for a granular medium, see Figure 5.9-(1) (Duran, 1999). The static friction coefficient is defined as

$$\mu_s = \frac{T}{P} = \frac{\tau}{\sigma_n} \ . \tag{5.15}$$

The three-dimensional stress state in the static friction experiment is shown in Figure 5.9-(2). The stresses on the cubic element represent the stress state in the sheared middle layer of the experimental setup. By analyzing the stress state in the middle layer, it is found that the middle layer of the static friction experiment is in a similar stress state as the pebble beds in the uniaxial compression tests. The normal stresses in the transverse plane are determined by the effect of the Poisson's ratio and a condition of axisymmetry in this plane. Consequently, the stress tensor can be expressed as

$$\begin{pmatrix} \sigma_n & \tau & 0 \\ \tau & c \cdot \sigma_n & 0 \\ 0 & 0 & c \cdot \sigma_n \end{pmatrix} \ . \tag{5.16}$$

In this stress tensor, the stress ratio $c = \nu^*/(1 - \nu^*)$ depends on the kind of loading. For pure elastic deformation, $\nu^* = \nu^e$ is the elastic Poisson's ratio, similar to Eqn. (5.3). In the case of elasto-plastic deformation, $\nu^* = \nu^p$ is some history-dependent quantity with a value in the range of $0.0 \leq \nu^* \leq 0.5$. Expressing this stress state in the Drucker-Prager-Cap model as

$$q = \sqrt{\left(\frac{1 - 2\nu^*}{1 - \nu^*}\sigma_n\right)^2 + 3\tau^2}$$
$$p = \frac{1 + \nu^*}{3(1 - \nu^*)}\sigma_n \ , \tag{5.17}$$

in the case of non-cohesive materials, according to Eqn. (4.14), we have

$$\tan\beta = 3\frac{\sqrt{(1 - 2\nu^*)^2 + 3\mu_s^2(1 - \nu^*)^2}}{1 + \nu^*} \ . \tag{5.18}$$
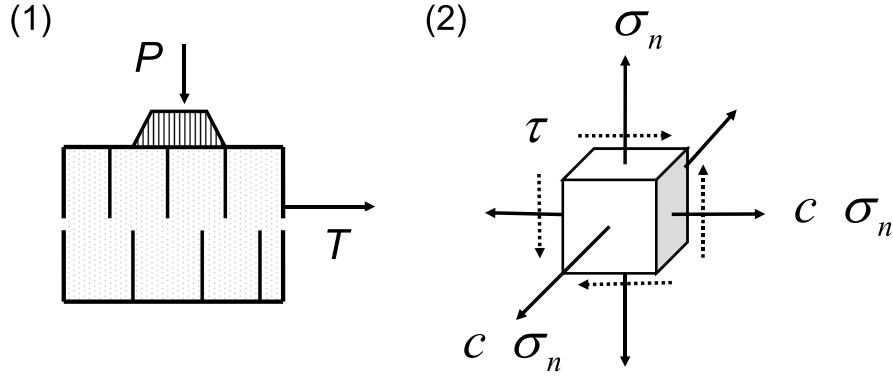
Figure 5.9: (1) A sketch of the typical experimental setup used to measure the coefficient of the static friction μ_s of a granular material; (2) the stress state in the sheared middle layer of the setup to the left.

Here, the Drucker-Prager friction angle β is expressed as a function of both the static friction coefficient μ_s and the Poisson's ratio ν^* ($= \nu^e$ or $= \nu^p$), see Figure 5.10. The value of β is a monotonic function of μ_s for $\mu_s \geq 0$.

The value of μ_s can be obtained by several kinds of experiments, and on the basis of μ_s, a rough range of the Drucker-Prager friction angle β can be estimated. For the shear failure surface to be parallel to the $\sigma_x(= \sigma_z)$-axis, the condition $\tan \beta = 1.5$ has to be satisfied (see Figure 5.4 and Eqn. (5.14)). By solving Eqn. (5.18), and considering the extreme condition of $\mu_s = 0$ for a totally non-frictional material, $\nu^* \leq \nu_0 = 0.2$ guarantees that the unloading path will not hit the shear failure surface. With a larger value of μ_s, the critical value of the Poisson's ratio ν_0 increases. In particular, $\nu_0 = 0.5$ for $\mu_s \geq \sqrt{3}/2$. By Eqn. (5.18), the region satisfying $\tan \beta \geq 1.5$ can be found in Figure 5.10.
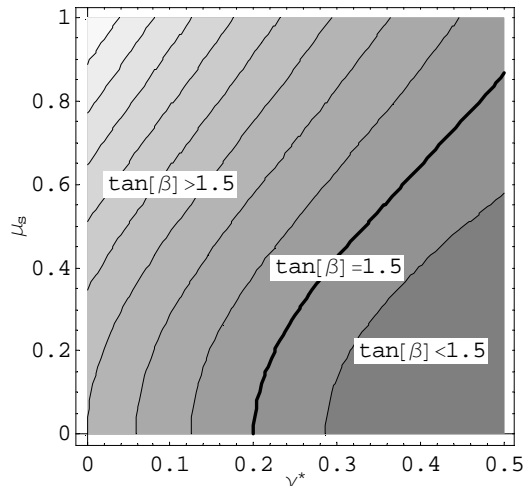

Figure 5.10: Contour plot of $\tan \beta$ as a function of the static friction coefficient μ_s and the Poisson's ratio ν^*, the bolded line shows the critical value of $\tan \beta$.

According to the available biaxial experimental data for ceramic breeder pebble beds (Hermsmeyer

and Reimann, 2002, and "*Material Assessment Report*" for ITER), the Drucker-Prager friction angle of the pebble beds can be calculated by analyzing the stress state in the biaxial compression. Following Eqn. (5.12) for the shear failure surface "II" in the axisymmetric stress plane, and assuming $d = 0$ for simplicity, we have:

$$\tan \beta = \frac{3(\sigma_y^0 - \sigma_x^0)}{\sigma_y^0 + 2\sigma_x^0} \ . \tag{5.19}$$

Superscript "0" indicates the failure stress in experiments. As a result, values of almost around 60° are found for the Drucker-Prager friction angle β of both ceramic breeder and beryllium pebble beds. As discussed above, such a value is in accordance with the criterion for avoiding unrealistic softening, i.e. Eqn. (5.14). Consequently, both the experimental results and theoretical considerations of the Drucker-Prager theory support the choice of the Drucker-Prager friction angle $\beta \approx 60^o$. On the other hand, as shown before, for such a value no unrealistic plastic softening behaviour occurs in the model.

5.3.2 Other material parameters

Most of the material parameters can be determined by the method presented above from the empirical equations of the experiments. However, some parameters are adjusted "manually", i.e. by trial-and-error, which does not affect the predictions in the uniaxial compression test but may possibly influence the ones in other loading paths. In principle, these parameters can be determined by experiments employing different loading paths, such as hydrostatic compression or triaxial compression. Figure 5.11 shows the impact of the parameter R on the simulation of hydrostatic compression. In Figure 5.11, the left plot shows the stress-strain curves and the right plot is the normal strain at 5 MPa versus the corresponding value of the parameter R.
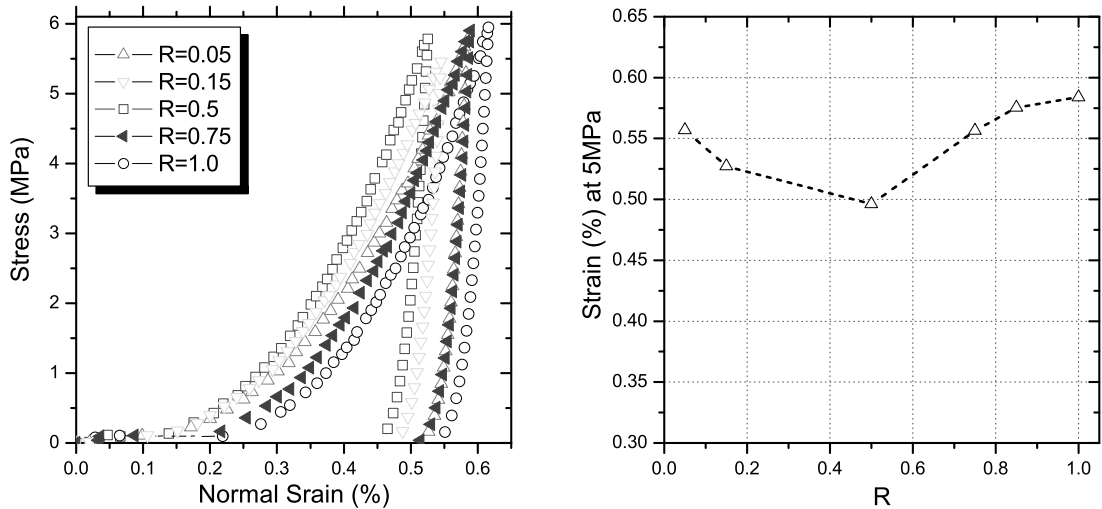

Figure 5.11: Hydrostatic compression with different values of R: *left*, stress-strain curves; *right*, strains at 5 MPa with different R-values.

In the present phenomenological model, only the determination of the value of R is missing. This constant controls the shape of cap surface, and mainly influences the direction of plastic

and creep flows. However, Figure 5.11 clearly shows that the stress-strain curves are not very sensitive to variations of R over a wide range. From the current point of view, these findings indicate that tremendous efforts for experiments with new type of loading states in order to exactly identify R seem not to be justified. Instead, some reasonable estimations for R will be sufficient for the purposes of this work. A reasonable large R results in a sufficient large active creep zone in the stress plane, see Figure 4.3. We hence choose $R = 0.9$ for both ceramic breeder and beryllium pebble beds in this investigation.

5.3.3 Advantages of the improvement

There are two main advantages of methods presented in this chapter. First, it is possible to directly use the empirical fit equations from the experiments to determine uniquely the set of material parameters, especially the hardening law, instead of using a trial-and-error method. The latter method may deliver various sets representing the uniaxial compression tests more or less well, however, they may result in totally different and possibly unphysical responses for other loading histories. By the method developed in this work, we uniquely identify the right set of these parameters.

Second, since this procedure can be carried out for different temperature levels, the temperature dependence of the hardening law is introduced into the model in an unambiguous way. This means that the thermo-plastic generalization of the constitutive model for pebble beds is obtained in a straightforward manner from the temperature-dependent empirical curves. Figure 5.12 shows a sketch of the yield (failure) surfaces in the stresses-temperature space. In this way, the inelastic response of the material at different temperatures can be predicted. Moreover, if the temperature varies, the theory might describe changed yielding behaviour of the material (Laloui and Cekerevac, 2003).
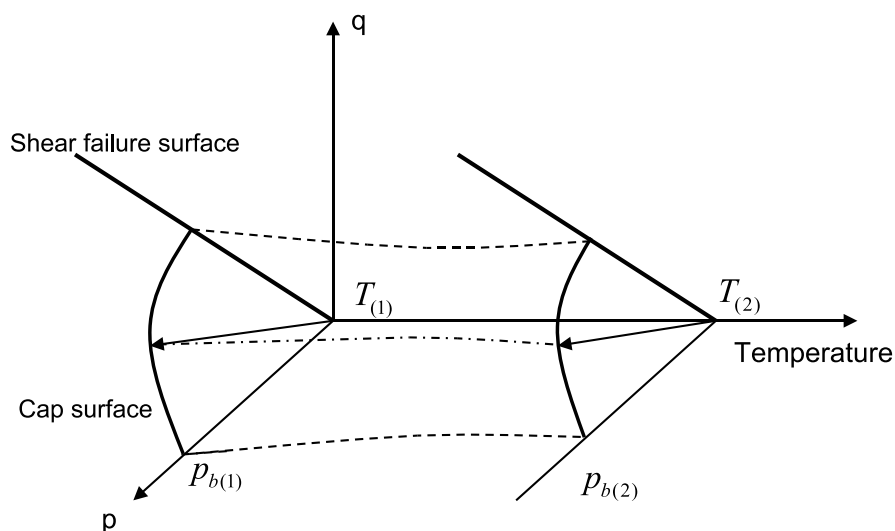

Figure 5.12: A sketch of the Drucker-Prager-Cap yielding/failure surfaces of thermo-plasticity.

The main result of unique and reliable identification of material parameters is to provide confidence in the physical significance of simulations based on the Drucker-Prager-Cap model. In summary, the relations between parameters in the Drucker-Prager-Cap model and experimental

results are listed briefly in Table 5.3, in order to give an overview of the present identification method.

Table 5.3: Summary of material parameters used in the phenomenological model

Parameters in the model	Expressed by experimental results
Non-linear elasticity	
A_e	Eqn. (5.8)
s	C_5^U
ν	0.25 (Bühler, 1998)
E_0	~ 0
Drucker-Prager-Cap model	
R	0.9
β	60° (Hermsmeyer and Reimann, 2002)
p_b	Eqs. (5.6) and (5.10)
d	~ 0
Creep law	
A, B, m, n	Experimental coefficients in Eqn. (5.11)

5.4 Summary

To determine the material parameters in the phenomenological model, a method is proposed here to find the proper set of these parameters from available experiments. This method is based on the analysis of the stress state and deformation in the uniaxial compression test, which is the basic experimental setup for characterizing the material properties of pebble beds. The hardening law of the Drucker-Prager-Cap theory is identified through empirical coefficients representing the experimental data.

Validation of the material model and identification method shows that the predictions of the model agree well with the experimental results. By using this method, the phenomenological model can be easily implemented for different types of pebble beds, and moreover thermo-plasticity can be realized without much effort.

Chapter 6

Implementation of the Material Model

In order to implement a phenomenological model into a finite element code, user-defined material routines are used to obtain information from the constitutive model, including the stress increments and the Jacobian matrix based on the given strain increments. The Drucker-Prager-Cap model has already been fixed in ABAQUS, but there are some limitations of the implementation, which can not be changed in an appropriate way, such as the creep/no-creep zones discussed in Chapter 4. The implementation in a user-defined material routine in this chapter can be used to overcome these problems. Furthermore, the same framework can be adopted if there are new material models proposed for pebble beds, for instance, a micro-mechanics based constitutive model. The current phenomenological model, consisting of the nonlinear elasticity law, Drucker-Prager-Cap model and consolidation creep, can be easily transferred from ABAQUS to other finite element codes.

In this chapter, first the implementation of a nonlinear elasticity law is presented, and the corresponding Jacobian matrix is given with respect to the state variables. A return mapping algorithm is used to solve the stress increments in plasticity, including both associated and non-associated plastic flow rules. Moreover, the elasto-plastic Jacobian matrix is calculated according to the strain increments and internal variables. Other properties, such as creep and thermo-mechanical interactions, are also employed in user-defined material routines to provide the possibility to carry out fully coupled thermo-mechanical analyses.

The Voigt notations are employed throughout this chapter. We use six-dimensional vectors to replace the second-order tensors, σ_{ij} and ε_{ij}, as

$$
\begin{aligned}
\boldsymbol{\sigma} &= \begin{bmatrix} \sigma_{11} & \sigma_{22} & \sigma_{33} & \sigma_{12} & \sigma_{23} & \sigma_{31} \end{bmatrix}^{\mathrm{T}} \\
\boldsymbol{\varepsilon} &= \begin{bmatrix} \varepsilon_{11} & \varepsilon_{22} & \varepsilon_{33} & 2\varepsilon_{12} & 2\varepsilon_{23} & 2\varepsilon_{31} \end{bmatrix}^{\mathrm{T}} .
\end{aligned}
\tag{6.1}
$$

Similar changes are made to their increments and components, such as $\mathbf{d}\boldsymbol{\sigma}$ and $\mathbf{d}\boldsymbol{\varepsilon}^p$. Thus the Voigt matrix notations are also applied to the fourth-order tensors, e.g., the stiffness tensor $\mathbf{C}$ and compliance tensor $\mathbf{S}$ are shortened by 6×6 matrixes. These changes are made for the sake of the convenience for programming.

6.1 User-defined material routines

To implement a constitutive model, e.g., using a UMAT (User-defined MATerial) routine in ABAQUS, the following information should be provided with respect to the incremental strain history from kinematic relations. First the stress tensor $\boldsymbol{\sigma}$ and internal variables, such as $\boldsymbol{\varepsilon}^p$ or more general $\boldsymbol{q}$, have to be updated based on the current strain increments $\boldsymbol{\Delta\varepsilon}$, given by the finite element code. If the elastic component can be separated from $\boldsymbol{\Delta\varepsilon}$ as $\boldsymbol{\Delta\varepsilon}^e$, the stress increments can hence be written as

$$\boldsymbol{\Delta\sigma} = \mathbf{C}^e \cdot \boldsymbol{\Delta\varepsilon}^e \ . \tag{6.2}$$

Here, $\mathbf{C}^e$ is the elastic stiffness matrix, which is the inverse tensor to the elastic compliance matrix $\mathbf{S}^e$, as $\mathbf{C}^e = (\mathbf{S}^e)^{-1}$.

The second part of the information needed for the user-defined material routine is the Jacobian matrix, or the consistent tangents. It can be defined as

$$\tilde{\mathbf{C}} = \frac{\partial \boldsymbol{\Delta\sigma}}{\partial \boldsymbol{\Delta\varepsilon}} \ . \tag{6.3}$$

Linearizing the relation between the stress and strain increments, the above equation satisfies

$$\boldsymbol{\Delta\sigma} = \tilde{\mathbf{C}} \cdot \boldsymbol{\Delta\varepsilon} \ . \tag{6.4}$$

The Jacobian matrix $\tilde{\mathbf{C}}$ is used to assemble the global stiffness matrix in the finite element code. Although it does not affect the local update scheme for stresses, it will obviously influence the convergence rate of the global Newton iteration, since $\tilde{\mathbf{C}}$ is the basis to calculate residuals during the current time increment and to predict the next strain increments. Different expressions can be obtained by the different integration schemes, implicit or explicit, adopted in the user-defined material routine with respect to the incremental strains.

Finally, the global momentum balance equation is tested for the computed stresses, and if violated, the iteration process is continued. Figure 6.1 shows the basic requirements for a typical user-defined material routine as discussed above. Inside the user-defined material routine, the integration scheme determines the internal variables $\boldsymbol{q}_{(n+1)}$ and stresses $\boldsymbol{\sigma}_{(n+1)}$ corresponding to the given strain increments $\boldsymbol{\Delta\varepsilon}$ within the time increment.
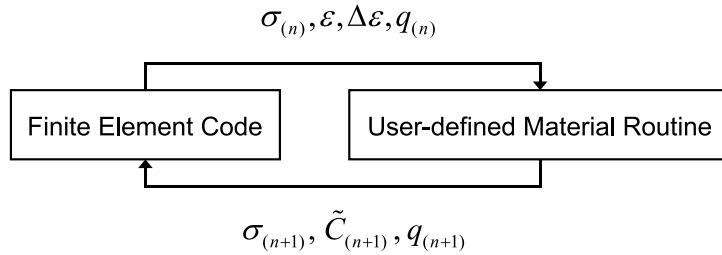

Figure 6.1: A typical interface between the finite element code and user-defined material routine.

6.2 Elasticity

For granular materials, it has been observed that the elastic constants depend on stresses, see Chapter 4. According to the nonlinear elasticity law used in the present phenomenological

64

model, Eqn. (4.13), only Young's modulus E depends on the current stress state. Thus the elastic stiffness matrix $\mathbf{C}^e$ and compliance matrix $\mathbf{S}^e$ read as

$$\mathbf{C}^e = \begin{vmatrix} 2G + \bar{\lambda} & \bar{\lambda} & \bar{\lambda} & 0 & 0 & 0 \\ \bar{\lambda} & 2G + \bar{\lambda} & \bar{\lambda} & 0 & 0 & 0 \\ \bar{\lambda} & \bar{\lambda} & 2G + \bar{\lambda} & 0 & 0 & 0 \\ 0 & 0 & 0 & G & 0 & 0 \\ 0 & 0 & 0 & 0 & G & 0 \\ 0 & 0 & 0 & 0 & 0 & G \end{vmatrix}, \tag{6.5}$$

where $\bar{\lambda} = \nu E/[(1+\nu)(1-2\nu)]$ is the first Lamé parameter, and

$$\mathbf{S}^e = \frac{1}{E} \begin{vmatrix} 1 & -\nu & -\nu & 0 & 0 & 0 \\ -\nu & 1 & -\nu & 0 & 0 & 0 \\ -\nu & -\nu & 1 & 0 & 0 & 0 \\ 0 & 0 & 0 & 2(1+\nu) & 0 & 0 \\ 0 & 0 & 0 & 0 & 2(1+\nu) & 0 \\ 0 & 0 & 0 & 0 & 0 & 2(1+\nu) \end{vmatrix}. \tag{6.6}$$

Based on the theory of elasticity and the requirements of the user-defined material routine, the Jacobian matrix $\tilde{\mathbf{C}}^e$ should be provided at each time increment for purely elastic loading as

$$\boldsymbol{\Delta\sigma} = \tilde{\mathbf{C}}^e \cdot \boldsymbol{\Delta\varepsilon} . \tag{6.7}$$

Since the stiffness matrix here depends on the stress state, the Jacobian matrix can be derived from the elastic stiffness matrix, Eqn. (6.5). The relation between stress and strain tensors can be written at the beginning and the end of the time increment as

$$\boldsymbol{\sigma} = \int_0^{\boldsymbol{\varepsilon}} \mathbf{C}^e(\boldsymbol{\sigma}) \cdot \mathbf{d}\boldsymbol{\varepsilon}$$

$$\boldsymbol{\sigma} + \boldsymbol{\Delta\sigma} = \int_0^{\boldsymbol{\varepsilon}+\boldsymbol{\Delta\varepsilon}} \mathbf{C}^e(\boldsymbol{\sigma}) \cdot \mathbf{d}\boldsymbol{\varepsilon} . \tag{6.8}$$

For sufficiently small strain increments $\boldsymbol{\Delta\varepsilon}$, we have

$$\boldsymbol{\Delta\sigma} = \int_{\boldsymbol{\varepsilon}}^{\boldsymbol{\varepsilon}+\boldsymbol{\Delta\varepsilon}} \mathbf{C}^e(\boldsymbol{\sigma}) \cdot \mathbf{d}\boldsymbol{\varepsilon} \approx \mathbf{C}^e(\boldsymbol{\sigma} + \boldsymbol{\Delta\sigma}) \cdot (\boldsymbol{\varepsilon} + \boldsymbol{\Delta\varepsilon}) - \mathbf{C}^e(\boldsymbol{\sigma}) \cdot \boldsymbol{\varepsilon} . \tag{6.9}$$

Here, the stress increments $\boldsymbol{\Delta\sigma}$ are unknown. The Taylor expansion is applied to the stress-dependent stiffness matrix $\mathbf{C}^e(\boldsymbol{\sigma})$

$$\mathbf{C}^e(\boldsymbol{\sigma} + \boldsymbol{\Delta\sigma}) = \mathbf{C}^e(\boldsymbol{\sigma}) + \frac{\partial \mathbf{C}^e(\boldsymbol{\sigma})}{\partial \boldsymbol{\sigma}} \cdot \boldsymbol{\Delta\sigma} , \tag{6.10}$$

presuming the stress increments are small and have negligible influence on the derivative of the stiffness matrix. Substituting Eqn. (6.10) into Eqn. (6.9) and writing the stress increments in the form of components of the tensors, we have

$$\Delta\sigma_i = C^e_{ij,k}\Delta\sigma_k\varepsilon_j + \left[C^e_{ij} + C^e_{ij,k}\Delta\sigma_k \right] \cdot \Delta\varepsilon_j . \tag{6.11}$$

Here, $(\bullet)_{,k}$ indicates the partial derivative of the quantity. After separating the stress and strain increments, we replace the dummy subscripts, i.e. i, j, k, l,

$$\left[\delta_{ki} - C^e_{kl,i}(\varepsilon_l + \Delta\varepsilon_l) \right] \cdot \Delta\sigma_i = C^e_{kj}\Delta\varepsilon_j . \tag{6.12}$$

Finally, the consistent tangents can be written as

$$\tilde{C}_{ij}^e = \left[\delta_{ki} - C_{kl,i}^e (\varepsilon_l + \Delta \varepsilon_l) \right]^{-1} \cdot C_{kj}^e \; . \tag{6.13}$$

This elastic Jacobian matrix depends on not only the current stress state, but also on the strains and strain increments. Thus, we have the consistent elastic tangents in Eqn. (6.13), and the stresses are updated by Eqn. (6.7) in the user-defined material routine. There is no symmetry of the consistent elastic tangents here. For linear elasticity, the symmetry of the consistent elastic tangents is satisfied automatically. However, for nonlinear elasticity, a fully explicit or a fully implicit scheme will provide the feature of symmetry-preserving (Ortiz and Martin, 1989).

6.3 Plasticity

Over the years, many researchers have proposed different types of integration schemes for constitutive equations of elasto-plasticity in the finite element method. Earlier approaches have mainly been based on a single scheme for the local integration, known as forward Euler. For global iterations, to solve the nonlinear equilibrium equations, Newton-Raphson and quasi-Newton methods can be applied with either a fixed Jacobian matrix or the updating secant modulus, and thus a number of iterations are needed to achieve convergence. These earlier methods need small incremental time steps to accomplish conditional stability.

Recently, algorithms using implicit methods to achieve unconditional stability have been developed (Ortiz and Popov, 1985; Ortiz and Simo, 1986; Ortiz and Martin, 1989; Keavey, 2002; Ahadi and Krenk, 2003). In an implicit integration scheme, the solution makes use of the final stress state and internal variables $(\boldsymbol{\sigma}_{(n+1)}, \boldsymbol{q}_{(n+1)})$, which are determined by solving nonlinear equations iteratively so that the stress increments fulfill the consistency condition. As one typical category presented in literature, some well-known return mapping algorithms are the radial return, closest point projection and cutting plane algorithms (Simo and Hughes, 1997). Therefore, different formulations of the consistent tangents have to be obtained by differentiation of the stress update algorithms with respect to the incremental strains.

6.3.1 Return-mapping algorithm

The essence of the general return-mapping algorithm is explained in the following. First, a "trail stress" $\boldsymbol{\sigma}_{(n+1)}^{(0)}$ is calculated by the elasticity law as an elastic predictor. If the stresses are substituted into the yield function and the value of the yield function is less than zero, the predicted stress state is the required stress state at the end of the increment, and no corrector step is needed. On the contrary, if the trail stress state locates outside the yield surface, then plastic flow takes place. In addition to the updating of stresses, the internal variables change gradually, and in turn, the yield surface moves at the same time. There are various corrector algorithms which take stresses back to the yield surface in the stress space.

In the current consideration, we use a forward Euler step, followed by a sequence of backward Euler steps, if the material behaves plastically. This procedure for the integration scheme of plasticity is sketched in Figure 6.2. In this figure, step (0) is the elastic predictor, step (1) is the forward Euler method and the following steps are computed by the backward Euler method. At

the beginning of each iteration step, the yield function and plastic flow potential are updated according to the end of the last iteration. During the current step, plastic flow depends on the updated stresses and variables, and the conditions for convergence are checked at the end of the current iteration. The conditions for convergence are set to ensure that the nonlinear equations are solved according to an implicit scheme.
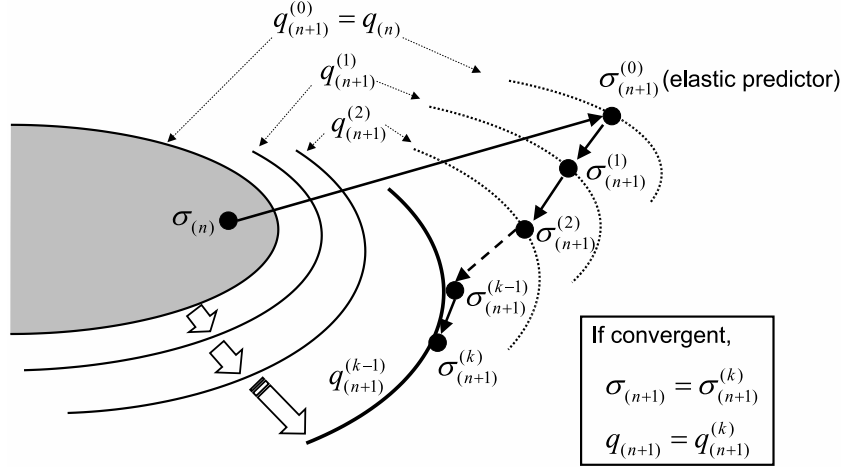

Figure 6.2: Procedure of the return mapping algorithm.

Here, for elasto-plastic deformation, we assume that the elastic stiffness matrix $\mathbf{C}^e$ stays unchanged during iterations in order to simplify the implementation of the integration scheme. The yield surface is

$$f(\boldsymbol{\sigma}, \boldsymbol{q}) = 0 \ , \tag{6.14}$$

and the corresponding plastic flow potential is

$$g(\boldsymbol{\sigma}, \boldsymbol{q}) \ . \tag{6.15}$$

Materials whose behaviour obeys the principle of normality are referred to as associated materials. For associated plastic flow, $f \equiv cg$, and here c is a constant. Many materials, such as geomaterials, are reputed to be non-associated, which implies that f and g do not coincide. The present phenomenological model employs both associated and non-associated flow potentials, see Chapter 4. Thus, a general case of non-associated plastic flow rules is investigated here.

We define the following vectors similar to Chapter 4, using the Voigt notations

$$
\begin{aligned}
\boldsymbol{\alpha} &= \frac{\partial f}{\partial \boldsymbol{\sigma}} = \begin{bmatrix} \frac{\partial f}{\partial \sigma_{11}} & \frac{\partial f}{\partial \sigma_{22}} & \frac{\partial f}{\partial \sigma_{33}} & \frac{\partial f}{\partial \sigma_{12}} & \frac{\partial f}{\partial \sigma_{23}} & \frac{\partial f}{\partial \sigma_{31}} \end{bmatrix}^{\mathrm{T}} \ , \\
\boldsymbol{\beta} &= \frac{\partial g}{\partial \boldsymbol{\sigma}} = \begin{bmatrix} \frac{\partial g}{\partial \sigma_{11}} & \frac{\partial g}{\partial \sigma_{22}} & \frac{\partial g}{\partial \sigma_{33}} & \frac{\partial g}{\partial \sigma_{12}} & \frac{\partial g}{\partial \sigma_{23}} & \frac{\partial g}{\partial \sigma_{31}} \end{bmatrix}^{\mathrm{T}} \ .
\end{aligned}
\tag{6.16}
$$

In general, the stress increment tensor $\boldsymbol{\Delta\sigma}$ depends on the incremental strain tensor $\boldsymbol{\Delta\varepsilon}$ given at the beginning of this time increment according to

$$\boldsymbol{\Delta\sigma} = \mathbf{C}^e \cdot (\boldsymbol{\Delta\varepsilon} - \Delta\lambda\,\boldsymbol{\beta}) \ , \tag{6.17}$$

or

$$\boldsymbol{\sigma} = \boldsymbol{\sigma}^e - \Delta\lambda\,\mathbf{C}^e \cdot \boldsymbol{\beta} \ . \tag{6.18}$$

Here, we define a stress tensor as the elastic predictor $\boldsymbol{\sigma}^e(= \boldsymbol{\sigma}^{(0)}) = \boldsymbol{\sigma}_{(n)} + \mathbf{C}^e \cdot \boldsymbol{\Delta\varepsilon}$, which is updated according to the stress tensor $\boldsymbol{\sigma}_{(n)}$ at the end of the last time increment. For this first prediction, the factor of proportionality $\Delta\lambda^{(0)} = 0$, and the yield condition is checked using this elastic predictor $\boldsymbol{\sigma}^e$. If the stress state locates outside the yield surface, plastic increments are calculated with the help of the factor of proportionality $\Delta\lambda^{(k)}$ as

$$\boldsymbol{\Delta\varepsilon}^{p,(k)} = \Delta\lambda^{(k)}\,\boldsymbol{\beta}^{(k)} \ . \tag{6.19}$$

The superscript (k) indicates the number of iterations.

First, the forward Euler method is used to guess an initial value of $\Delta\lambda^{(1)}$ and $\boldsymbol{\sigma}^{(1)}$, based on the value of $\boldsymbol{\sigma}^e$,

$$\Delta\lambda^{(1)} = \frac{f}{\boldsymbol{\alpha}^{\mathrm{T}} \cdot \mathbf{C}^e \cdot \boldsymbol{\beta} + A}$$
$$\boldsymbol{\sigma}^{(1)} = \boldsymbol{\sigma}^e - \Delta\lambda^{(1)}\,\mathbf{C}^e \cdot \boldsymbol{\beta} \ . \tag{6.20}$$

The details of this process can be found in Section 4.2.2. The contributions of the internal variables $\boldsymbol{q}$ are taken into account in parameter A. If the internal variables $\boldsymbol{q}$ can be written as a function of plastic strain $\boldsymbol{\varepsilon}^p$, e.g., the hardening parameter $p_b(\varepsilon^p_{vol})$ in the Drucker-Prager-Cap model, the parameter A can be calculated by

$$A = -\frac{\partial f}{\partial \boldsymbol{q}} \cdot \frac{\partial \boldsymbol{q}}{\partial \boldsymbol{\varepsilon}^p} \cdot \boldsymbol{\beta} \ . \tag{6.21}$$

Usually, the first estimation will not satisfy the convergence criterion, and hence the backward Euler method is applied in the following. For the k-th iteration (the first forward Euler step is named as the 1st iteration), a residual vector is defined as

$$\mathbf{r} = \boldsymbol{\sigma}^{(k-1)} - (\boldsymbol{\sigma}^e - \Delta\lambda\,\mathbf{C}^e \cdot \boldsymbol{\beta}^{(k-1)}) \ . \tag{6.22}$$

This residual vector describes the difference between the iterative solution $\boldsymbol{\sigma}^{(k-1)}$ and Eqn. (6.18). This vector is calculated at the beginning of the k-th iteration. To reach convergence of the integration, it should be sufficiently small, which guarantees a fully implicit integration scheme, as $|\mathbf{r}| \leq$ tolerance. A truncated Tailor expansion is applied to the residual vector and the yield function as

$$\mathbf{r}^t = \mathbf{r} + \boldsymbol{\delta\sigma}^{(k-1)} + \delta\lambda\,\mathbf{C}^e \cdot \boldsymbol{\beta}^{(k-1)} + \Delta\lambda\,\mathbf{C}^e \cdot \boldsymbol{\delta\beta}^{(k-1)}$$
$$f^t = f + \boldsymbol{\alpha}^{(k-1)} \cdot \boldsymbol{\delta\sigma}^{(k-1)} - \delta\lambda\,A^{(k-1)} \ . \tag{6.23}$$

The operator $\delta(\bullet)$ indicates a variational form of the quantity with respect to a sufficient small time increment δt, and here $\delta\lambda$ is used to indicate the variation of $\Delta\lambda$.

Note that the plastic flow vector $\boldsymbol{\beta}$ is a function of not only stresses but also internal variables, for instance, plastic strains, expressed in the form of $\boldsymbol{\beta}(\boldsymbol{\sigma}, \boldsymbol{\varepsilon}^p)$. Thus $\boldsymbol{\delta\beta}$ can be writen as

$$\boldsymbol{\delta\beta} = \frac{\partial \boldsymbol{\beta}}{\partial \boldsymbol{\sigma}} \cdot \boldsymbol{\delta\sigma} + \frac{\partial \boldsymbol{\beta}}{\partial \boldsymbol{\varepsilon}^p} \cdot \boldsymbol{\delta\varepsilon}^p \ . \tag{6.24}$$

The value of $\boldsymbol{\delta\varepsilon}^p$ can be calculated by $\delta\lambda\,\boldsymbol{\beta}$.

The conditions for the approximate solution can be written as $\mathbf{r}^t = 0$ and $f^t = 0$. The first condition ensures that the stresses are updated by Eqn. (6.18) according the state variables

at the end of the time increment, and the second one is the consistency condition for rate-independent plasticity. Solving Eqn. (6.23) with the above conditions, we have the solution for the k-th iteration

$$\delta\lambda = \frac{f - \boldsymbol{\alpha}^{\mathrm{T}} \cdot \mathbf{R} \cdot \mathbf{r}}{\boldsymbol{\alpha}^{\mathrm{T}} \cdot \mathbf{R} \cdot \mathbf{C}^e \cdot \mathbf{Q} \cdot \boldsymbol{\beta} + A^{(k-1)}} \ ,$$
$$\boldsymbol{\delta\sigma}^{(k-1)} = -\mathbf{R} \cdot \left(\mathbf{r} + \delta\lambda\, \mathbf{C}^e \cdot \mathbf{Q} \cdot \boldsymbol{\beta} \right) \ . \tag{6.25}$$

Here, two additional matrixes are defined as

$$\mathbf{Q} = \mathbf{I} + \Delta\lambda\, \frac{\partial \boldsymbol{\beta}}{\partial \boldsymbol{\varepsilon}^p} \ ,$$
$$\mathbf{R} = \left(\mathbf{I} + \Delta\lambda\, \mathbf{C}^e \cdot \frac{\partial \boldsymbol{\beta}}{\partial \boldsymbol{\sigma}} \right)^{-1} \ , \tag{6.26}$$

where $\mathbf{I}$ is the identity matrix of dimension of 6×6, and it can also be written using the Kronecker delta notation.

Using Eqn. (6.25), the updated stresses and factor of proportionality read as

$$\boldsymbol{\sigma}^{(k)} = \boldsymbol{\sigma}^{(k-1)} + \boldsymbol{\delta\sigma}^{(k-1)}$$
$$\Delta\lambda^{(k)} = \Delta\lambda^{(k-1)} + \delta\lambda \ . \tag{6.27}$$

The iteration stops if the following convergence conditions

$$|\mathbf{r}| \leq \xi \ ,$$
$$|f| \leq \zeta \ , \tag{6.28}$$

are satisfied, where ξ and ζ are tolerances. Otherwise, additional iterations are needed by using the backward Euler method. The procedure of the return mapping algorithm used in this investigation is summarized in Figure 6.3 as a flow chart.

6.3.2   Stiffness matrix

After convergence is reached in the return mapping algorithm, the internal variables and stresses at the end of the time increment are updated. Here, we derive the stiffness matrix $\tilde{\mathbf{C}}$ according to the state variables at the end of the time increment. The variational form of Eqn. (6.18) is

$$\boldsymbol{\delta\sigma} = \mathbf{C}^e \cdot \boldsymbol{\delta\varepsilon} - \delta\lambda\, \mathbf{C}^e \cdot \boldsymbol{\beta} - \Delta\lambda\, \mathbf{C}^e \cdot \boldsymbol{\delta\beta} \ , \tag{6.29}$$

and using Eqn. (6.24), we separate the variables

$$\left[\mathbf{I} + \Delta\lambda\, \mathbf{C}^e \cdot \frac{\partial \boldsymbol{\beta}}{\partial \boldsymbol{\sigma}} \right] \cdot \boldsymbol{\delta\sigma} = \mathbf{C}^e \cdot \boldsymbol{\delta\varepsilon} - \delta\lambda\, \mathbf{C}^e \cdot \boldsymbol{\beta} - \Delta\lambda\, \mathbf{C}^e \cdot \frac{\partial \boldsymbol{\beta}}{\partial \boldsymbol{\varepsilon}^p} \cdot (\delta\lambda\, \boldsymbol{\beta}) \ . \tag{6.30}$$

Simplifying Eqn. (6.30) with matrixes $\mathbf{R}$ and $\mathbf{Q}$ in Eqn. (6.26),

$$\boldsymbol{\delta\sigma} = \mathbf{R} \cdot \left[\mathbf{C}^e \cdot \boldsymbol{\delta\varepsilon} - \delta\lambda\, \mathbf{C}^e \cdot \mathbf{Q} \cdot \boldsymbol{\beta} \right] \ . \tag{6.31}$$

Then substituting Eqn. (6.31) into the variational form

$$\delta f = \boldsymbol{\alpha}^{\mathrm{T}} \cdot \boldsymbol{\delta\sigma} - A\, \delta\lambda = 0 \tag{6.32}$$
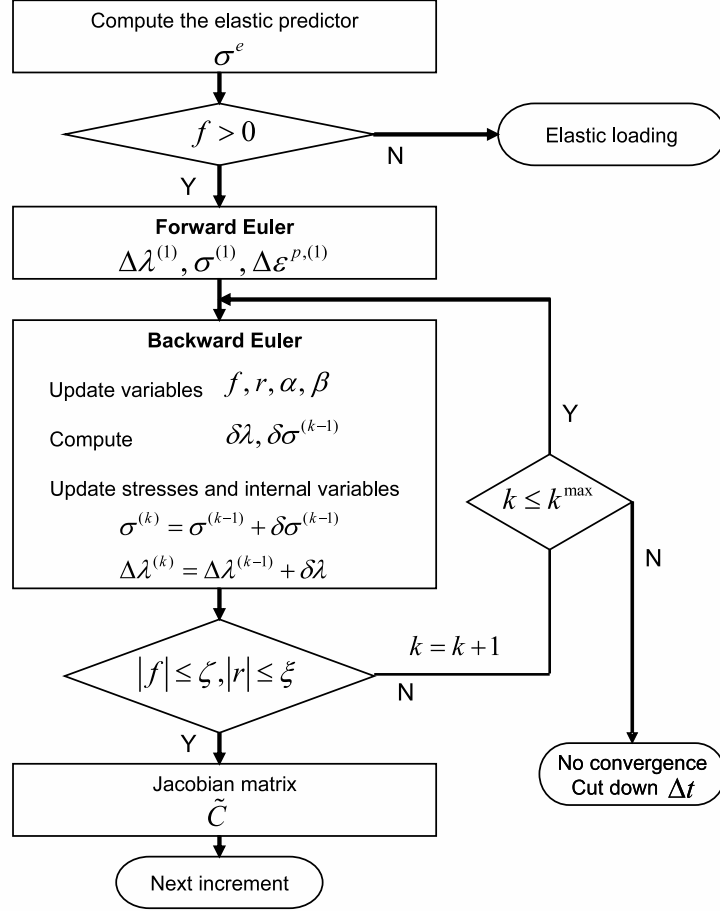
Figure 6.3: Flow chart of the integration scheme for elasto-plastic loading.

of the consistency equation, we have

$$\delta\lambda = \frac{\boldsymbol{\alpha}^{\mathrm{T}} \cdot \mathbf{R} \cdot \mathbf{C}^{e} \cdot \boldsymbol{\delta\varepsilon}}{\boldsymbol{\alpha}^{\mathrm{T}} \cdot \mathbf{R} \cdot \mathbf{C}^{e} \cdot \mathbf{Q} \cdot \boldsymbol{\beta} + A} \; . \tag{6.33}$$

Combining Eqs. (6.31) and (6.33), we obtain the Jacobian matrix as

$$\tilde{\mathbf{C}} = \frac{\boldsymbol{\delta\sigma}}{\boldsymbol{\delta\varepsilon}} = \mathbf{R} \cdot \mathbf{C}^{e} \cdot \left[\mathbf{I} - \mathbf{Q} \cdot \boldsymbol{\beta} \cdot \frac{\boldsymbol{\alpha}^{\mathrm{T}} \cdot \mathbf{R} \cdot \mathbf{C}^{e}}{\boldsymbol{\alpha}^{\mathrm{T}} \cdot \mathbf{R} \cdot \mathbf{C}^{e} \cdot \mathbf{Q} \cdot \boldsymbol{\beta} + A} \right] \; . \tag{6.34}$$

This relation providing the consistent tangents can be easily implemented in the user-defined material routine, and the internal variables and stresses in Eqn. (6.34) can be calculated at the end of the time increment.

For the Drucker-Prager-Cap model introduced in Chapter 4, we have implemented this integration scheme of elasto-plasticity in a UMAT routine in ABAQUS. By the same framework, it is also possible to transfer the current user-defined material routine into other finite element codes. One remark has to be made that during the implementations of both the integration scheme for plasticity and the stiffness matrix, it is better to provide equations in analytical forms as much as possible to reduce accumulative errors during calculation, rather than to use numerical differentiations.

6.4 Other material properties

In this section, the implementations of creep behaviour and thermo-mechanical interactions by user-defined material routines are discussed. Modifications to the Drucker-Prager-Cap model are made based on the consolidation creep mechanism. The procedures will be introduced briefly, with emphasis on the thermo-mechanical behaviour of pebble beds in fusion blankets.

6.4.1 Creep properties

The implementation of creep behaviour is realized as follows: first, at the beginning of each time increment, the creep strains are calculated with respect to the current stress state $\boldsymbol{\sigma}_{(n)}$ and time increment $\Delta t_{(n+1)}$. Second, the elasto-plastic calculation starts, considering the creep strains as a part of the inelastic strains. Thus the deformation gradient $\mathbf{F}$ can be decomposed into the creep and elasto-plastic parts as

$$\mathbf{F} = \mathbf{F}^{ep} \cdot \mathbf{F}^{cr} . \tag{6.35}$$

This decomposition means that any deformation can be split locally into a creep deformation, which is followed by an elasto-plastic deformation. The additive form, $\boldsymbol{\varepsilon} = \boldsymbol{\varepsilon}^{ep} + \boldsymbol{\varepsilon}^{cr}$, can be used for infinitesimal strains. For most cases in thermo-mechanical analyses of pebble beds, the creep deformation starts while temperature and loading stay nearly constant. If changes of the stresses in each step are sufficiently small during a given time increment, this method is valid.

For representing creep procedures of pebble beds, the consolidation creep potential, Eqn. (4.30), is modified in the following way as

$$G_c^{cr} = \sqrt{p^2 + (R\,q)^2} . \tag{6.36}$$

As discussed in Section 4.3, by changing the consolidation creep potential, the "no creep region" is removed, and the difference between Eqn. (6.36) and the default form in ABAQUS is schematically drawn in Figure 6.4. As long as the stress state locates inside the "no creep region", the default creep potential in ABAQUS would give an opposite and unrealistic direction of creep strain increments. Therefore, the driving force $\bar{p}^{cr} = p - p_a$ is set by default to zero in this region, and this can not be modified even by using a "CREEP" subroutine. The discussion in Chapter 4 showed that due to the existence of this "no creep region", neither the large creep strain nor the hardening by the creep strains can be represented in a satisfying way by the default form. After all, they are two typical experimentally observed phenomena, which may exist at the same time in the pebble beds under fusion-relevant conditions. The mechanism of creep in a pebble bed includes the creep deformation of the bulk material and rearrangement of pebbles, both of which can introduce hardening effects on the material. The active creep region in the present implementation is inside the whole yield/failure surface, instead of having an initial pressure (p_a), like the vertical dashed line in Figure 6.4.

With this modified creep potential, the creep strain increments can be calculated by

$$\Delta \boldsymbol{\varepsilon}^{cr} = \Delta \lambda \frac{\partial G_c^{cr}}{\partial \boldsymbol{\sigma}} . \tag{6.37}$$

For the case of volumetric creep, the coefficient $\Delta \lambda$ can be obtained as

$$\Delta \lambda = \Delta \varepsilon_{vol}^{cr} \Big/ \left(\frac{\partial G_c^{cr}}{\partial \sigma_{ii}} \right) . \tag{6.38}$$
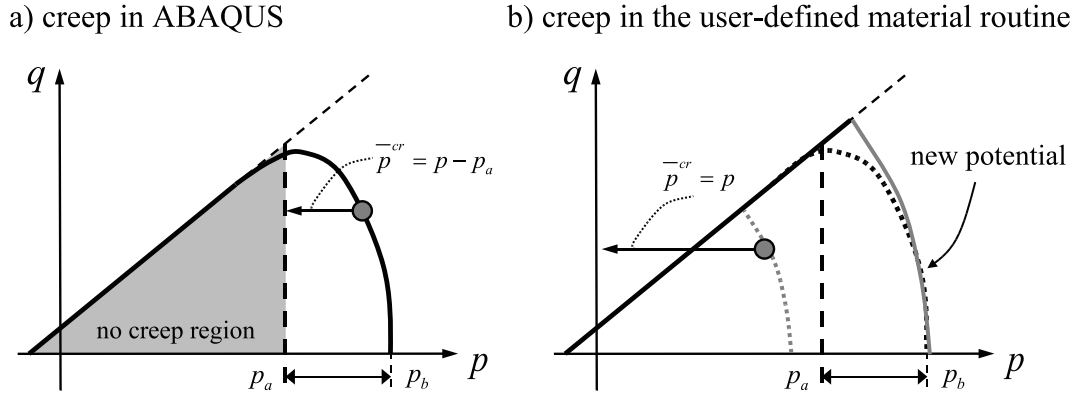
Figure 6.4: Modification of the creep potential in the user-defined material routine.

According to the above discussion, the consolidation creep procedure has also been implemented in the UMAT routine in ABAQUS.

6.4.2 Thermo-mechanical behaviour

The coefficient of thermal expansion can be directly implemented in the UMAT routine as well. On the other hand, for the definition of thermal conductivity and specific heat, another routine, called UMATHT (user-defined material's thermal behaviour), should be used in addition to a UMAT routine in ABAQUS.

These implementations are straightforward from the experimental data. A special feature of the effective thermal conductivity of pebble beds is the dependence not only on temperature but also on the inelastic volumetric strain in this investigation. Therefore, information concerning the thermo-mechanical coupling has to be passed between these two routines.

6.5 Verification

As discussed above, the phenomenological model introduced in Chapter 4 has been implemented in ABAQUS by both UMAT and UMATHT routines. The verification is presented in this section. We take the database for the reference Li_4SiO_4 and beryllium pebble beds provided by Fokkens (2003), where the coefficients for both uniaxial compression tests and creep experiments (Reimann and Worner, 2001; Reimann and Harsch, 2004) are provided.

Simulations for uniaxial compression and creep tests have been carried out by a single finite element (CAX8RT element in ABAQUS). Figure 6.5 shows the comparison between the predictions by the present user-defined material routine and experimental data. Figures 6.5-(a) and (b) show the uniaxial compression tests at room temperature for Li_4SiO_4 and beryllium pebble beds, respectively. In uniaxial compression tests, the material parameters are identified from the empirical curves with the method proposed in Chapter 5. The maximum compressive stress reaches 6 MPa. Good agreements are found in both loading and unloading branches.

The creep experiments of both Li_4SiO_4 and beryllium pebble beds are compared with the predictions in Figure 6.5-(c) and (d), respectively. The material parameters (A^*, B, m, n) in Eqn. (4.33) can be identified by the method in Chapter 5 from the experimental coefficients (A, B, m, n) as well. The hydrostatic pressure p is used here as the driving force for creep, while in the empirical curves the pressure σ_y is employed. A factor α^{cr} is thus used to adjust the difference between experimental data and predictions, for instance, $A^* = \alpha^{cr}A$. For Li_4SiO_4, $\alpha^{cr} = 0.45$, and for beryllium pebble beds, $\alpha^{cr} = 0.48$ gives the best fit to the experimental data. These values are different from the ones mentioned in Section 5.2.2, since the creep potential has been modified according to Eqn. (6.36). For each material, two different conditions have been carried out: for Li_4SiO_4, (1) 6.5 MPa and 650 ^oC as well as (2) 2.2 MPa and 850 ^oC; and for beryllium pebble beds, (1) 3.5 MPa and 500 ^oC as well as (2) 1.7 MPa and 650 ^oC. The prediction consists well with the experimental data.

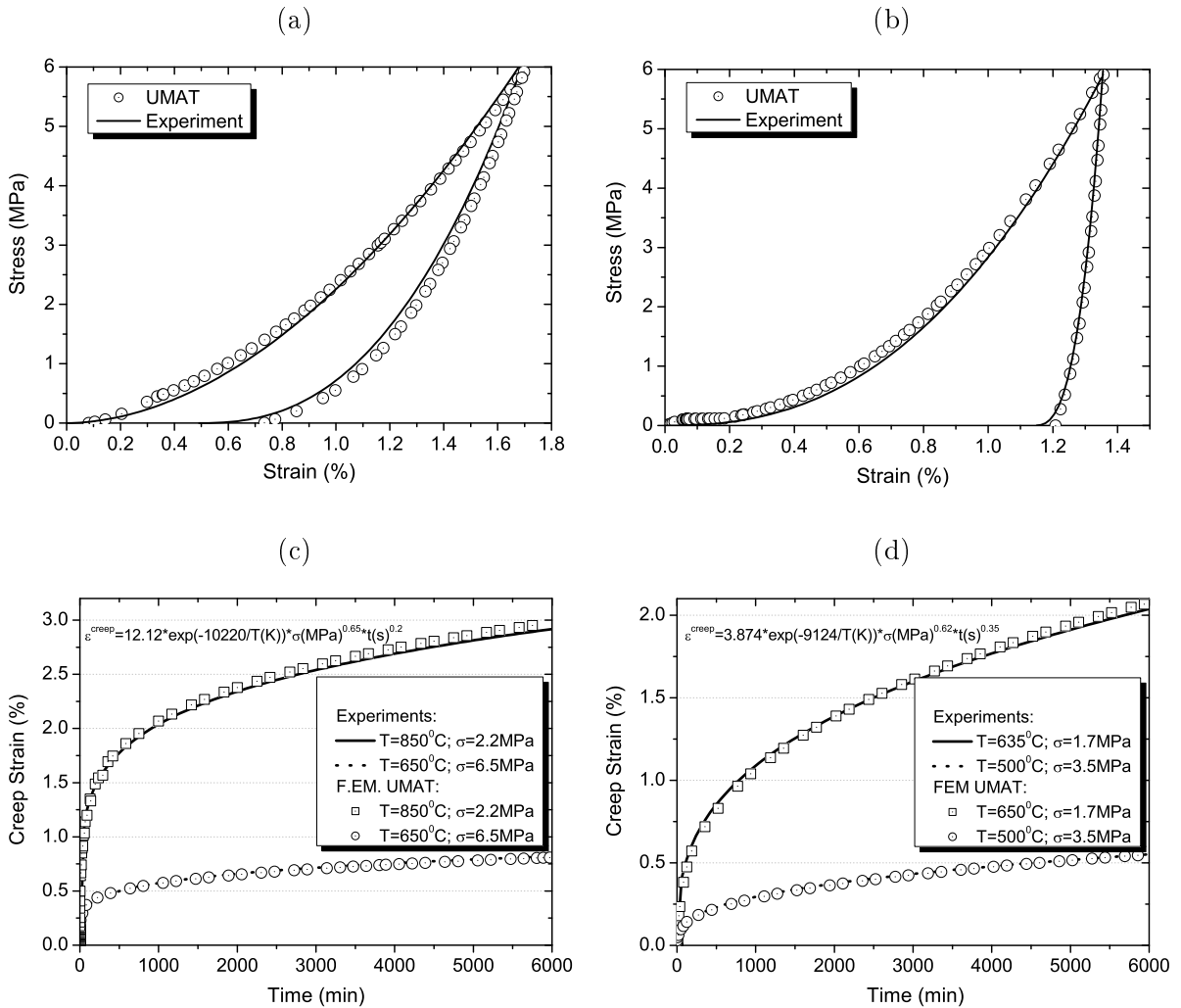Figure 6.5: Validation of the user-defined material routine, including UCT of (a) Li_4SiO_4 and (b) beryllium, and creep experiments of (c) Li_4SiO_4 and (d) beryllium pebble beds.

The verifications show that the present implementation of the material model has been successful for ceramic breeder and neutron multiplier pebble beds.

6.6 Summary

In this chapter, user-defined material routines are introduced to implement the phenomeno-
logical model into a finite element code. The material properties include nonlinear elasticity,
time-independent plasticity with non-associated plastic flow, creep and thermo-mechanical in-
teractions. The update scheme for stresses and internal variables, and the Jacobian matrix with
respect to the incremental strain history are two important issues in a user-defined material
routine.

The return mapping algorithm is adopted as the integration scheme for elasto-plasticity. The
elasto-plastic consistent tangents are given at the end of each time increment. Based on the
Drucker-Pager-Cap theory, we have re-implemented these material properties into UMAT and
UMATHT routines in ABAQUS. We also changed the consolidation creep potential to overcome
the limitations of the default form in ABAQUS. Other material properties, which are essential to
perform fully coupled thermo-mechanical analyses of pebble beds, have also been implemented.
Verifications have been made for both the uniaxial compression tests and creep experiments.
This work also provides the possibility to implement other relevant material models for pebble
beds.

Chapter 7

Thermo-Mechanical Modelling of Interfaces

With the phenomenological model of pebble beds discussed in previous chapters, structures containing pebble beds, such as HCPB blankets, are possible to be analyzed using coupled thermo-mechanical finite element codes. But before the material model is employed into engineering applications, the interfacial behaviour of interactions between the pebble bed and container wall has to be investigated. The interfacial behaviour is important in thermo-mechanical analyses since it provides boundary conditions for the bulk region of the pebble bed, in terms of both temperature and displacement.

The pebble-wall interactions can be split into two categories: (1) mechanical interactions; and (2) the interfacial heat transfer. For mechanical interactions, the interfacial contact and friction forces can be taken into account in the finite element code by a frictional contact law, such as the Coulomb friction law, without too much effort on considering the microstructure of pebble beds. However, for the heat transfer coefficient (HTC) between the contacting parts it needs special emphasis. The HTC depends on the properties of the bulk materials, overall properties of the pebble bed, as well as the temperature and mechanical fields near the interface.

In this chapter, after the review of available experiments and models, the interfacial heat transfer is investigated theoretically, taking into account the mechanical contributions. Then the prediction of the model is compared to the experimental data, and some discussions are made.

7.1   Available experiments and models

7.1.1   Experiments

Experimental investigations on heat transfer coefficients for pebble-wall interfaces have been carried out by different researchers. Dalle Donne and Sordon (1990) have performed experiments for the interface between a Li_4SiO_4 pebble bed and stainless steel container. The ceramic pebbles have an average diameter of 0.5 mm and a packing factor of 61.9%. Tehranian et al. (1994) and Tehranian and Abdou (1995) have studied different types of pebble beds contacting with stainless steel, including aluminium pebbles with a diameter of 0.8 mm and packing factor of 63%, and

Li$_2$ZrO$_3$ (lithium zirconate) pebbles with an average diameter of 1.2 mm and packing factor of 65-69%. The purge gas consisted of either air or helium at different pressures. Mechanical load has been taken into account in their work, but the average bed temperature is comparably low. For beryllium pebble beds, interfaces have been investigated experimentally by Dalle Donne et al. (2000) and Abou-Sena et al. (2003). The first type of the experiments for the interfaces between beryllium pebble bed and container wall has been carried out in a stainless steel container, and beryllium pebbles had a diameter of 2 mm and two kinds of packing factors, namely, 60% and 63% (Dalle Donne et al., 2000). Due to the experimental setup, it was not easy to separate the influences of temperature and mechanical loads. Recently, Abou-Sena et al. (2003) have studied the interfacial heat transfer of a beryllium pebble bed (d=2 mm, PF=60.6%) in contact with a layer of silicon carbide (SiC), including the dependence on both the bed temperature and the compressive stresses.

In the above experiments, the basic strategy is to extrapolate the temperature measurements on thermo-couples, located inside the pebble bed, to the pebble-wall interface as T_b, and meanwhile measure the wall temperature T_w. Knowing the surface heat flux q via the interface, the HTC can be expressed as

$$h = \frac{q}{T_b - T_w} \ .$$
(7.1)

However, inaccuracy of the measurements is introduced by different factors, such as variations of errors on the thermo-couples. Another important fact is that the temperature drop through the pebble-wall interface is comparably small, due to the limitation of the heat supply in the experiments. Therefore, the measurements of HTC vary in a wide range of magnitudes (Dalle Donne and Sordon, 1990). A theoretical model of the interfacial heat transfer is essential to understand the pebble-wall interactions.

7.1.2 Models

Models of interfacial heat transfer have been proposed mainly for a packed bed in contact with a flat surface, rather than for the specific case of the interfaces between pebble beds and wall under fusion-relevant conditions. The latter case includes some specific features, such as using high temperature helium as interstitial gas and having a low solid-to-gas conductivity ratio. But the basic notion of these models can be utilized in this investigation.

Among the existing interfacial models, a unit cell is commonly used to study the case of the thermal contact conductance of a single spherical particle-wall interaction. The interfacial heat transfer can be separated into different mechanisms, such as the one in the solid-gas and the solid-solid region. Different assumptions have been made about the temperature distribution inside the unit cell, e.g., temperatures at the surfaces of the bulk materials can be assumed to be either uniform (Schlünder, 1982) or non-uniform (McGee et al., 1985). The heat transfer through the interstitial gas gap has been mostly concerned (Schlünder, 1982), while recent models consider not only the contact between pebble and wall, but also the influence of wall materials (Kikuchi, 2001). In most cases, a parallel heat transfer has been assumed in the solid-gas region. For the solid-solid contact region, Peterson and Fletcher (1988) have studied the interface in vacuum, and compared the model with experiments. Gorbis et al. (1995) have proposed a model using the near-wall conductivity, considering both solid-gas and solid-solid regions. Except for the work of Kikuchi (2001), the wall effects have not been considered in literature. However, it

would be an issue if the wall material has a lower thermal conductivity than the bulk material of pebbles, such as in the case of the interface between beryllium pebble beds and the stainless steel container. For applications in fusion blankets, Reimann et al. (2005a) have investigated the pebble-wall interactions of ceramic and beryllium pebble beds based on Schlünder's model, and this model has been proposed to be the reference database for pebble beds. Nevertheless, the solid-solid contact region and wall effects have not been taken into account in this model.

Finally, an averaging method is applied to transfer the results from the microscopic study into a phenomenological model. In this way, the HTC model can be combined with a finite element code as shown in Figure 7.1. The HTC model needs the definitions of the contacting materials from the material database, i.e. material properties with respect to temperature, and state variables from the finite element analysis, such as temperature, strains and stresses. On the other hand, the finite element code needs the HTC value as an input for predicting the current temperature distribution. These procedures are coupled, but an explicit scheme can be adopted in each increment with an adequate time step, e.g., calculating the HTC value with the state variables at the beginning of the time step, and then providing thermal boundary conditions for the finite element code.
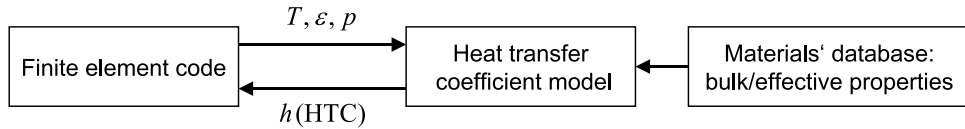

Figure 7.1: Interface between the HTC model and a finite element code.

7.2   Modelling of interfacial heat transfer

For the heat transfer between two surfaces, the definition of the thermal contact conductance (TCC) of the interface is

$$h = \frac{q}{\Delta T} \, , \tag{7.2}$$

where q is the surface heat flux through the interface and ΔT is the additional temperature drop due to the presence of the imperfect joint. In this work, this concept can be directly employed into the investigation of the pebble-wall interaction.

Here, we focus on pebble-wall interfaces, i.e. interfaces between pebble bed and container wall. Perpendicular to the interface between the near-wall pebbles and the container wall, there is an area of A containing N contact zones (see Figure 7.2). These contacting pebbles have a radius of R, projected onto the interface as dashed circles, and the average radius of the contact zones is a. These contact areas could be assumed to have the same temperature as the contacting pebbles, and they seem to be "hot spots" on the wall if the heat is transferred from the pebbles to the wall region.

In order to obtain the HTC value of the interface, we have to take into account the density of the contact zones. Here, we use the parameter

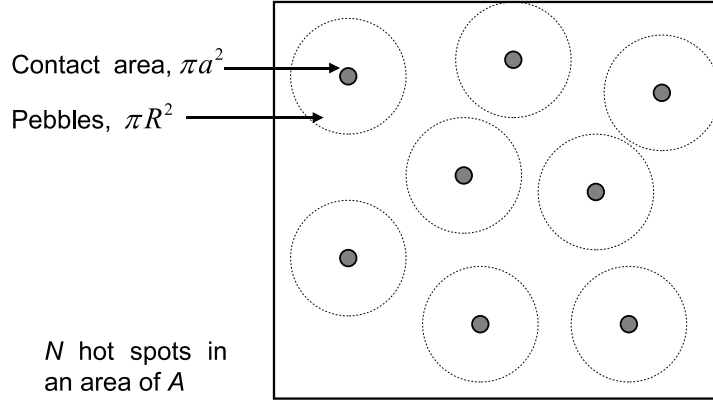$$L = \left(\frac{A}{\pi N}\right)^{0.5} \, , \tag{7.3}$$

Figure 7.2: Multiple "hot spots" model for the thermal contact conductance.

depending on the near-wall packing structure, which can be either a regular or a random packing of pebbles. To estimate the value of parameter L, we assume that the pebbles are packed regularly. Thus for the (001)-direction of a FCC packing, the typical value of L/R is $4/\pi$; and for the (001)-direction of a BCC packing, it is $16/3\pi$.

Considering the condition of axisymmetry, a basic unit cell can be sketched as in Figure 7.3-(a). This is a microscopic side view of each contact zone, and includes the regions of the wall, pebble and interstitial gas. The pebble has a radius of R, and the unit cell has a thickness of $2R$. The radius of the unit cell is L, depending on the topology of the packed pebbles near the wall, as defined in Eqn. (7.3). We use $L = 4R/\pi$ in this unit cell.

The temperature distribution along the direction perpendicular to the interface, representing the temperature averaged in r-direction at each cross-section, is schematically drawn in Figure 7.3-(b). The two temperature values at the upper and lower boundaries of the unit cell, denoted as T_1 and T_0, respectively, are connected by a solid curve as the actual temperature distribution. Two dashed lines indicate the temperature distributions extrapolated by the thermal conductivity of wall material, k_w, and the effective thermal conductivity of the pebble bed, k_{eff}, respectively. The temperature difference ΔT_C at the interface is calculated by the difference of these two extrapolated temperatures, and it is the additional temperature drop due to the presence of the interface. If Q is the total heat flow through the unit cell, then the heat transfer coefficient can be expressed as

$$h = \frac{Q}{\pi L^2 \, \Delta T_C} = \frac{q}{\Delta T_C} \ . \tag{7.4}$$

In principle, the heat transfer via an interface occurs by a combination of four different modes: conduction through the pebble-wall contacts, conduction through the interstitial gas, convection in the interstitial gas region, and thermal radiation. Researchers (Lang, 1962) have pointed out that the convection mode is usually negligible for gap widths of up to 6 mm (corresponding to a Grashof number of 2000 for air at atmospheric pressure of 101 kPa and a temperature of 300 K). A similar conclusion has been made by Yagi and Kunii (1960). In the case of helium being the interstitial purge gas, as in fusion blankets, the convection mode is hence negligible.

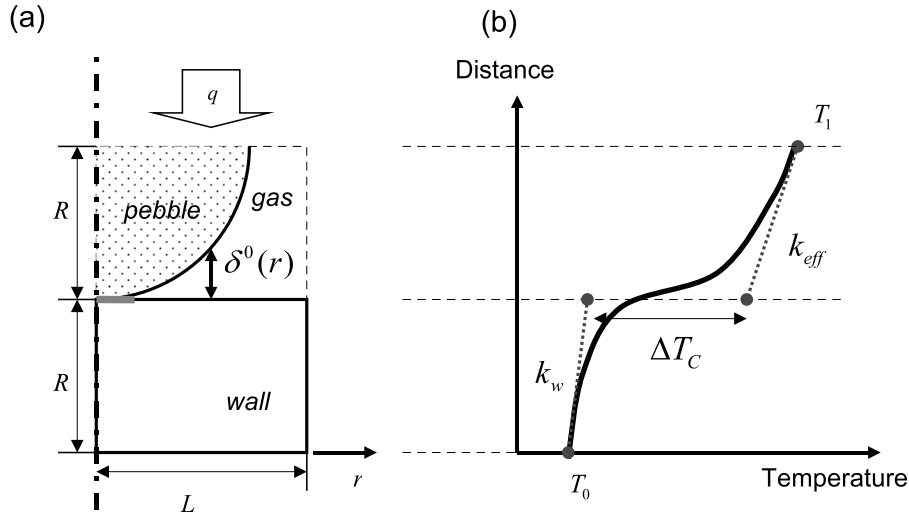We separate heat flux q through the unit cell into three main mechanisms in Figure 7.4: (a) q_c,

Figure 7.3: (a) The unit cell of the HTC model; (b) the temperature distribution.

heat transfer through the solid-solid contact; (b) q_g, through the gas gap; and (c) q_r, by thermal radiation. Thus, these types of heat flux fulfill the condition

$$q = q_c + q_g + g_r \ . \tag{7.5}$$

In Figure 7.4, the notations, k_{eff}, k_p, k_w and k_g, indicate the effective thermal conductivity of pebble beds, thermal conductivities of the bulk material of pebbles, wall material and interstitial gas, respectively.
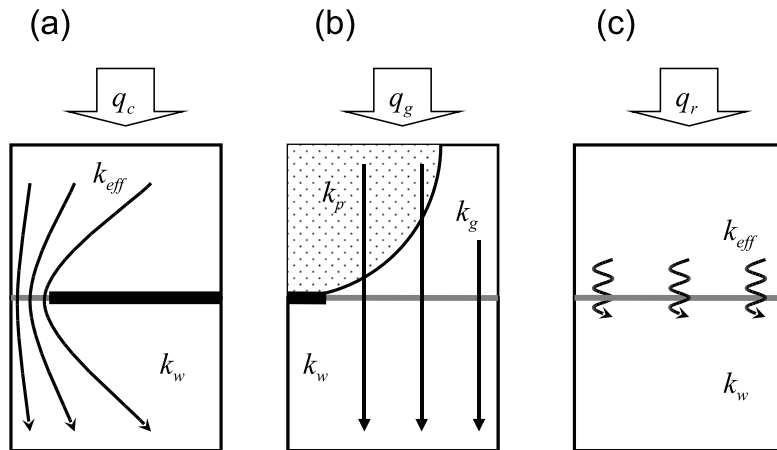
Figure 7.4: Three mechanisms of heat transfer in the unit cell.

Since the equations of thermal conduction have a similar form as Ohm's law, these types of thermal conduction can be summed in the same manner as serial and parallel electrical conductors. The electrical analog of the problem considered here can be sketched as in Figure 7.5. Inside each mechanism, the thermal resistors are in series, while for the three different mechanisms, these overall resistors are in parallel. Therefore, the objective of this analysis is to find the

solution of the interfacial heat transfer coefficient h_0 in the relation

$$\sum_{i=c,g,r} \left(\frac{R}{k_{\mathrm{eff}}} + \frac{1}{h_i} + \frac{R}{k_w}\right)^{-1} = \left(\frac{R}{k_{\mathrm{eff}}} + \frac{1}{h_0} + \frac{R}{k_w}\right)^{-1} . \qquad (7.6)$$

In the following section, analyses of the different mechanisms are made. Based on Eqn. (7.6), the heat transfer coefficient of the interface, h_0, can be obtained.
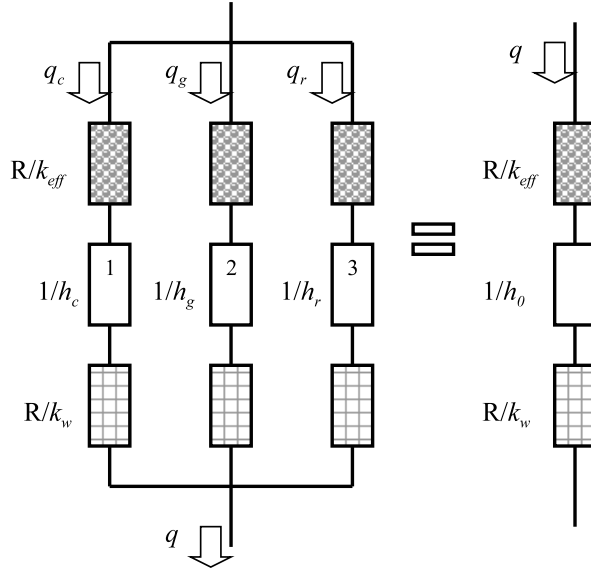

Figure 7.5: Electrical analog of thermal conductances in Figure 7.4.

7.3 Analysis of the unit cell

In this section, three different mechanisms are analyzed separately, by which the overall behaviour of the unit cell can be obtained. We assume that the heat transfer through each pebble-wall unit cell at the interface is identical. Therefore, the phenomenological heat transfer coefficient is directly obtained from the unit cell.

7.3.1 Solid-solid region

The first mechanism of the interfacial heat transfer is conduction via the pebble-wall contact in the unit cell. To solve the problem analytically, the change of the mechanical field with respect to the compressive stress present at the interface, p_n, has to be taken into account. If the interface has a surface normal $\mathbf{n}$, $p_n = \boldsymbol{\sigma} \cdot \mathbf{n}$. According to the Hertzian solution (Johnson, 1985), we have the following relation between the radius of the contact zone and the contact force $P = p_n(\pi L^2)$

$$a = \left[\frac{3}{4}\pi P(K_p + K_w)R\right]^{1/3} , \qquad (7.7)$$

where K_p and K_w depend on the elastic moduli of the bulk materials, as $K_i = (1 - \nu_i^2)/\pi E_i$ with $i = p, w$.

In the solid-solid region, Madhusudana (1995) has provided a solution for the thermal conductance of the solid spot contact as a function of the contact area as

$$h_c = \frac{2ak}{\pi L^2} \ . \tag{7.8}$$

Here, $k = 2k_w k_p/(k_w + k_p)$ is the harmonic mean of the bulk thermal conductivities of wall and pebble, and a is the radius of the contact spot in Eqn. (7.7).

Peterson and Fletcher (1988) have investigated the interfacial heat transfer in vacuum experimentally, which results in the summation of the contributions of solid-solid contacts and thermal radiation. The analytical result of the solid contact conductance fits well with the experiments, since the contribution of thermal radiation is relatively small.

7.3.2 Solid-gas region

As shown in Figure 7.3-(a), the distance between the two surfaces at the same radial position r can be expressed as

$$\delta^0(r) = \left\{ \begin{array}{ll} R - \sqrt{R^2 - r^2}, & r < R \ , \\ R, & L \geq r \geq R \ . \end{array} \right. \tag{7.9}$$

This expression is valid while the bulk materials of pebble and wall are hard materials, and thus the gap reduction due to compressive stresses is negligible over a certain range of the mechanical load. Otherwise, the gap reduction can be taken into account by the relative displacement between the contacted surfaces.

To study the heat transfer via a interstitial gas gap, general properties of the gas gap are first shown here. For the gas gap, the thermal conductivity in the microscopic region near the solid surface is decreased by the Smoluchowski effect. This effect accounts for the inefficiency in energy exchanges between gas molecules and solid surfaces during single collisions (Madhusudana, 1995). Thus, the thermal conductivity of a gas gap with a width of $\delta^0(r)$ reads as

$$k_g(r) = \frac{k_{g,\infty}}{1 + (\Delta + j)/\delta^0(r)} \ , \tag{7.10}$$

where $k_{g,\infty}$ is the thermal conductivity of gas without the effect of solid-gas interfaces and Δ is the summation of surface roughness. The coefficient j is the temperature jump distance, taking into account the Smoluchowski effect. In a sufficiently large gas gap, the Smoluchowski effect vanishes. The temperature jump distance can be expressed as

$$j = \Big(\sum_i \frac{2 - \alpha_i}{\alpha_i} \Big) \frac{2\gamma}{\gamma + 1} \frac{\lambda}{Pr} \ , \tag{7.11}$$

where α_i denotes the accommodation coefficient of the interstitial gas on the corresponding surface, γ is the ratio of specific heats, λ is the mean free path of gas molecules and Pr is the Prandlt number. The mean free path λ_g of gas molecules at temperature T_g and pressure p_g has the relation

$$\lambda_g = \lambda_0 \Big(\frac{T_g}{T_0} \Big) \Big(\frac{p_0}{p_g} \Big) \ , \tag{7.12}$$

to the one λ_0 at temperature T_0 and pressure p_0. It has been suggested by Song and Yovanovich (1987) that the accommodation coefficient $\alpha = 0.4$ can be used in most engineering surfaces to give a reasonable approximation.

For the heat transfer via the gas gap, as illustrated in Figure 7.4-(b), the overall heat conductance $h^{(b)}$ is

$$h^{(b)} = \left(\frac{R}{k_{\text{eff}}} + \frac{1}{h_g} + \frac{R}{k_w} \right)^{-1} . \tag{7.13}$$

In this region, $h^{(b)}$ can be directly obtained from the analysis of the unit cell, instead of calculating h_g.

In the solid-gas region, different assumptions for the heat transfer can be made. The interstitial gas gap has been studied under the following assumptions by Schlünder (1982): (1) the temperature on each surface is uniform; (2) the temperature difference between two different surfaces is the additional temperature drop ΔT_C of the unit cell; and (3) the heat flow is one dimensional. This gives the heat transfer coefficient as

$$h^{(b)} = \frac{1}{\pi L^2} \int_a^L \frac{k_g(r)}{\delta^0(r)} 2\pi r \, \mathrm{d}r . \tag{7.14}$$

It is valid while $k_g \ll k_p$ and $k_g \ll k_w$. This expression can be used for packed beds and gives reasonable results, although assumptions have been made that all contacts are point-wise and the surfaces have zero roughness (Schlünder, 1982). In other words, this model does not separate the effects of the solid-solid and solid-gas regions. Thus, the model can give an overestimation if we only consider the solid-gas region.

Alternatively, the heat transfer can be assumed to follow parallel heat pipes from the top to the bottom of the unit cell (McGee et al., 1985). Compared with the assumptions made by Schlünder (1982), assumption (1) has been released, so the temperature distributions on the surfaces can be position-dependent; assumption (2) is irrelevant in this case; assumption (3) remains and the parallel heat transfer is also assumed in this case. This model considers the effects of both the wall and the bulk region of pebbles. The corresponding heat transfer coefficient in the solid-gas region is

$$h^{(b)} = \frac{1}{\pi L^2} \int_a^L \frac{1}{\frac{R - \delta^0(r)}{k_p} + \frac{\delta^0(r)}{k_g(r)} + \frac{R}{k_w}} 2\pi r \, \mathrm{d}r . \tag{7.15}$$

Both types of assumptions give comparable predictions of the heat transfer coefficient, while the value obtained by the second one is smaller, especially for materials with a low solid-to-gas conductivity ratio. Therefore, for ceramic breeder pebble beds, the Schlünder model usually gives an overestimation. In this investigation, we use the second type of modelling for the solid-gas region.

7.3.3 Radiation effect

For thermal radiation, the heat transfer coefficient depends on the mean temperature of the interface, T_i, as

$$h_r = 4 \frac{C_s}{1/\epsilon_w + 1/\epsilon_p - 1} T_i^3 \tag{7.16}$$

where C_s is the Stefan-Boltzman constant ($5.67 \times 10^{-8} W/m^2 K^4$), ϵ_w is the emissivity of the wall, and ϵ_p is the emissivity of pebble bed. Figure 7.6 shows the radiation effects as a function of temperature, with different values of emissivity. In this investigation, we use $\epsilon_w = \epsilon_p = 0.5$. The radiation effect will be negligible in the low temperature region, which can also be found in Peterson and Fletcher's experiments.
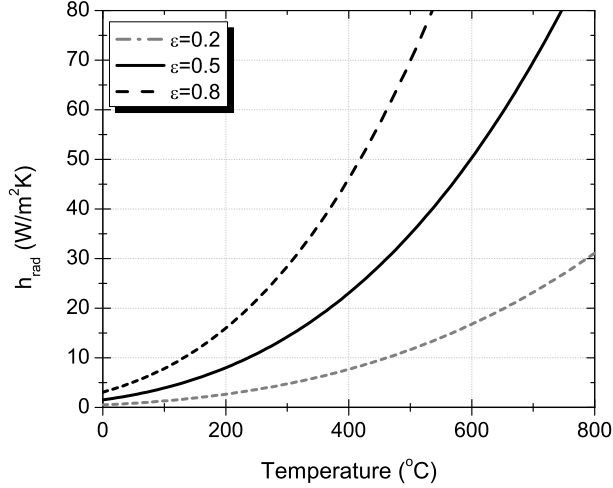
Figure 7.6: Radiation effect as a function of temperature.

7.3.4 Overall behaviour

Substituting the solutions of h_c, h_g (or $h^{(b)}$) and h_r into Eqn. (7.6), we can solve for the value of h_0. This solution represents the dependence on the temperature, gas pressure and mechanical field. By implementing this relation into the finite element code, the heat transfer coefficient can be realized into the fully coupled thermo-mechanical analysis.

7.4 Comparison with the experiments

The heat transfer coefficient depends on the additional temperature drop ΔT_C at the interface, which is typically small and not easy to be measured in experiments. Only a few related measurements are available for Li_4SiO_4 and beryllium pebble beds in literature (Dalle Donne and Sordon, 1990; Dalle Donne et al., 2000; Abou-Sena et al., 2003). In this section, we compare the prediction of the theoretical model with the available experimental data.

7.4.1 Material parameters

For the present HTC model, the material properties are required for the purpose of validation. The temperature dependence of the bulk material properties is not taken into account to simplify the prediction in this investigation, since the effect is moderate. Therefore, the temperature dependence of the heat transfer coefficient is dominated by the interstitial gas phase in this investigation.

Table 7.1 shows the properties of the bulk materials used in this investigation.[1] Table 7.2 shows the parameters for the gas gap thermal conductivity, and here helium is chosen as the interstitial purge gas. The surface roughness (Δ) of these materials is set to 5 μm. The effective thermal conductivities of pebble beds are listed in Table 7.3. These measurements have been made in the

---

[1]Data from *Fusion Network*: `http://fusionnet.seas.ucla.edu/fusionnetwork/index.php`

corresponding experiments to obtain heat transfer coefficients. The reference effective thermal conductivities can be found in Chapter 4 for both Li_4SiO_4 and beryllium pebble beds.

Table 7.1: Properties of bulk materials for heat transfer coefficients

Bulk material	Thermal conductivity (W/mK)	Young's modulus (GPa)	Poisson's ratio
Beryllium	176.95	287	0.032
Li_4SiO_4	1.42	90	0.24
Stainless Steel	14.15	196	0.30
SiC	45	450	0.21

Table 7.2: Parameters for the gas gap thermal conductivity

Thermal conductivity $k_{g,\infty}(W/mK)$	$3.623 \times 10^{-3} \times T(K)^{0.66}$
Ratio of specific heats γ	1.66
Prandtl number Pr	0.67
Accommodation coefficient α	0.4
Mean free path of gas molecules λ (nm)	0.186 ($T_0 = 300K$, $p_0 = 101kPa$)

7.4.2 Comparison with available experiments

Table 7.4 shows a summary for the experimental HTC results. These related experimental investigations can be classified into three types according to their bulk materials: (1) the Be/stainless steel interface (Dalle Donne et al., 2000); (2) the Be/SiC interface (Abou-Sena et al., 2003); and (3) the Li_4SiO_4/stainless steel interface (Dalle Donne and Sordon, 1990). The above material properties, as well as the effective thermal conductivity of pebble beds, are used as inputs to the present interfacial model.

Table 7.3: Correlations for the effective thermal conductivities of pebble beds

$k_{\text{eff}}(W/mK)$; $T_m(^oC)$ is the mean temperature of the pebble bed; d is the mean diameter of pebbles; η denotes the packing factor; and $\varepsilon(\%)$ is the compressive strain. Ref.: [1] Dalle Donne et al. (2000); [2] Abou-Sena et al. (2003); [3] Dalle Donne and Sordon (1990).

	Types	Thermal conductivity	Ref.
Be	$d = 2$ mm; $\eta = 63\%$.	$2.499 + 2.07 \cdot 10^{-3}T_m$	[1]
	$d = 2$ mm; $\eta = 60\%$.	$1.823 + 2.053 \cdot 10^{-3}T_m$	[1]
	$d = 2$ mm; $\eta = 60.6\%$.	$1.9712 + 2.2 \cdot 10^{-3}T_m$	[2]
Li_4SiO_4	$d = 0.5$ mm; $\eta = 61.9\%$.	0.736 ($T_m = 51.6$); 0.825 ($T_m = 131.6$)	[3]

(1) Be/stainless steel

Figure 7.7 shows the comparison between the present HTC model and experimental results for the Be/stainless steel interface. This type of experiments has been performed in PEHTRA

Table 7.4: Heat transfer coefficients of pebble-wall interactions

$T_w(^oC)$ is the near-wall temperature of the pebble bed. Ref.: [1] Dalle Donne et al. (2000); [2] Abou-Sena et al. (2003); [3] Dalle Donne and Sordon (1990).

	Types	HTC (W/m^2K)	Ref.
Be	$d = 2\ mm$; $\eta = 63\%$.	$369 + 0.8666T_w + 3.472 \cdot 10^{-3}T_w^2$ (Be/stainless steel)	[1]
	$d = 2\ mm$; $\eta = 60\%$.	$614.6 - 0.8867T_w + 7.899 \cdot 10^{-3}T_w^2$ (Be/stainless steel)	[1]
	$d = 2\ mm$; $\eta = 60.6\%$.	data points (Be/SiC)	[2]
Li_4SiO_4	$d = 0.5\ mm$; $\eta = 61.9\%$.	data points (Li_4SiO_4/stainless steel)	[3]

(Dalle Donne et al., 2000), with a cylinder container and a rod heater located in the center. It is difficult to control the thermal stresses induced by the temperature changing. Therefore, the heat conductance at high temperatures increases due to not only the changing thermal conductivity of the interstitial gas with respect to temperature, but also due to the induced compressive stresses at the interface. A small increase of the compressive stresses can introduce notable changes on the value of the HTC, since beryllium has a relatively high thermal conductivity. Although the model overestimates the value at low temperatures, it still gives reasonable predictions, including the temperature dependence and the difference between the two cases with different packing factors.
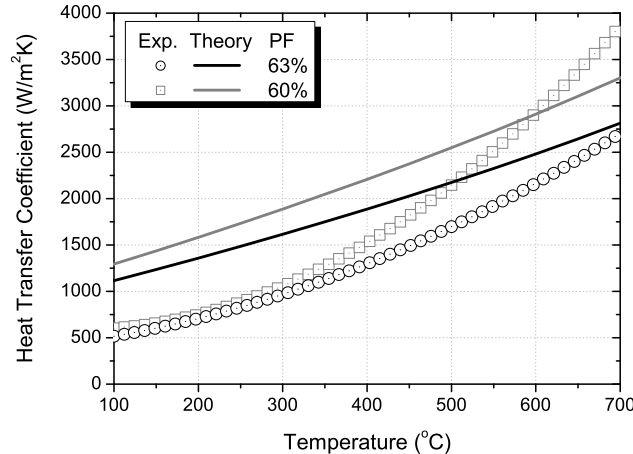
Figure 7.7: Comparison of the HTC model with data from Dalle Donne et al. (2000): the Be/stainless steel interface.

(2) Be/SiC

For the Be/SiC interface, the comparison between the predictions and experiments can be found in Figure 7.8. Abou-Sena et al. (2003) have performed a series of measurements to investigate: (i) the dependence on the mean bed temperature, and (ii) the dependence on the pressure at a fixed bed temperature. Figure 7.8-(a) shows that the HTC changes over the mean bed temperature, from room temperature to 450 ^oC. In Figure 7.8-(b), the pressure varies from 0 to 2 MPa at a mean bed temperature of 270 ^oC. The prediction shows a clear increment with respect to the

mechanical pressure. An overestimation of the theoretical model is also found in this case.
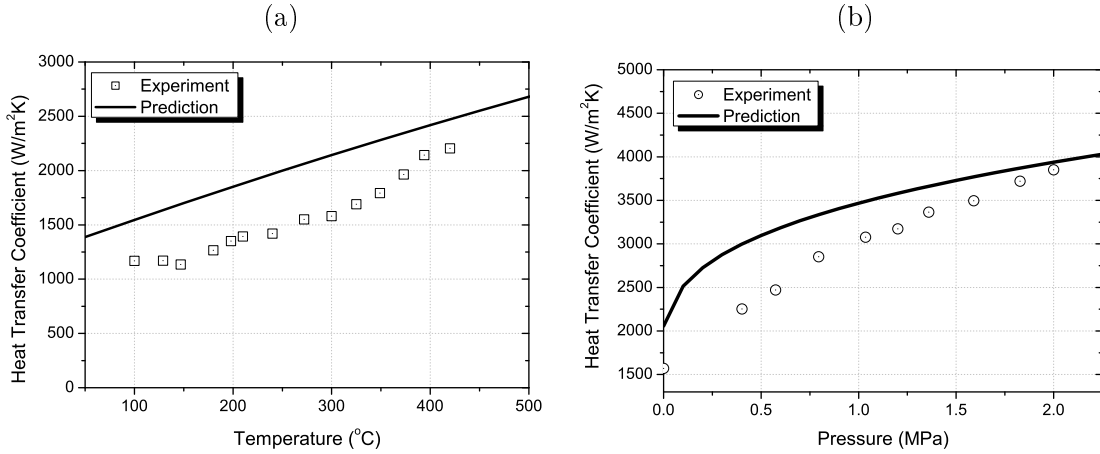

Figure 7.8: Comparison of the HTC model with data from Abou-Sena et al. (2003): the Be/SiC interface. HTC over: (a) the mean bed temperature; (b) the compressive stresses ($T_m = 270^oC$).

(3) Li_4SiO_4/stainless steel

The available experimental data are limited in the case of the Li_4SiO_4/stainless steel interface (Dalle Donne and Sordon, 1990). The cylinder container with a heater rod in its center has also been used here. Two data points have been measured near the heater side (the inner wall) and the others near the coolant side (the outer wall). Figure 7.9 shows the comparison between the model and measurements. It has been suggested that these data from the inner wall are more reliable, due to the presence of larger temperature drops (Dalle Donne and Sordon, 1990). The outer wall has smaller temperature drops, and thus the HTC is difficult to be determined there. The level of the compressive stresses inside the container is not clear, and hence we use the prediction of uncompressed pebble beds, similar to the case of the Be/strainless steel interface. The HTC model here gives an underestimation of the experimental data at the heater side, and an overestimation at the coolant side.

7.5 Discussion

The differences between the prediction of the present HTC model and experimental data can be found in the previous section. Here, we will first discuss some issues concerning the accuracy of both the theoretical model and the experimental measurements.

7.5.1 Predictions and experimental measurements

One explanation for the error introduced by experiments is, as sketched in Figure 7.10-(a), the difference between the real temperature distribution (dashed-curve) and the extrapolated one (solid-line) inside a pebble bed. The additional temperature drop ΔT_C is calculated by the difference between the near-wall temperature T_n and wall temperature $T_{w,n}$, where $n = 1, 2$ indicates the position of the interface. The mean temperature of the bed is denoted by T_m. Here, we consider the effective thermal conductivity of the pebble bed to be a monotonically
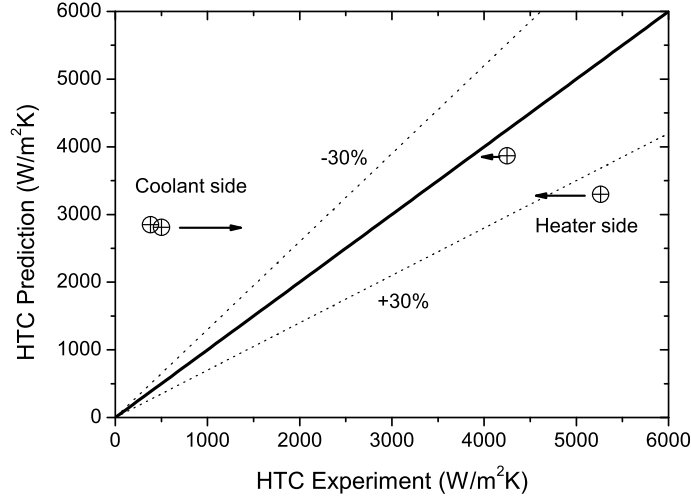
Figure 7.9: Comparison of the HTC model with data from Dalle Donne and Sordon (1990): the Li$_4$SiO$_4$/stainless steel interface.

increasing function of temperature. For the temperature distribution extrapolated by using $k_{\text{eff}}(T_m)$, as the solid-line, this introduces larger ΔT_C at the low temperature side, and smaller ΔT_C at the high temperature side. This phenomenon can also be observed in the experimental results from Dalle Donne and Sordon (1990): the outer wall measurements of the HTC are much lower than the ones near the inner wall, as shown in Figure 7.9. However, the magnitudes of these two types of measurements should be comparable.

Correspondingly, in the theoretical model, a similar simplification has been made during validation. To extrapolate the temperature inside the unit cell, we use the effective thermal conductivity k_{eff} as a function of the mean bed temperature T_m to compare with experiments, while in practice the near-wall temperature T_n should be used. The difference is notable for pebble beds having low effective thermal conductivities, and thus having larger values of $|T_m - T_n|$. This effect in the near-wall regions can be sketched as in Figure 7.10-(b). It turns out to give an overestimation near the high temperature region, and an underestimation near the low temperature region.

Furthermore, the gas properties depend on the local temperature, as shown in Table 7.2. Using the near-wall temperature T_n instead of the local interstitial gas temperature T_g introduces additional errors. Since the gas has lower thermal conductivity than the bulk material of pebbles, in a pebble bed, $T_g < T_n$ at the heater side and $T_g > T_n$ at the coolant side. For instance, if the thermal conductivity of the interstitial gas is a monotonic increasing function of temperature, the present model overestimates the value of the HTC at the high temperature region, and vice versa.

Except for the experiments conducted by Abou-Sena et al. (2003), the mechanical field has not been separated from the temperature field. However, the size of the contact zone is important for the beryllium pebble-wall interactions, as shown in Figure 7.8-(b). With more information from the experiments, the prediction of the present model can be better validated. We have also observed the changes of the average coordination number in the bulk region with the discrete

element simulations in Chapter 3. The stress state can also introduce a variation of the contact number between pebbles and the wall during heating. In the theoretical model, however, the contact number has been fixed as an intermediate value ($L/R = 4/\pi$), and this gives an overestimation in the region with low compressive stresses, and an underestimation in the region with high compressive stresses.

The present HTC model with a unit cell presumes that k_{eff} is independent of the near-wall packing, except for the first (1/2)-diameter region to the wall. Nevertheless, the changes of the topology locate mainly in the region of 4 diameters away from the wall (Gray, 1968). Recently, with the help of microtomography, it was possible to investigate how the packing factor changes near-wall (Reimann et al., 2007). The effective thermal conductivity could be varied, most likely to be decreased, but the influence is not clear up to date. According to this fact, the HTC model can give an overestimation compared to the real situation.
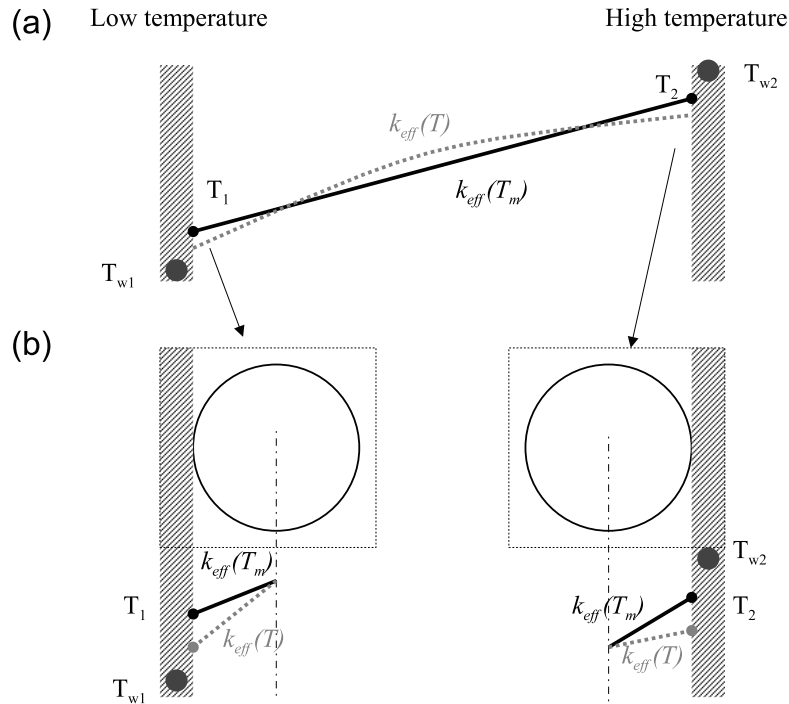

Figure 7.10: (a) Schematic drawing of temperature distributions; (b) the near-wall regions.

The above mentioned facts influencing the accuracy of the predictions are listed in Table 7.5. Despite the fact that the current model already gives reasonable representations of the experimental observations, the influences of factors (1)-(3) can be eliminated if more information can be provided in further experiments. For instance, T_n and T_g can be derived from the experimental data as a function of T_m, and moreover, the compressive stresses can be observed explicitly as provided by Abou-Sena et al. (2003). Here, we discuss the reasons why inaccuracy exists during validation. However, for a fully coupled thermo-mechanical analysis of the structure containing pebble beds, we consider local temperature and stress state in the interfacial model, which eliminates the influences of (1) and (3). In engineering applications, the prediction of the present theoretical model, h_0, gives usually an overestimation, such as in the benchmark exercises of HELICA and HEXCALIBER. We suggest to use $\bar{h} = \alpha h_0$ ($\alpha < 1$) to calibrate the

heat transfer coefficient, for example, a value of $\alpha = 0.6 \sim 0.8$ has been used in the analyses of the HELICA and HEXCALIBER benchmark exercises (Gan and Kamlah, 2008).

Table 7.5: Factors influencing predictions of the present HTC model

Influencing factors	Low temperature	High temperature
(1) Effective thermal conductivity using T_m †	underestimation	overestimation
(2) Gas properties using T_w	underestimation	overestimation
(3) Without compressive stress	underestimation	underestimation
(4) Near-wall topology	overestimation	overestimation

† For both the theoretical model and experiments.

7.5.2 Gap formation

In the case of gap formation, a layer of interstitial gas can be added to the unit cell. The solid-solid region is removed from this model, and the gap formation can be taken into account by varying the thickness of the gas gap. A simplified model can be written as

$$\bar{h}_0 = (1/h_0 + \delta/k_{g,\infty})^{-1} \ , \tag{7.17}$$

where δ is the thickness of the additional gas gap, and h_0 is the solution of the unit cell without the solid-solid region.

In spite of the simplification made in the present theoretical model, it gives reasonable predictions. The model has been implemented in ABAQUS, coupled with the phenomenological model for the bulk region of pebble beds, to perform thermo-mechanical analyses of HCPB blankets under fusion-relevant conditions.

7.6 Summary

In this chapter, the heat transfer via the pebble-wall interface has been investigated theoretically. A model to estimate the interfacial heat transfer coefficient, based on the temperature and mechanical fields, has been proposed. In this model, a unit cell, consisting of a solid-solid region, a solid-gas region and thermal radiation, has been analyzed.

Comparisons are made to validate the present HTC model to limited available experiments. The differences between the predictions and the experimental data can be explained through the discussions of the current HTC model. This model can be implemented straightforwardly in a finite element code to perform fully coupled thermo-mechanical analyses of structures taking into account pebble beds.

Chapter 8

Application

In this chapter, we first review the existing mock-up experiments of pebble beds, among which the HELICA out-of-pile experiment has been used as a benchmark exercise for EU associations. The present phenomenological model, as well as the interfacial model, is employed in the finite element analysis for the overall behaviour of the lithium orthosilicate cassette, which is heated by electric heaters to represent volumetric heating inside the pebble bed. Predictions of the numerical study are compared with the experiment, including temperatures measured by the thermo-couples located inside the pebble bed and the lateral deformation of the cell. Finally, some remarks concerning structural analyses of pebble beds are made.

8.1 Background

To investigate the thermo-mechanical properties of pebble beds under fusion-relevant conditions, mock-up experiments are carried out by means of in-pile and out-of-pile tests. For the first type of experiments, the pebble bed assembly (PBA) and EXOTIC experiments are two typical examples (van der Laan et al., 2000a,b, 2002; Fokkens, 2003; Piazza et al., 2004). These in-pile experiments are usually put into high flux fission reactors, such as the HFR in NRG Petten, the Netherlands. Thermo-mechanical properties and, especially, irradiation effects can be studied by this type of experiments. However, due to the limited space in the fission reactor core, comparably small capsules have been used. In such cases, the ratio of the diameter of pebbles to the dimension of capsules is too large to represent the overall behaviour of pebble beds used in fusion blankets.

The out-of-pile experiments have been used, besides other purposes, to validate the material models which have been proposed by different EU associations (NRG, Petten; DIN, Palermo; and FZK, etc.). Among these mock-up experiments, HELICA (HE-FUS3 Lithium Cassette) and HEXCALIBER (HE-FUS3 Experimental Cassette of Lithium and Beryllium Pebble Beds) are launched in the HE-FUS3 facility at ENEA Brasimone, Italy (Dell'Orco et al., 2006, 2007). Thermo-couples (TCs) and linear variable displacement transducers (LVDTs) have been placed to monitor the responses of the pebble beds under different loading conditions. To minimize the disturbing by TCs located inside the pebble layers, their number has to be limited. On the other hand, stresses and strains are difficult to be measured experimentally inside pebble beds. Therefore, the finite element simulation using a proper material model is very important

to understand the thermo-mechanical behaviour of pebble beds. The comparison between the simulation and experiments can be carried out at the positions where the measurements are made in experiments.

8.2 Finite element model of HELICA mock-up

In the following sections, the HELICA mock-up experiment is modelled and analyzed by using the coupled thermo-mechanical model, which has been implemented in ABAQUS. A two-cycle loading has been simulated, in order to investigate not only the response at the maximum loading, but also cyclic effects.

8.2.1 Experimental setup

As an out-of-pile experiment, the HELICA mock-up consists of (see Figure 8.1): a single welded cell, made in ferritic-martensitic steel (ASME SA 387 grade T91); the breeder cell, divided into three sub-cells by two flat electric heaters, namely, two outer sub-cells and one middle sub-cell; two cooling plates, constrained by a stack of cup springs to provide adequate heat conductance at the interface to the cassette; a flanged plug, closing the test cell and providing the power supply and instrumentation lead-throughs. The HELICA mock-up is filled with breeder ceramic pebbles (Li_4SiO_4, diameters between 0.2~0.4 mm) and heated by the two above mentioned electric heaters located inside the breeder cell to reproduce the designed temperature increase of the pebble bed. Each electric heater generates a surface heat flux of 42 kW/m^2 in 6 one-hour subsequent steps. The breeder cell filled with pebbles is divided into the 3 sub-cells mentioned earlier, 446 mm in width, 192 mm in depth and 4.6 mm in thickness. During the test, the temperature inside the breeder cell can be read out by TCs located inside the pebble layer. These TCs are placed at different distances, namely, 55/100/150 mm, to the first wall (FW). Furthermore, the displacements at specific places, e.g., horizontal and vertical directions, are measured by LVDTs. In HELICA, 6 LVDTs measure the lateral deformation of the steel cassette during operation. The stiffness plate is constantly pressed with the magnitude of 0.09 MPa. HELICA has been cooled by helium gas with an inlet flow rate of 8 g/s, pressure of 1.5-1.7 MPa and temperature of 200^oC; the breeder cell has been purged by a helium flow of 0.002 g/s, pressure of 0.05-0.1 MPa and inlet temperature of 50^oC.

8.2.2 Geometric model of HELICA mock-up

Considering not only the ratio of the width to the thickness of the cassette, but also similar loading conditions along the width, a 2D generalized plain strain model has been used in this investigation. The out-of-plane deformation is set to be identical to the one caused by thermal expansion of the cassette. Despite the fact that the helium temperature varies along the cooling channel, here we take the helium temperature at the middle cross-section of the cooling plate as the reference value, since the structural materials have higher thermal conductivities than helium and hence are less sensitive to the variation of the helium temperature. Furthermore, the geometric symmetry of the model has been taken into account for reducing the size of the FE model, by applying mechanical and thermal symmetry boundary conditions to this

plane. Figure 8.2 shows the geometric model of HELICA with finite element meshes, based on the IGES-file provided by ENEA Brasimone. In Figure 8.2, different materials are shown in different colors: T91 steel (yellow), stainless steel (magenta), pebbles (red), inconel 718 (green), kanthal (blue) and soft gasket (white). The material data used in this analysis are taken from *HELICA: Material Database* (Fokkens, 2005), while the ones of the ceramic breeder pebble bed are referred to the uniaxial compression and creep experiments performed in FZK (Reimann et al., 2006a). The mechanical properties of the structural materials, such as Young's modulus and the Poisson's ratio, are listed with respect to temperature. The properties of thermal expansion, specific heat and thermal conductivity are also included in this material database to perform the coupled thermo-mechanical analysis. The phenomenological model of pebble beds, as discussed in Chapter 4, has been adopted to describe the overall thermo-mechanical behaviour of ceramic breeder pebbles inside the breeder cell. Moreover, the identification method has been employed, as in Chapter 5, to extract the material parameters from experiments for the pebble bed considered here. The properties of all the other materials are implemented in ABAQUS as separate data sheets.

In this analysis, 4-node bilinear coupled temperature-displacement generalized plane strain elements (CPEG4T element in ABAQUS) are used. There are 3664 elements in the present model, among which 1395 are the elements of the pebble layer. With generalized plane strain elements, the deformation of a uniform out-of-plane strain can be taken into account, as caused by thermal expansion of the container's material. The mesh can be found in Figure 8.2, and it is refined in the high temperature gradient area, i.e. inside the ceramic breeder layer.

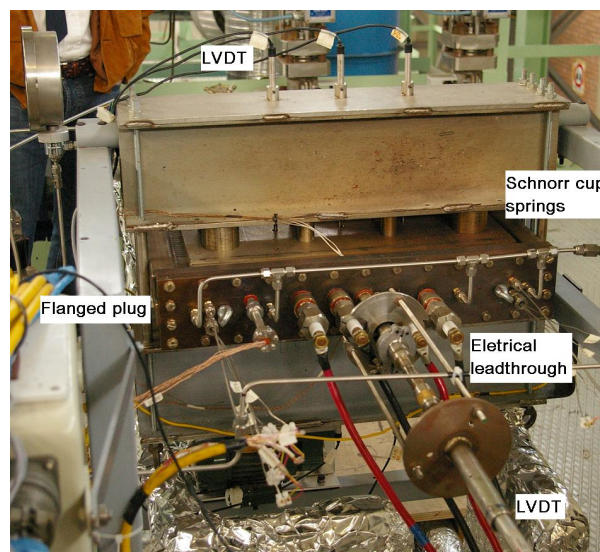Figure 8.1: HELICA mock-up (ENEA Brasimone) under testing in the horizontal direction.

8.2.3 Boundary conditions and loading history

The boundary conditions can be described as: interactions between the parts of HELICA mock-up are modelled by surface contact; inside the cooling channels, and along the air-structure interfaces, film coefficients (listed in Table 8.1) are applied to simulate the heat transfer via
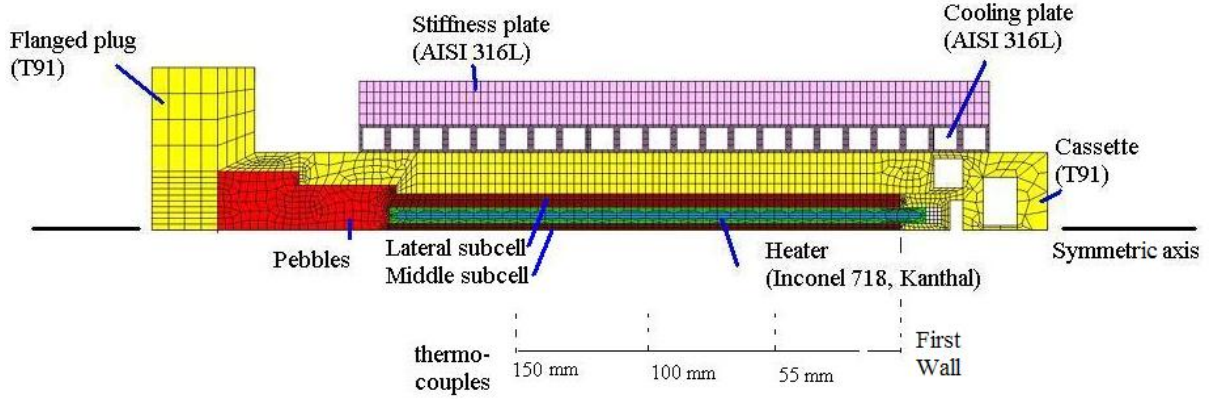
Figure 8.2: Finite element mesh of HELICA mock-up.

the coolant-structure and air-structure interfaces. For the pebble-wall interface, the friction coefficient is set to be 0.02~0.05 (the case of 0.02 is shown in this chapter), and the theoretical model of the interfacial heat transfer has been implemented as discussed in Chapter 7. A forced helium flow in the channels of the cooling plate has an initial inlet temperature of 200^oC. The helium temperature increases in the range of $200\sim300^oC$ during the heat-up operation. The surface of the mock-up is surrounded by air at room temperature (20^oC).

The loading history of the electric heaters is plotted in Figure 8.3. In the first hour, the HELICA mock-up is uniformly heated up from room temperature to 200^oC as the start-up procedure. Then loading cycles are performed, lasting 8 hours for each cycle. The electric heater generates a surface heat flux ramping up from 0 to 42 kW/m^2 by 6 one-hour steps, and the unloading step lasts 2 hours. The numbers of the subsequent steps are listed in Figure 8.3. In each loading step, the surface heat flux is increased by 7 kW/m^2 in the first 10 minutes, and kept constant in the following 50 minutes. Two loading cycles are applied in this investigation.

A uniform volumetric heating is applied to the electric heaters to provide the designed surface heat flux q (kW/m^2). The corresponding magnitude of the power density ρ (MW/m^3) can be calculated from q and the thickness of the heater, h (mm) as

$$\rho = \frac{q}{h} \ . \tag{8.1}$$

Table 8.1: Film coefficients in the analysis.

	Film coefficient (W/m^2K)	Reference sink temperature (^oC)
Coolant-structure	145	200~300
Air-structure	10	20

8.3 Thermo-mechanical analysis

The thermo-mechanical analysis of the above procedure has been performed in ABAQUS Version 6.6. The finite element calculation of two loading cycles takes around 3 hours on an IBM machine
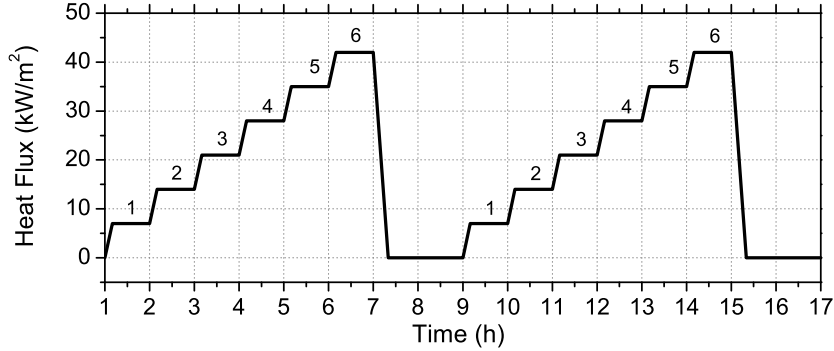
Figure 8.3: Loading history of the surface heat flux (kW/m^2) of the electric heaters during two loading cycles.

(Power 4) with 1.5 GHz CPUs. The contact algorithm, coupled with the nonlinear material model, needs extra iterations to reach convergence. The unloading paths cost more CPU time, due to not only the instability of the material under shearing but also contact iterations caused by surface separations during cooling down.

The yielding stress of the pebble bed (a few MPa) is much smaller than the one of the structural materials (hundreds MPa), and this means that a small variation of stresses has totally different effects on those two kinds of materials. An acceptable error in the structural material regions, which could be introduced and accumulated in the finite element calculation, may cause the pebble bed to deform with a very large inelastic increment, probably leading to a physically non-realistic state or the instability of the material. Therefore, during the calculation, the default criterion for convergence in ABAQUS is not valid any more. A much stricter criterion is adopted in this investigation, in order to reach convergence and obtain physically realistic results in the region of the pebble bed. The criterion is changed in such a way that the maximum residual forces on nodes will not introduce significant inelastic strains in the pebble bed. This modification has been made by setting an upper limit for the residual force in the part of the user defined average flux $\tilde{q}_u^\alpha$ of the command "*CONTROLS, PARAMETERS=FIELD, FIELD=DISPLACEMENT" in ABAQUS.

In this section, two cycles of loading have been simulated using the present phenomenological model for pebble beds. The finite element calculation is compared to experimental data, including the temperature and displacement measurements. The calculated stresses and strains inside the pebble layer are also reported.

8.3.1 Temperature filed

Figure 8.4 shows the comparison of temperature history between the measurements and predictions. The experimental data are taken from a typical cycle during the cyclic loading in the experiments at ENEA Brasimone. The locations of the TCs along the thickness are sketched in a small plot in Figure 8.4-(a). Since there are symmetrically distributed TCs in the HELICA mock-up, except for the ones at the plane of symmetry (TC_01), the mean values of other

TCs (TC_02, TC_03, TC_04) are calculated from two corresponding data sets. The prediction underestimates the temperature at 55 mm (the maximum difference within 15^oC), while it overestimates the ones at 100 and 150 mm (the maximum difference within 30^oC). For this simplified FE model, the heat flux generated by the heater and the temperature of the coolant are assumed to be independent of positions, while in the mock-up experiment they are varied by several factors, e.g., the position-dependent coolant temperature. Despite the fact that there are 5~10% differences between the initial states of the predictions and measurements, the errors of FE predictions are less than ±10% during the whole loading cycle. The calculated values of the second cycle have also been plotted out to show the cyclic effect. In this investigation, the cyclic effect on the temperature changing is ignorable.
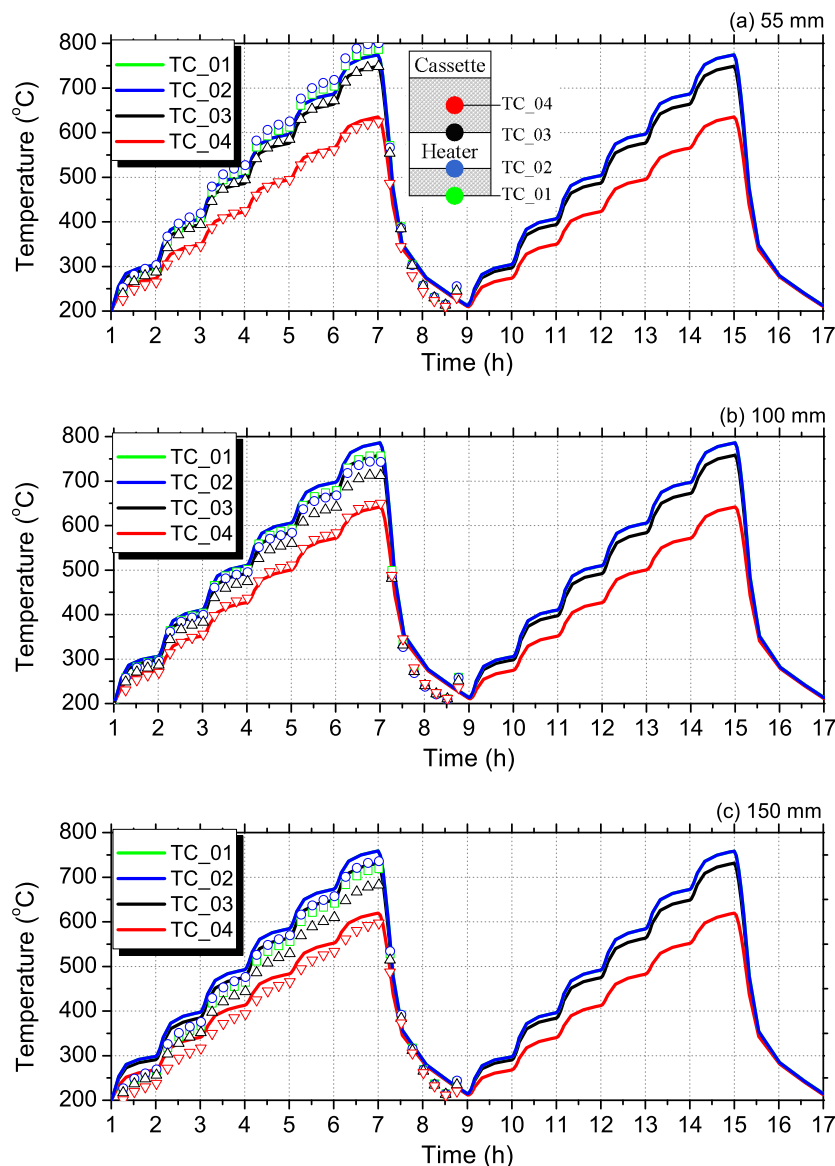

Figure 8.4: Temperature over time during two loading cycles: (a) 55 mm; (b) 100 mm; (c) 150 mm to the FW. Dots, experimental data; solid lines, F.E. calculation (unit: ^oC).

The temperature distribution at the maximum heating is shown in Figure 8.5, with the deformed

configuration. Loading steps in the second loading cycle, namely, step No. 2, 4, and 6 as shown in Figure 8.3, are plotted to show the evolution of the temperature distribution. The maximum temperature in the pebble bed locates in the middle layer of the breeder cell, and reaches close to 790^oC at maximum load. Due to the bending of the top surface of the cassette, gaps are formed between the cooling plate and the cassette, which slightly change the pattern of the heat transfer.
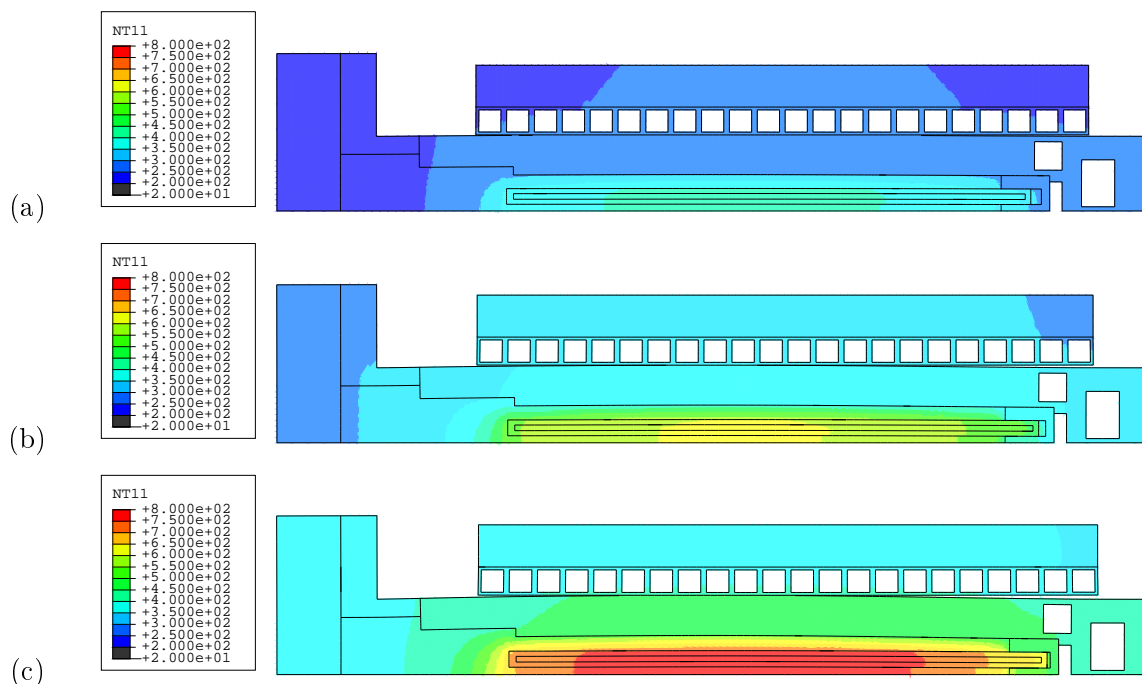

Figure 8.5: Calculated temperature distribution at: (a) Step 2, (b) Step 4 and (c) Step 6, the maximum load (unit: ^oC), with deformations at a scale factor of 5.

8.3.2 Mechanical field

In the coupled thermo-mechanical analysis, the mechanical field, as well as the temperature field, has been obtained. The mechanical field is important in the analysis of pebble beds, due to the fact that not only the thermal and mechanical fields are coupled, e.g., the effective thermal conductivity depends on the average contact area of pebbles and the number of contacts, but also the stress concentration may cause crush of individual pebbles during the operation. Figure 8.6 shows the calculated hydrostatic pressure and von Mises stress at the locations of the TCs (TC_01) along the axis of symmetry during the two loading cycles. In each cycle, there are obvious decreases of the stresses at the 5th and 6th loading steps, and this behaviour is caused by the creep deformation at the relatively high temperatures. The main reasons for this phenomenon are the re-configuration of the local packing structure of pebbles and creep of the bulk material. Friction forces at the pebble-wall interfaces and thermal expansion of the heaters are present in this analysis, and it turns out to push the pebbles against the FW. Therefore, the value of hydrostatic pressure at 55 mm to the FW is higher than the one at 100/150 mm. The hydrostatic pressure after unloading reaches almost zero, but no tensile stress is present

in the pebble layer, which is consistent with the nature of the non-cohesive granular materials. Differences between two loading cycles can be observed but they are not significant.

Figure 8.7 shows the distributions of (a) hydrostatic pressure and (b) von Mises stress at the maximum load. The maximum hydrostatic pressure (around 4.9 MPa) locates near to the FW, and the reason for this has been explained above. Another reason for this phenomenon is that the structural compliance near the first wall is less than the one in the middle, see the deformed shape in Figure 8.5. In this investigation, a dependence of the maximum hydrostatic pressure on the friction coefficient between pebbles and the wall has been found. For a larger friction coefficient, a higher magnitude of the resulting hydrostatic pressure occurs. Inside the high hydrostatic pressure regions, crush of single pebbles is likely to be observed in experiments. The DEM simulation in Chapter 3 also shows the dependence of the maximum normal contact force on the hydrostatic pressure. If we scale the maximum contact force, $f_{\max}$, between pebbles considered here to the ones with 0.5 mm diameter by Eqn. (3.53), the value is close to 5.5 N in the $p = 4.9$ MPa region. However, the average crush load on dried pebbles in experiments is 7~8 N with a 20% of scattering (Piazza et al., 2001b; Reimann et al., 2005a). It is also found that the coordination number influences the crush probability of single pebbles (Marketos and Bolton, 2007), while the experimental data normally cover only the case of $n_C = 2$.

The maximum von Mises stress occurs inside the outer sub-cell. This is mainly introduced by different thermal expansion coefficients of the cassette wall and the electric heater, respectively, which shears the pebbles inside the outer sub-cell. During the unloading step, the direction of the shear stress changes, and it turns out to recover part of the inelastic strains accumulated in the previous loading steps.

Figure 8.8 shows the evolution of (a) volumetric inelastic strain and (b) volumetric plastic strain of the pebble bed at the positions of TC_01 (55, 100 and 150 mm to the FW). The volumetric inelastic strain is the summation of the volumetric plastic and creep strains. The increments of the volumetric inelastic strain at the 5th and 6th steps are higher compared to the others, since the creep strain rate is larger at high temperatures. On the contrary, the increments of the volumetric plastic strain at the 5th and 6th steps decrease in Figure 8.8-(b), due to the fact that creep deformations reduce stresses. The maximum volumetric inelastic strain reached in the second cycle is slightly higher than the one in the first cycle. During unloading, the volumetric plastic strain recovers, and even some dilations exist inside the pebble layer, e.g., near TC_01 at 55 mm. Due to the shrinking of the electric heaters during unloading, the pebbles in the middle sub-cell are carried back by friction forces to the original configuration.

Figure 8.9 shows the distributions of (a) volumetric inelastic strain and (b) volumetric plastic strain at the maximum load of the second cycle. The distributions of the two variables are similar. The maximum volumetric inelastic strain is around 2.1%, and the maximum volumetric plastic strain reaches 1.5% inside the pebble bed.

One node of the FE model, where the LVDT locates in the experiment, has been monitored during the calculation. Figure 8.10 shows the comparison between the experimental data and predictions. These two sets of data are offset by the displacement obtained at the beginning of the second cycle, in order to provide results independent of the irreversible deformation during the first starting cycle. Cyclic effects achieve saturation at the end of the second cycle, see Figure 8.10. Considering the scatter of the measurements, the present finite element analysis

(a)

(b)
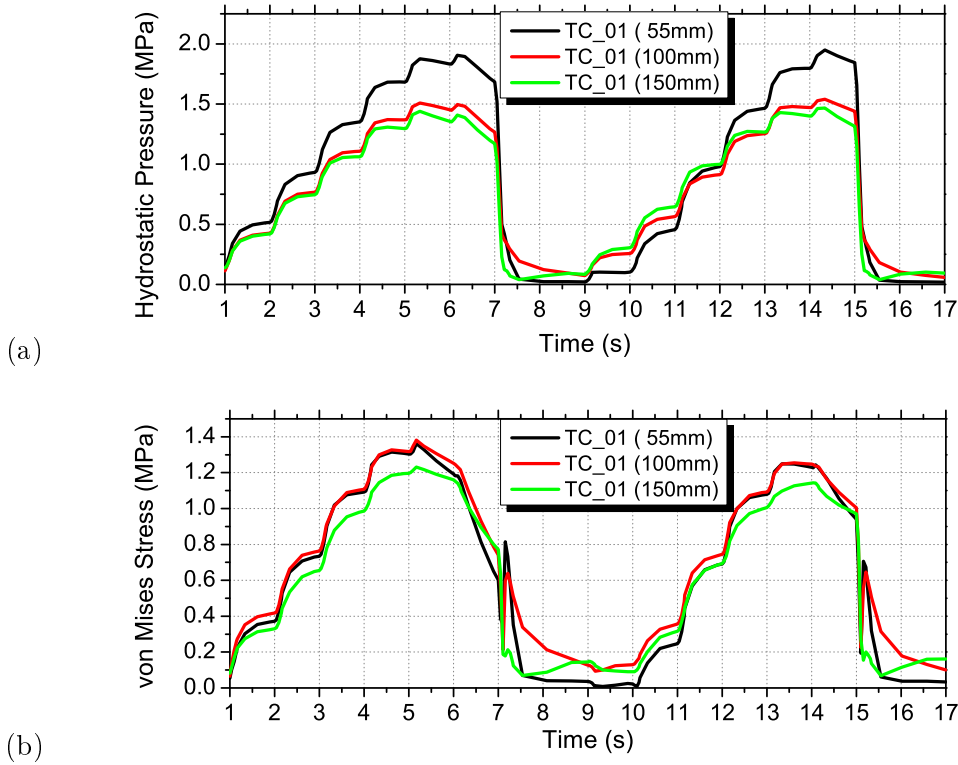
Figure 8.6: Stresses over time during two cycles: (a) hydrostatic pressure; (b) von Mises stress (unit: *MPa*).

(a)

(b)
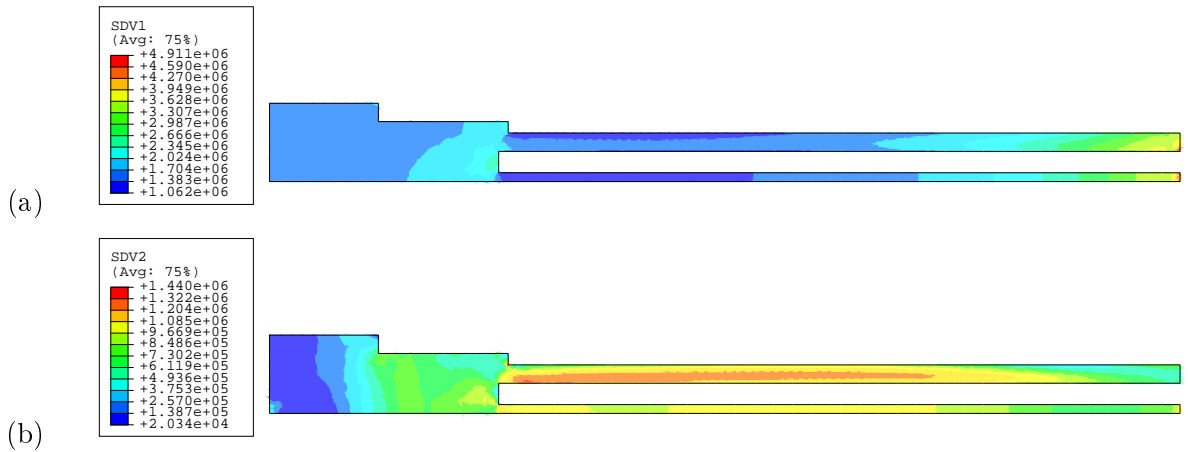
Figure 8.7: Stress distributions inside the pebble layer at the maximum load (Step 6 in the second cycle): (a) hydrostatic pressure; (b) von Mises stress (unit: *Pa*).

Figure 8.8: (a) Volumetric inelastic strain and (b) volumetric plastic strain over time during two cycles (unit : %).
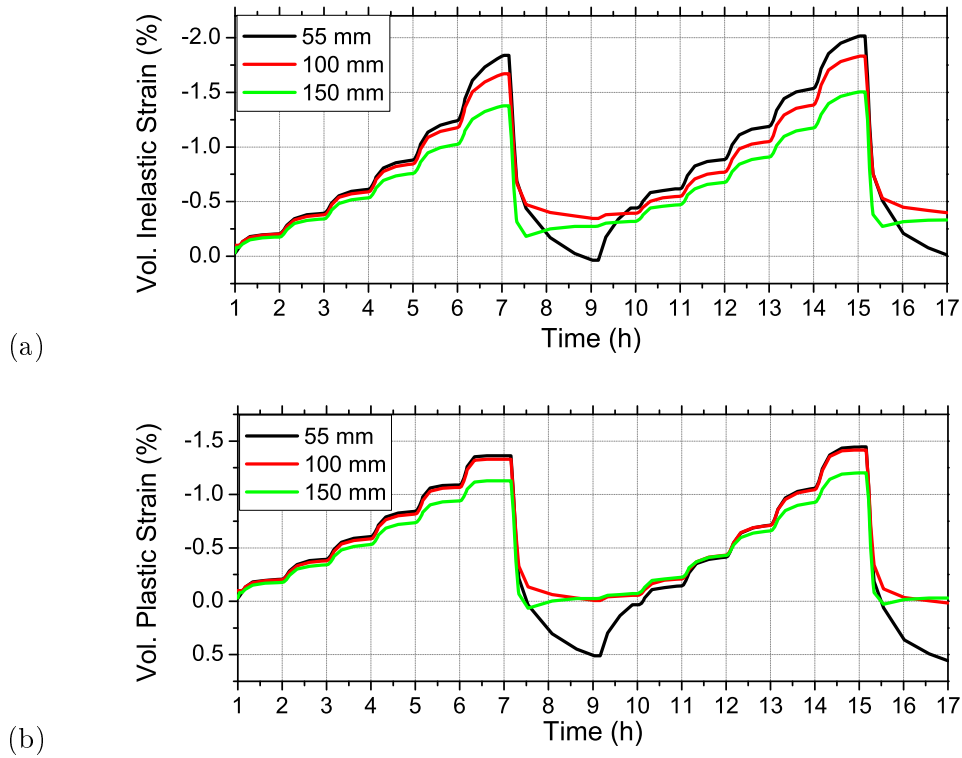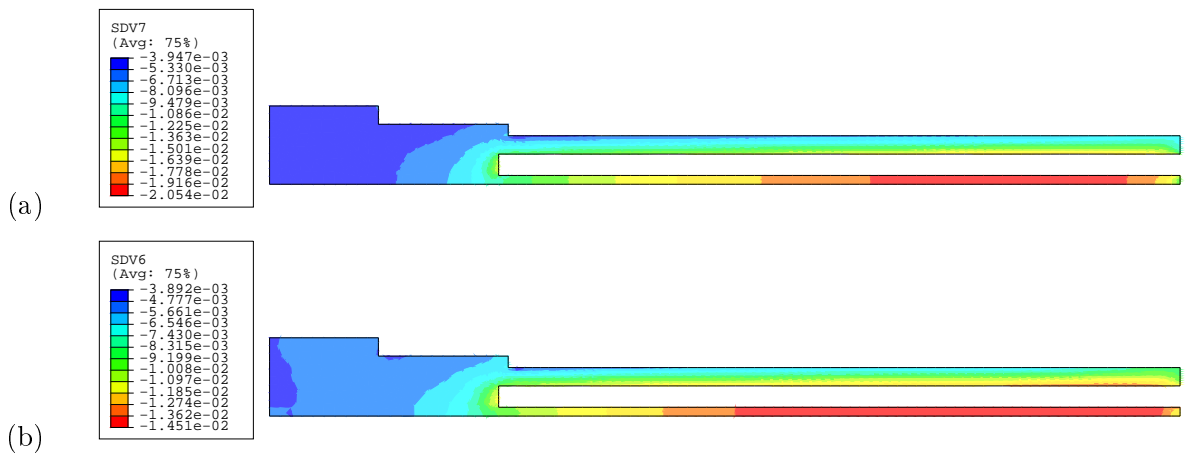

Figure 8.9: Volumetric strain distributions inside the pebble layer at the maximum load (Step 6 in the second cycle): (a) inelastic strain; (b) plastic strain.
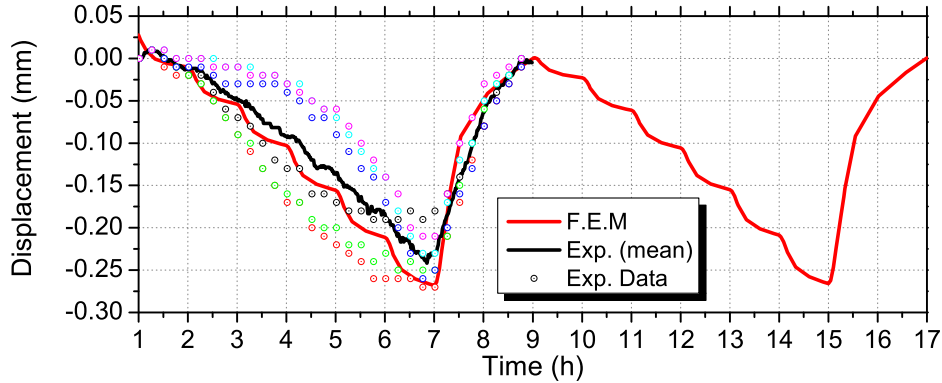
gives a reasonable prediction.

Figure 8.10: Displacement of HELICA (unit: mm), comparison between LVDTs' measurements (scattered dots) and the calculated value (the solid line).

8.4 Discussion and conclusion

Based on the present numerical study of the HELICA mock-up experiment, the interfacial heat transfer coefficient, effective thermal conductivity of the pebble bed and gap formation are discussed in this section.

8.4.1 Heat transfer coefficient

With the interfacial heat transfer model as discussed in Chapter 7, the HTC can be calculated by the local temperature and pressure in the finite element analysis. The temperature drop ΔT at the interface depends on the heat flux and the value of HTC. Figure 8.11 shows the temperature distributions along the cross-section at 100 mm to FW, and the experimental data are also plotted for comparison. The maximum temperature locates in the middle sub-cell, and the temperature decreases in the direction of the heat flux, from the electric heater to the cassette. For different loading steps, there are temperature drops at the interface of the heater and the outer sub-cell, as well as the ones at the interface of the outer sub-cell and the cassette. With the increase of the surface heat flux during loading (from step 1 to 6), the temperature drop ΔT increases, but meanwhile with the resulting changes of temperature and stresses, the HTC value changes. In the same loading step, the heat fluxes are almost the same at both the heater-pebble bed and pebble bed-cassette interfaces. However, the differences between the temperature drops, or the HTC values, are introduced by differences of the temperatures and pressures at these two interfaces.

8.4.2 Effective thermal conductivity

The effective thermal conductivity of pebble beds depends on both the local temperature and volumetric inelastic strain, and this has been implemented in our present phenomenological
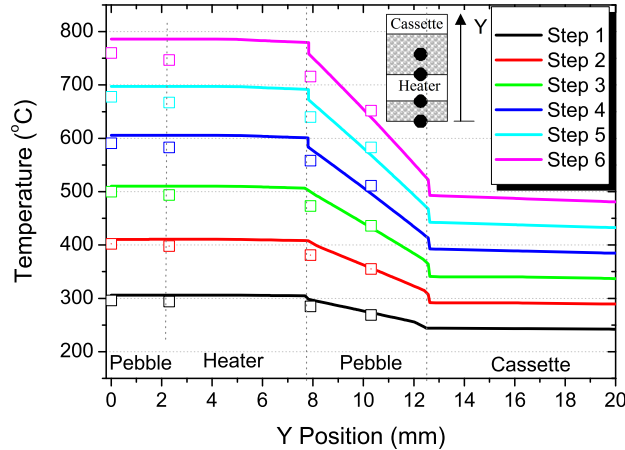
Figure 8.11: Temperature distributions at the cross-section 100 *mm*, at different steps. Solid lines, calculation; dots, measurements.

model. It is suggested (Reimann et al., 2006a) that the thermal conductivity has about 12% reduction for the beds with smaller sized pebbles as used in HELICA and HEXCALIBER mock-ups, decreasing the average diameter from 0.4 (the reference pebbles) to 0.225 *mm*. Knowing the calculated temperature and strain distributions, it is convenient to plot out the effective thermal conductivity of the pebble bed. Figure 8.12 shows the evolution of the effective thermal conductivity of the Li_4SiO_4 pebble bed during two cycles, and three points are taken from the locations of TC_01 along the axis of symmetry, namely, 55/100/150 *mm* to the FW. The effective thermal conductivity increases during the loading steps, and it has a similar trend with the changing of the local temperature, since it changes linearly with respect to temperature and is insensitive to strains. The cyclic effect on the thermal conductivity is negligible.

Figure 8.13 gives the distributions of the effective thermal conductivity of the Li_4SiO_4 pebble bed at two different steps. As shown in Figure 8.13-(a), the thermal conductivity at the maximum load ranges from 0.842 to 1.044 *W/mK*, depending mainly on the temperature distribution, as shown in Figure 8.5-(c). The maximum value locates in the middle sub-cell between the heaters. Figure 8.13-(b) shows the distribution of the thermal conductivity after the unloading, and there is only small variation over the whole region of the pebble bed, from 0.768 to 0.782 *W/mK*. The inhomogeneous distribution is induced by the inelastic strains.

8.4.3 Gap formation

During operation, the pebble layer is mainly under compressive stresses. A negative volumetric inelastic strain exists almost everywhere in the whole pebble bed region, which does not fully recover during unloading, see Figure 8.8. It is expected that gaps will be formed at the pebble bed-heater or pebble bed-cassette interface after unloading. However, in HELICA, the heaters shear back and forth during loading cycles. One of the interesting properties of granular materials is that the volume increases while being sheared, and this can be predicted by the shear failure surface in the modified Drucker-Prager-Cap theory with non-associated plastic flow. The stress history in Figure 8.6, especially the one of von Mises stress, shows that the shear stress acting
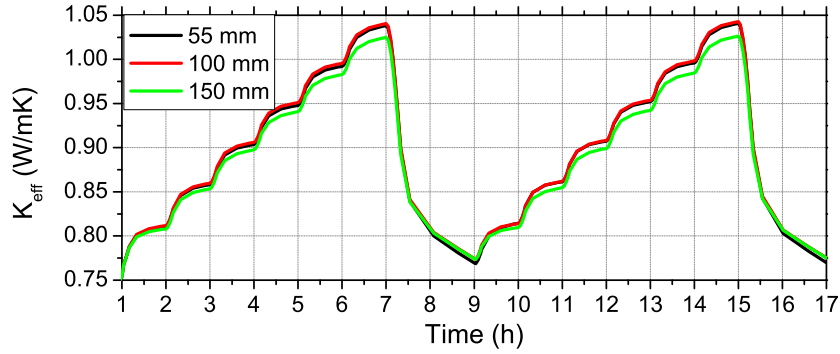
Figure 8.12: Effective thermal conductivity of the Li$_4$SiO$_4$ pebble bed over time at 55/100/150 mm of symmetric axis (unit, W/mK).
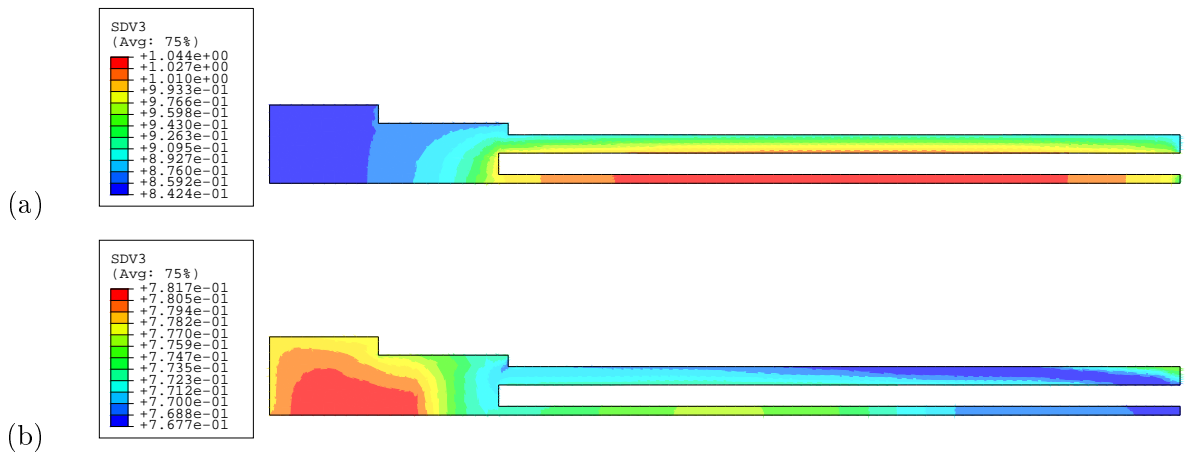

(a)

(b)

Figure 8.13: Calculated profile of the effective thermal conductivity: (a) at Step 6; (b) after unloading (unit, W/mK).

in the pebble layer changes its sign during unloading. The stress state during unloading is different from the one during loading. The unloading case is actually a pure shearing of the pebble layer, which can be seen from the fact that the hydrostatic pressure reduces almost to zero while a non-zero von Mises stress is present. This leads to a partial recovery of the inelastic strains accumulated during loading, and increases the volume occupied by the material. The deformation after unloading has been investigated, and Figure 8.14 shows the only observable gap in HELICA. The gap has been formed between the two heaters and close to the FW, and the width of the gap is 0.29 mm.
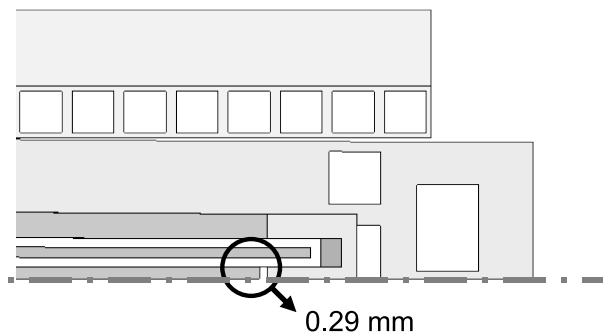
Figure 8.14: Gap formation in HELICA after unloading, with deformations at a scale factor of 5.

8.4.4 Remarks on the simulation

According to the present finite element analysis of the HELICA mock-up experiment, the following remarks can be made:

- The maximum temperature will be reached between the two electric heaters, and the maximum value depends on both the magnitude of the heat flux provided by the heaters and the configuration of the cooling channels. Regions with high temperature gradient locate in the outer sub-cells. Cyclic effects of the ceramic breeder pebble bed are ignorable.

- A hydrostatic pressure develops during the loading steps, and decreases in high temperature regions, due to the creep deformation of the pebble bed. The maximum value is reached near the interface of the FW in the middle sub-cell. The value is so high that it is likely to break individual pebbles in this region. The hydrostatic pressure reduces nearly to zero after unloading, and no tensile stress exists.

- Gap formation is found in the analysis, and the width of the gap is around 0.29 mm. The location is at the interface of the FW in the middle sub-cell of the pebble bed.

- When pebble beds are present in the structural analyses, extra controls for convergence have to be made in the finite element analysis to both reach convergence and obtain reasonable results. For structural analyses for HCPB-TBM design, the pebble beds have a strong influence on the temperature field. The modified Drucker-Prager-Cap model can describe precisely the behaviour of pebbles during both loading and unloading. The mechanical variables, in turn, influence significantly the temperature distribution in the fully coupled thermo-mechanical analysis.

- A 3D analysis will provide more details of this mock-up experiment, but the problem remains mainly in the scale of the finite element calculation, rather than verification of the material model.

8.4.5 Other applications

Within the framework of the EFDA R&D activities, the present phenomenological model has also been used to investigate the pre-compaction procedure of the pebble bed assembly in NRG Petten (Gan and Kamlah, 2006, 2007a), and the thermo-mechanical behaviour of the HEXCALIBER mock-up experiment in ENEA Brasimone (Gan and Kamlah, 2007b, 2008). Moreover, with the help of the phenomenological model for pebble beds and the identification method of the material parameters proposed in this work, Mazzone et al. (2006) have investigated a typical HCPB-TBM structure under electromagnetic loading. To understand the thermal mechanical response of a HCPB blanket under volumetric heating, which is induced by neutron and gamma-ray radiation in a fusion reactor, a typical sandwich structure of the DEMO configuration consisting of both ceramic breeder and beryllium pebble beds under the power density profile during operation has also been studied (Gan et al., 2007).

8.5 Summary

In this chapter, HELICA, an out-of-pile mock-up experiment in ENEA Brasimone, has been analyzed using the phenomenological model of pebble beds developed in this work. Using 2D generalized plain strain elements, the fully coupled thermo-mechanical analysis of this mock-up experiment has been performed. The calculated results are reported, including the temperature, stress-strain fields and the effective thermal conductivity of the pebble bed. As a benchmark exercise, we compare the predictions with experimental measurements, which shows the validity of the present phenomenological model and the interfacial heat transfer model. This work exhibits the feasibility of the simulation of large scale experiments, and the capability of structural analyses taking into account the special features of pebble beds. The thermo-mechanically coupled analysis will be an efficient and important tool for the design of HCPB blankets.

Chapter 9

Conclusion

In this work, tritium breeder and neutron multiplier pebble beds have been modelled by a discrete element method and a continuum mechanics approach, to perform thermo-mechanical analyses of structures containing these materials under fusion-relevant conditions. In addition to describing the thermo-mechanical behaviour of pebble beds, this strategy also focuses on the utilization of the available experimental data. This not only makes use of the properties of single pebbles, but also identifies the material parameters in the phenomenological model from typical experimental setups for pebble beds.

In the first approach, each single pebble is considered an individual element, and the interactions between elements are revealed by the discrete element method. In order to provide a reasonable initial configuration for the discrete element simulation, in particular, with periodic boundary conditions and a high packing factor, an algorithm for random close packing has been developed. By simulating different assemblies of pebbles under uniaxial compression, similar distributions of contact forces have been achieved, regardless of the initial configuration and loading level. Moreover, the average and maximum contact forces, as well as the average coordination number in the representative volume element have been found to be related to a macroscopic quantity, namely, the hydrostatic pressure. This provides important information for understanding the overall behaviour of pebble beds, such as the nonlinear elasticity and strain-dependent thermal conductivity. The discrete element method provides promising solutions for pebble bed related problems, such as the quantitative analysis of the crush probability, and moreover the yield surface.

In order to take into account pebble beds in an engineering scale and describe the material properties in HCPB-TBM blankets, the phenomenological approach has been presented. According to the experimental observations and the requirements for the capability of carrying out coupled thermo-mechanical analysis, the present phenomenological model includes a nonlinear elasticity law, the Drucker-Prager-Cap model, consolidation creep and strain-dependent thermal conductivity. We have proposed a customized method to identify the material parameters from the empirical curves of the available experiments, instead of using a trial-and-error method. This method can be applied for different types of pebble beds, and moreover, it introduces thermo-plasticity into our present phenomenological model by using temperature-dependent empirical curves. Verifications of the phenomenological model have been made for different types of materials and at different bed temperature levels. Successful and unique identification of the material

parameters clearly shows physical relevance to the model. Implementation of the phenomeno-logical model into a finite element code has also been discussed in this investigation. A return mapping algorithm has been used as the integration scheme for a general rate-independent theory of plasticity with non-associated plastic flow. This provides the possibility to either improve the current phenomenological model, or transfer the model into other finite element codes. Furthermore, the same framework can be used to implement a new material model, e.g., a micro-mechanics based model.

As preparation for the structural analysis, the pebble bed-wall interactions have been investi-gated, with emphasis on the heat transfer coefficient of the interface. The interfacial model includes the dependence on both temperature and mechanical loads, which have been observed in experiments and thus are important for predicting the temperature distribution inside the pebble beds. Finally, as a benchmark exercise for material models proposed by EU associations, the HELICA mock-up experiment has been analyzed using the present phenomenological model. The predictions have been compared to measurements, which suggests that the framework of the current investigation satisfies the requirements in fusion blankets. The numerical tools for the thermo-mechanics of pebble beds will be efficient and important for the design and analysis of HCPB blankets.

In the future, several directions seem to be important for further developments for thermo-mechanics of pebble beds:

- First, as a sequential multi-scale approach, a micro-mechanics based phenomenological model can be investigated using the extension of the discrete element method into multi-axial proportional loading. The obtained material model can be implemented into a finite element code by a user-defined material routine like the one discussed in this work.

- Second, by linking the macroscopic and microscopic quantities, the crush probability of individual pebbles can be estimated according to the stress and temperature distributions of the structure. Data scattering of the crush experiments for single pebbles seems to be inevitable. However, this can be taken into account by the discrete element simulation. Further investigations are needed to study the influences of the coordination number, which can be obtained explicitly in the simulation, on the crush probability of single pebbles in a theoretical or experimental way.

- With the help of the discrete element method, the effective thermal conductivity and thermal expansion of pebble beds can be studied, and the micro-mechanical basis of these overall properties can be revealed.

- Moreover, in further structural analyses, it is needed to consider cost-efficiency of simula-tions. A simplified material model may be necessary. However, the basic characteristics of the present model should be preserved.

- For interfacial heat transfer, additional factors should be taken into account to improve the interfacial model, e.g., the near-wall topology and the changing of the contact number with respect to the loads.

- Finally, in the case of high level irradiation, swelling and degradation of pebbles can be taken into account either by the discrete element simulation, or as an internal variable in

the phenomenological model. This work would provide a basis for the implementation of the further experimental data for irradiation effects.

Bibliography

ABAQUS. *Analysis User's Manual, Version 6.5*. 2004a.

ABAQUS. *Theory Manual, Version 6.5*. 2004b.

A. Abou-Sena, A. Ying, and M. Abdou. Experimental investigation and analysis of the effective thermal properties of beryllium packed beds. *Fusion Science and Technology*, 44(1):79–84, 2003.

A. Abou-Sena, A. Ying, and M. Abdou. Effective thermal conductivity of lithium ceramic pebble beds for fusion blankets: A review. *Fusion Science and Technology*, 47(4):1094–1100, 2005.

A. Ahadi and S. Krenk. Implicit integration of plasticity models for granular materials. *Computer Methods in Applied Mechanics and Engineering*, 192(31-32):3471–3488, 2003.

M.P. Allen and D.J. Tildesley. *Computer Simulation of Liquids*. Clarendon Press, Oxford, 1987.

Z. An, A. Ying, and M. Abdou. Application of discrete element method to study mechanical behaviors of ceramic breeder pebble beds. *Fusion Engineering and Design*, 82(15-24):2233–2238, 2007a.

Z. An, A. Ying, and M. Abdou. Numerical characterization of thermo-mechanical performance of breeder pebble beds. *Journal of Nuclear Materials*, 367:1393–1397, 2007b.

R. Andreani, E. Diegele, W. Gulden, R. Lasser, D. Maisonnier, D. Murdoch, M. Pick, and Y. Poitevin. Overview of the European Union fusion nuclear technologies development and essential elements on the way to DEMO. *Fusion Engineering and Design*, 81(1-7):25–32, 2006.

E. Angel. *Interactive Computer Graphics: A Top-Down Approach with OpenGL*. Addison-Wesley Longman Publishing Co., Inc. Boston, MA, USA, 1996.

S. Joseph Antony. Evolution of force distribution in three-dimensional granular media. *Physical Review E*, 63(1):011302, 2000.

D. Aquaro and N. Zaccari. Pebble bed thermal-mechanical theoretical model - Application at the geometry of test blanket module of ITER-FEAT nuclear fusion reactor. *Fusion Engineering and Design*, 75-9:903–909, 2005.

Donato Aquaro and Nicola Zaccari. Experimental and numerical analysis on pebble beds used in an ITER Test Module Blanket. *Fusion Engineering and Design*, 81(1-7):707–712, 2006.

GK Batchelor and RW O'Brien. Thermal or electrical conduction through a granular material. *Proceedings of the Royal Society of London Series a-Mathematical Physical and Engineering Sciences*, 355:313–333, 1977.

James G. Berryman. Random close packing of hard spheres and disks. *Physical Review A*, 27 (2):1053, 1983.

N Bicanic. Discrete element methods. In Erwin Stein, Rene de Borst, and Thomas J.R. Hughes, editors, *Encyclopedia of Computational Mechancis*, volume 1, pages 311–337. John Wiley and Sons, 2004.

L. V. Boccaccini, N. Bekris, Y. Chen, U. Fischer, S. Gordeev, S. Hermsmeyer, E. Hutter, K. Kleefeldt, S. Malang, K. Schleisiek, I. Schmuck, H. Schnauder, and H. Tsige-Tamirat. Design description and performance analyses of the European HCPB test blanket system in ITER feat. *Fusion Engineering and Design*, 61-2:339–344, 2002.

L. Bühler. A simple model for the elasticity of granular materials in fusion breeding blankets. FZKA 6093. Technical report, 1998.

L. Bühler. Continuum models for pebble beds in fusion blankets. FZKA 6561. Technical report, 2002.

L. Bühler and J. Reimann. Thermal creep of granular breeder materials in fusion blankets. *Journal of Nuclear Materials*, 307:807–810, 2002.

C. K. Chan and C. L. Tien. Conductance of packed spheres in vacuum. *Journal of Heat Transfer*, 95 Ser C(3):302–308, 1973.

J. Christoffersen, M. M. Mehrabadi, and S. Nemat-Nasser. A Micromechanical description of granular material behavior. *Journal of Applied Mechanics(Transactions of the ASME)*, 48(2): 339–344, 1981.

I. F. Collins and G. T. Houlsby. Application of thermomechanical principles to the modelling of geotechnical materials. *Proceedings of the Royal Society of London Series a-Mathematical Physical and Engineering Sciences*, 453(1964):1975–2001, 1997.

Olivier Coube. *Modelling and numerical simulation of powder die compaction with consideration of cracking.* Phd thesis, Frauhofer-Institut für Werkstoffmechanik, 1998.

D.J. Cumberland and R.J. Crawford. *The Packing of Particles*, volume 6 of *Handbook of Powder Technology*. Elsevier, 1987.

P. A. Cundall. Formulation of a 3-dimensional distinct element model .1. a scheme to detect and represent contacts in a system composed of many polyhedral blocks. *International Journal of Rock Mechanics and Mining Sciences & Geomechanics Abstracts*, 25(3):107–116, 1988.

P. A. Cundall and O. D. L. Strack. A discrete numerical model for granular assemblies. *Geotechnique*, 29(1):47–65, 1979.

M. Dalle Donne and G. Sordon. Heat-Transfer in Pebble Beds for Fusion Blankets. *Fusion Technology*, 17(4):597–635, 1990.

M. Dalle Donne, A. Goraieb, G. Piazza, and F. Scaffidi-Argentina. Experimental investigations on the thermal and mechanical behaviour of single size beryllium pebble beds. *Fusion Technology*, 38(3):290–298, 2000.

G. Dell'Orco, A. Ancona, A. DiMaio, M. Simoncini, and G. Vella. Thermo-mechanical testing of Li-ceramic for the helium cooled pebble bed (HCPB) breeding blanket. *Journal of Nuclear Materials*, 329-333(Part 2):1305–1308, 2004.

G. Dell'Orco, P. A. Di Maio, R. Giammusso, A. Malavasi, L. Sansone, A. Tincani, and G. Vella. Progress in the benchmark exercise for analyzing the lithiate breeder pebble bed thermo-mechanical behaviour. *Fusion Engineering and Design*, 81(1-7):169–174, 2006.

G. Dell'Orco, P. A. Di Maio, R. Giammusso, A. Tincani, and G. Vella. A constitutive model for the thermo-mechanical behaviour of fusion-relevant pebble beds and its application to the simulation of HELICA mock-up experimental results. *Fusion Engineering and Design*, 82 (15-24):2366–2374, 2007.

P. A. Di Maio, E. Oliveri, and G. Vella. Fusion pebble bed thermo-mechanical modelling final report A-C. DIN, Palermo, Italy. Technical report, 2002.

W. Dienst and H. Zimmermann. Investigation of the Mechanical-Properties of Ceramic Breeder Materials. *Journal of Nuclear Materials*, 155:476–479, 1988.

D. C. Drucker and W. Prager. Soil mechanics and plastic analysis or limit design. *Quarterly of Applied Mathematics*, 10:157–164, 1953.

J. Duran, J. Rajchenbach, and E. Clement. Arching Effect Model for Particle-Size Segregation. *Physical Review Letters*, 70(16):2431–2434, 1993.

J. Duran, T. Mazozi, E. Clement, and J. Rajchenbach. Size Segregation in a 2-Dimensional Sandpile - Convection and Arching Effects. *Physical Review E*, 50(6):5138–5141, 1994.

Jacques Duran. *Sands, Powders, and Grains*. Springer, 1999.

A.C. Eringen. Theory of micropolar elasticity. In H. Liebowitz, editor, *Fracture: An Advanced Treatise*, volume 2, pages 621–729. 1968.

U. Fischer, P. Pereslavtsev, P. Kotiluoto, and F. Wasastjerna. Nuclear performance analyses for HCPB test blanket modules in ITER. *Fusion Engineering and Design*, 82(15-24):2140–2146, 2007.

J.H. Fokkens. Thermo-mechanical finite element analysis of the HCPB in-pile test element. TW0-TTBB-004-D1, NRG Report 21477/02.50560/P. Technical report, 2003.

J.H. Fokkens. HELICA: Material Database. NRG Report 21630/05.69841/P. Technical report, 2005.

Y. Gan and M. Kamlah. Thermo-mechanical modelling of ceramic breeder and beryllium pebble beds. Report on TW2-TTBB-006b-D02, FZK Fusion 266. Technical report, 2006.

Y. Gan and M. Kamlah. Identification of material parameters of a thermo-mechanical model for pebble beds in fusion blankets. *Fusion Engineering and Design*, 82(2):189–206, 2007a.

Y. Gan, M. Kamlah, G Rizzi, and L. Boccaccini. Validation of a Thermo-mechanical Model for Ceramic Breeder and Beryllium Pebble Beds. Report on TW2-TTBB-006b-D03, FZK Fusion 297. Technical report, 2007.

Yixiang Gan and Marc Kamlah. Thermo-mechanical analyses of HELICA and HEXCALIBER mock-up experiments. Report on TW5-TTBB-001-D11, FZK Fusion 312. Technical report, 2007b.

Yixiang Gan and Marc Kamlah. Thermo-mechanical analyses of HELICA and HEXCALIBER mock-ups. *Journal of Nuclear Materials (Proceeding of ICFRM-13)*, in press, 2008.

L. Giancarli, V. Chuyanov, A. Abdou, M. Akiba, B. G. Hong, R. Lasser, C. Pan, Y. Strebkov, and The TBWG. Breeding blanket modules testing in ITER: An international program on the way to DEMO. *Fusion Engineering and Design*, 81(1-7):393–405, 2006.

F. A. Gilabert, J. N. Roux, and A. Castellanos. Computer simulation of model cohesive powders: Influence of assembling procedure and contact laws on low consolidation states. *Physical Review E*, 75(1):011303, 2007.

C. Goldenberg and I. Goldhirsch. Friction enhances elasticity in granular solids. *Nature*, 435 (7039):188–191, 2005.

Z. R. Gorbis, M. S. Tillack, F. Tehranian, and M. A. Abdou. Analysis of Wall-Packed Bed Thermal Interactions. *Fusion Engineering and Design*, 27:216–225, 1995.

W.A. Gray. *The Packing of Solid Particles*. Chapman and Hall, 1968.

A. L. Gurson. Continuum theory of ductile rupture by void nucleation and growth: Part I. Yield criteria and flow rules for porous ductile materials. *Journal of Engineering Materials and Technology*, 99:2–15, 1977.

A. A. Gusev. Representative volume element size for elastic composites: A numerical study. *Journal of the Mechanics and Physics of Solids*, 45(9):1449–1459, 1997.

A. A. Gusev. Asymptotic back strain approach for estimation of effective properties of multiphase materials. *Advanced Engineering Materials*, 9(1-2):117–120, 2007.

S. Hermsmeyer and J. Reimann. Particle flow of ceramic breeder pebble beds in bi-axial compression experiments. *Fusion Engineering and Design*, 61-2:367–373, 2002.

S. Hermsmeyer, B. Dolensky, J. Fiek, U. Fischer, C. Koehly, S. Malang, P. Pereslavtsev, J. Rey, and Z. Xu. Revision of the EU Helium cooled pebble bed blanket for DEMO. In *Proceedings of the SOFE Conference*, San Diego, 2003.

H. J. Herrmann and S. Luding. Modeling granular media on the computer. *Continuum Mechanics and Thermodynamics*, 10(4):189–231, 1998.

D. Hofer and M. Kamlah. Drucker-Prager-Cap creep modelling of pebble beds in fusion blankets. *Fusion Engineering and Design*, 73(2-4):105–117, 2005.

C. T. Hsu, P. Cheng, and K. W. Wong. Modified Zehner-Schlunder Models for Stagnant Thermal-Conductivity of Porous-Media. *International Journal of Heat and Mass Transfer*, 37(17):2751–2759, 1994.

H. M. Jaeger, S. R. Nagel, and R. P. Behringer. Granular solids, liquids, and gases. *Reviews of Modern Physics*, 68(4):1259–1273, 1996.

W.S. Jodrey and E.M. Tory. Computer simulation of close random packing of equal spheres. *Physical Review A*, 32(4):2347–2351, 1985.

K.L. Johnson. *Contact Mechanics*. Cambridge University Press, Cambridge, 1985.

H. Kawamura, H. Takahashi, N. Yoshida, V. Shestakov, Y. Ito, M. Uchida, H. Yamada, M. Nakamichi, and E. Ishitsuka. Application of beryllium, intermetallic compounds to neutron multiplier of fusion blanket. *Fusion Engineering and Design*, 61-2:391–397, 2002.

M. A. Keavey. A canonical form return mapping algorithm for rate independent plasticity. *International Journal for Numerical Methods in Engineering*, 53(6):1491–1510, 2002.

A.S. Khan and S Huang. *Continuum Theory of Plasticity*. John Wiley and Sons, INC., 1995.

S. Kikuchi. Numerical analysis model for thermal conductivities of packed beds with high solid-to-gas conductivity ratio. *International Journal of Heat and Mass Transfer*, 44(6):1213–1221, 2001.

R. Knitter. personal communication, unpublished results, 2008.

R. Knitter and B. Alm. Crystallisation of amorphous lithium orthosilicate and quality control of conditioned pebble beds. Fusion Nr. 254, final report on TW5-TTBB-006-D3, Forschungszentrum Karlsruhe. Technical report, 2005.

Regina Knitter, Birgit Alm, and Georg Roth. Crystallisation and microstructure of lithium orthosilicate pebbles. *Journal of Nuclear Materials*, 367-370(Part 2):1387–1392, 2007.

H. Kruggel-Emden, E. Simsek, S. Rickelt, S. Wirtz, and V. Scherer. Review and extension of normal force models for the Discrete Element Method. *Powder Technology*, 171(3):157–173, 2007.

L. Laloui and C. Cekerevac. Thermo-plasticity of clays: An isotropic yield mechanism. *Computers and Geotechnics*, 30(8):649–660, 2003.

P.M. Lang. Calculating heat transfer across small gas-filled gaps. *Nucleonics*, 20(1):62–63, 1962.

B. Loebbecke and R. Knitter. Procurement and quality control of Li4SiO4 pebbles for testing of breeder unit mock-ups. Fusion Nr. 311, final report on TW6-TTBB-006-D2, Forschungszentrum Karlsruhe. Technical report, 2007.

Z. Lu, A. Y. Ying, and M. A. Abdou. Numerical and experimental prediction of the thermo-mechanical performance of pebble beds for solid breeder blanket. *Fusion Engineering and Design*, 49:605–611, 2000.

C.V. Madhusudana. *Thermal Contact Conductance*. Springer, 1995.

H.A. Makse, David L. Johnson, and Lawrence M. Schwartz. Packing of Compressible Granular Materials. *Physical Review Letters*, 84(18):4160, 2000.

G. Marketos and M. D. Bolton. Quantifying the extent of crushing in granular materials: A probability-based predictive method. *Journal of the Mechanics and Physics of Solids*, 55(10): 2142–2156, 2007.

C. L. Martin. Elasticity, fracture and yielding of cold compacted metal powders. *Journal of the Mechanics and Physics of Solids*, 52(8):1691–1717, 2004.

C. L. Martin, D. Bouvard, and S. Shima. Study of particle rearrangement during powder compaction by the Discrete Element Method. *Journal of the Mechanics and Physics of Solids*, 51(4):667–693, 2003.

G. Mazzone, F. Lucca, and G. Samuelli. Model development for the structural analyses to take into account pebble beds during EM loading. ENEA FUS TN-BB-R-018. Technical report, 2006.

G. R. McGee, M. H. Schankula, and M. M. Yovanovich. Thermal resistance of cylinder-flat contacts: Theoretical analysis and experimental verification of a line-contact model. *Nuclear Engineering and Design*, 86(3):369–381, 1985.

S. D. Mesarovic and K. L. Johnson. Adhesive contact of elastic-plastic spheres. *Journal of the Mechanics and Physics of Solids*, 48(10):2009–2033, 2000.

S. Nemat-Nasser. A micromechanically-based constitutive model for frictional deformation of granular materials. *Journal of the Mechanics and Physics of Solids*, 48(6-7):1541–1563, 2000.

M. Oda and K. Iwashita. Study on couple stress and shear band development in granular media based on numerical simulation analyses. *International Journal of Engineering Science*, 38(15): 1713–1740, 2000.

M. Ortiz and J. B. Martin. Symmetry-preserving return mapping algorithms and incrementally extremal paths - a unification of concepts. *International Journal for Numerical Methods in Engineering*, 28(8):1839–1853, 1989.

M. Ortiz and E.P. Popov. Accuracy and stability of integration algorithms for elastoplastic constitutive relations. *International Journal for Numerical Methods in Engineering*, 21:1561–1576, 1985.

M. Ortiz and J. C. Simo. An Analysis of a New Class of Integration Algorithms for Elastoplastic Constitutive Relations. *International Journal for Numerical Methods in Engineering*, 23(3): 353–366, 1986.

G. P. Peterson and L. S. Fletcher. Thermal Contact Conductance of Packed-Beds in Contact with a Flat Surface. *Journal of Heat Transfer-Transactions of the ASME*, 110(1):38–41, 1988.

G. Piazza, M. Enoeda, and A. Ying. Measurements of effective thermal conductivity of ceramic breeder pebble beds. *Fusion Engineering and Design*, 58-9:661–666, 2001a.

G. Piazza, J. Reimann, E. Gunther, R. Knitter, N. Roux, and J. D. Lulewicz. Behaviour of ceramic breeder materials in long time annealing experiments. *Fusion Engineering and Design*, 58-59:653–659, 2001b.

G. Piazza, J. Reimann, E. Gunther, R. Knitter, N. Roux, and J. D. Lulewicz. Characterisation of ceramic breeder materials for the helium cooled pebble bed blanket. *Journal of Nuclear Materials*, 307:811–816, 2002.

G. Piazza, J. Reimann, G. Hofmann, S. Malang, A. A. Goraieb, and H. Harsch. Heat transfer in compressed beryllium pebble beds. *Fusion Engineering and Design*, 69(1-4):227–231, 2003.

G. Piazza, A. Erbe, R. Rolli, and O. Romer. Post-irradiation examinations of Li4SiO4 pebbles irradiated in the EXOTIC-8 experiment. *Journal of Nuclear Materials*, 329-33:1260–1265, 2004.

Y. Poitevin, L. V. Boccaccini, A. Cardella, L. Giancarli, R. Meyder, E. Diegele, R. Laesser, and G. Benamati. The European breeding blankets development and the test strategy in ITER. *Fusion Engineering and Design*, 75-9:741–749, 2005.

A. T. Procopio and A. Zavaliangos. Simulation of multi-axial compaction of granular media from loose to high relative densities. *Journal of the Mechanics and Physics of Solids*, 53(7): 1523–1551, 2005.

P. Redanz and N. A. Fleck. The compaction of a random distribution of metal cylinders by the discrete element method. *Acta Materialia*, 49(20):4325–4335, 2001.

J. Reimann and M. Behnke. Experimental investigation of basic properties of monosized and binary Beryllium pebble beds. FZKA 6337. Technical report, 1999.

J. Reimann and H. Harsch. Thermal creep of Beryllium pebble beds. In *Proceeding 23rd SOFT*, 2004.

J. Reimann and S. Hermsmeyer. Thermal conductivity of compressed ceramic breeder pebble beds. *Fusion Engineering and Design*, 61-2:345–351, 2002.

J. Reimann and S. Mueller. First experiments on the thermomechanical behaviour of Li4SiO4 pebble beds. In *Proceeding 20th SOFT*, pages 1337–1340, 1998.

J. Reimann and G. Worner. Thermal creep of Li4SiO4 pebble beds. *Fusion Engineering and Design*, 58-9:647–651, 2001.

J. Reimann, E. Arbogast, M. Behnke, S. Muller, and K. Thomauske. Thermomechanical behaviour of ceramic breeder and beryllium pebble beds. *Fusion Engineering and Design*, 49: 643–649, 2000a.

J. Reimann, S. Hermsmeyer, G. Piazza, and G. Woerner. Thermal conductivity measurements of deformed Beryllium pebble beds by hot wire method. In *CBBI-9*, Toki, Japan, 2000b.

J. Reimann, L. Boccaccini, M. Enoeda, and A. Y. Ying. Thermomechanics of solid breeder and Be pebble bed materials. *Fusion Engineering and Design*, 61-2:319–331, 2002.

J. Reimann, R. Knitter, and G. Piazza. New compilation of the material data base and the material assessment report. Final report on TW5-TTBB-006-D02. Technical report, 2005a.

J. Reimann, G. Piazza, Z. Xu, A. Goraieb, and H. Harsch. Measurements of the thermal conductivity of compressed beryllium pebble beds. FZKA 7096. Technical report, 2005b.

J. Reimann, R. Knitter, A. Moeslang, B. Alm, P. Kurinskiy, R. Rolli, C. Adelhelm, H. Harsch, and G. Raeke. Production and characterization of breeder and multiplier materials in support of the HELICA and HEXCALIBER experiments. Final Report on TW5-TTBB-006 D1+D2. Technical report, 2006a.

J. Reimann, G. Piazza, and H. Harsch. Thermal conductivity of compressed beryllium pebble beds. *Fusion Engineering and Design*, 81(1-7):449–454, 2006b.

J. Reimann, R. A. Pieritz, and R. Rolli. Topology of compressed pebble beds. *Fusion Engineering and Design*, 81(1-7):653–658, 2006c.

J. Reimann, R. A. Pieritz, C. Ferrero, M. Di Michiel, and R. Rolli. X-ray tomography investigations on pebble bed structures. In *8th International Symposium on Fusion Nuclear Technology*, Heidelberg, Germany, 2007.

P. Richard, M. Nicodemi, R. Delannay, P. Ribiere, and D. Bideau. Slow relaxation and compaction of granular systems. *Nature Materials*, 4(2):121–128, 2005.

K. H. Roscoe and J. B. Burland. On the generalized stress-strain behaviour of wet clay. *Engineering Plasticity*, 3:539–609, 1968.

F. Scaffidi-Argentina, G. R. Longhurst, V. Shestakov, and H. Kawamura. The status of beryllium technology for fusion. *Journal of Nuclear Materials*, 283-287(Part 1):43–51, 2000.

E.U. Schlünder. Particle heat transfer. In *Proceeding of the 7th International Heat Transfer Conference*, volume 1, pages 195–212, München, Germany, 1982. Hemishere Publ. Co.

J. C. Simo and Thomas J.R. Hughes. *Computational Inelasticity*. Interdisciplinary Applied Mathematics. Springer, 1997.

S. Song and M. M. Yovanovich. Correlation of thermal accommodation coefficient for'engineering'surfaces. In *Proceedings of the Twenty-fourth National Heat Transfer Conference and Exhibition, Pittsburgh, PA, Aug. 9-12, 1987 (A88-18501 05-34). New York, American Society of Mechanical Engineers, p. 107-116.* 1987.

Weston M. Stacey. *Fusion: an introduction to the physics and technology of magnetic confinement fusion.* John Wiley and Sons, 1984.

B. Storakers, N. A. Fleck, and R. M. McMeeking. The visco-plastic compaction of composite powders. *Journal of the Mechanics and Physics of Solids*, 47(4):785–815, 1999.

W. C. Swope, H. C. Andersen, P. H. Berens, and K. R. Wilson. A computer simulation method for the calculation of equilibrium constants for the formation of physical clusters of molecules: Application to small water clusters. *The Journal of Chemical Physics*, 76:637, 1982.

F. Tehranian and M. A. Abdou. Experimental study of the effect of external-pressure on particle bed effective thermal properties. *Fusion Technology*, 27(3):298–313, 1995.

F. Tehranian, M. A. Abdou, and M. S. Tillack. Effect of external pressure on particle bed effective thermal conductivity. *Journal of Nuclear Materials*, 215:885–890, 1994.

C. Thornton and S. J. Antony. Quasi-static deformation of particulate media. *Philosophical Transactions of the Royal Society of London Series a-Mathematical Physical and Engineering Sciences*, 356(1747):2763–2782, 1998.

A. Tincani, G. Dell'orco, P. A. Di Maio, R. Giammusso, A. Malavasi, I. Ricapito, L. Sansone, and G. vella. Preparation of HEXCALIBER tests and preliminary thermo-mechanical analysis. In *CBBI-14*, Petten, the Netherlands, 2006.

S. Torquato, T. M. Truskett, and P. G. Debenedetti. Is random close packing of spheres well defined? *Physical Review Letters*, 84(10):2064–2067, 2000.

K. Tsuchiya, H. Kawamura, T. Takayama, and S. Kato. Control of particle size and density of Li2TiO3 pebbles fabricated by indirect wet processes. *Journal of Nuclear Materials*, 345(2-3): 239–244, 2005.

K. Tsuchiya, H. Kawamura, and S. Tanaka. Evaluation of contact strength of Li2TiO3 pebbles with different diameters. *Fusion Engineering and Design*, 81(8-14):1065–1069, 2006.

J. G. van der Laan, R. Conrad, K. Bakker, L. V. Boccaccini, J. G. Boshoven, L. Buhler, J. H. Fokkens, M. A. C. van Kranenburg, B. J. Pijlgroms, and J. Reimann. Design analyses and pre-tests for the irradiation of HCPB pebble-bed assemblies. *Fusion Engineering and Design*, 51-52:909–918, 2000a.

J. G. van der Laan, H. Kawamura, N. Roux, and D. Yamaki. Ceramic breeder research and development: progress and focus. *Journal of Nuclear Materials*, 283-287(Part 1):99–109, 2000b.

J. G. van der Laan, L. V. Boccaccini, R. Conrad, J. H. Fokkens, M. Jong, A. J. Magielsen, B. J. Pijlgroms, J. Reimann, M. P. Stijkel, and S. Malang. Test-element assembly and loading parameters for the in-pile test of HCPB ceramic pebble beds. *Fusion Engineering and Design*, 61-62:383–390, 2002.

I. Vardoulakis and J. Sulem. *Bifurcation Analysis in Geomechanics*. Blackie Academic and Professional, 1995.

G. Vella, P. A. Di Maio, E. Oliveri, M. Dalle Donne, G. Piazza, and F. Scaffidi-Argentina. Modelling of the thermal-mechanical behaviour of a single size beryllium pebble bed. *Fusion Engineering and Design*, 58-9:635–640, 2001.

L. Verlet. Computer" Experiments" on Classical Fluids. I. Thermodynamical Properties of Lennard-Jones Molecules. *Phys. Rev*, 159(1):98–103, 1967.

John Wesson. *Tokamaks*, volume 118 of *International Series of Monographs on Physics*. Oxford Science Publications, third edition edition, 2004.

A. Wouterse and A. P. Philipse. Geometrical cluster ensemble analysis of random sphere packings. *Journal of Chemical Physics*, 125(19):–, 2006.

S. Yagi and D. Kunii. Studies on heat transfer near wall surface in packed beds. *AIChE Journal*, 6(1):97–104, 1960.

A. Ying, H. L. Huang, and M. Abdou. Numerical simulation of ceramic breeder pebble bed thermal creep behavior. *Journal of Nuclear Materials*, 307:827–831, 2002.

A. Ying, M. Akiba, L. V. Boccaccini, S. Casadio, G. Dell'Orco, M. Enoeda, K. Hayashi, J. B. Hegeman, R. Knitter, J. van der Laan, J. D. Lulewicz, and Z. Y. Wen. Status and perspective of the R&D on ceramic breeder materials for testing in ITER. *Journal of Nuclear Materials*, 367-370(Part 2):1281–1286, 2007.

J. G. Ziegler and N. B. Nichols. Optimum settings for automatic controllers. *Journal of Dynamic Systems, Measurement, and Control*, 115(2 B):220–222, 1993.

H. Zimmermann. Mechanische Eigenschaften von Lithiumsilikaten für Fusionsreaktor-Brutblankets. KfK 4528, Kernforschungszentrum Karlsruhe. Technical report, 1989.

A. Z. Zinchenko. Algorithm for Random Close Packing of Spheres with Periodic Boundary-Conditions. *Journal of Computational Physics*, 114(2):298–307, 1994.

Appendix A

For thermo-mechanical analysis, additional material properties for lithium orthosilicate and beryllium pebble beds are listed in this appendix, including coefficients of thermal expansion, specific heat and density. The data sources are:

- J.H. Fokkens. Thermo-mechanical finite element analysis of the HCPB in-pile test element. TW0-TTBB-004-D1, NRG Report 21477/02.50560/P. Technical report, 2003.

- J.H. Fokkens. HELICA: Material Database. NRG Report 21630/05.69841/P. Technical report, 2005.

(1) Coefficients of Thermal Expansion $(1/{}^oC)$

Temp. $({}^oC)$	Li_4SiO_4	Beryllium
0.0	1.881E-05	1.134E-05
50.0	1.965E-05	1.182E-05
100.0	2.048E-05	1.229E-05
150.0	2.131E-05	1.275E-05
200.0	2.214E-05	1.319E-05
250.0	2.298E-05	1.361E-05
300.0	2.381E-05	1.402E-05
350.0	2.464E-05	1.442E-05
400.0	2.548E-05	1.480E-05
450.0	2.631E-05	1.516E-05
500.0	2.714E-05	1.551E-05
550.0	2.798E-05	1.585E-05
600.0	2.881E-05	1.617E-05
650.0	2.964E-05	1.648E-05
700.0	3.048E-05	1.667E-05
750.0	3.131E-05	1.704E-05
800.0	3.214E-05	1.731E-05
850.0	3.298E-05	1.755E-05
900.0	3.381E-05	1.778E-05
950.0	3.464E-05	1.800E-05
1000.0	3.548E-05	1.820E-05

(2) Specific Heat (J/kg^oC)

Temp. (^oC)	Li$_4$SiO$_4$	Beryllium
0.0	1392.4	1741.80
50.0	1450.0	1900.97
100.0	1513.4	2045.53
150.0	1580.0	2176.44
200.0	1648.5	2294.66
250.0	1718.2	2401.14
300.0	1788.8	2496.83
350.0	1859.9	2582.71
400.0	1931.4	2659.71
450.0	2003.3	2728.79
500.0	2075.3	2790.93
550.0	2147.5	2847.05
600.0	2219.8	2898.14
650.0	2292.3	2945.13
700.0	2364.8	2988.99
750.0	2437.4	3030.68
800.0	2510.1	3071.14
850.0	2582.8	3111.34
900.0	2655.5	3152.22
950.0	2728.3	3194.76
1000.0	2801.1	3239.90

(3) Density (kg/m^3)

Temp. (^oC)	Li$_4$SiO$_4$	Beryllium
0.0	1526.40	1166.72